Superconducting Nanostructures for Quantum Detection of Electromagnetic Radiation

by

Amir Jafari Salim

A thesis
presented to the University of Waterloo
in fulfillment of the
thesis requirement for the degree of
Doctor of Philosophy
in
Electrical and Computer Engineering

Waterloo, Ontario, Canada, 2014

Abstract

In this thesis, superconducting nanostructures for quantum detection of electromagnetic radiation are studied. In this regard, electrodynamics of topological excitations in 1D superconducting nanowires and 2D superconducting nanostrips is investigated. Topological excitations in superconducting nanowires and nanostrips lead to crucial deviation from the bulk properties. In 1D superconductors, topological excitations are phase slippages of the order parameter in which the magnitude of the order parameter locally drops to zero and the phase jumps by integer multiple of 2π. We investigate the effect of high-frequency field on 1D superconducting nanowires and derive the complex conductivity. Our study reveals that the rate of the quantum phase slips (QPSs) is exponentially enhanced under high-frequency irradiation. Based on this finding, we propose an energy-resolving terahertz radiation detector using superconducting nanowires. In superconducting nanostrips, topological fluctuations are the magnetic vortices. The motion of magnetic vortices result in dissipative processes that limit the efficiency of devices using superconducting nanostrips. It will be shown that in a multi-layer structure, the potential barrier for vortices to penetrate inside the structure is elevated. This results in significant reduction in dissipative process. In superconducting nanowire single photon detectors (SNSPDs), vortex motion results in dark counts and reduction of the critical current which results in low efficiency in these detectors. Based on this finding, we show that a multi-layer SNSPD is capable of approaching characteristics of an ideal single photon detector in terms of the dark count and quantum efficiency. It is shown that in a multi-layer SNSPD the photon coupling efficiency is dramatically enhanced due to the increase in the optical path of the incident photon.

Acknowledgements

It is a great pleasure to thank those who made this thesis possible. First and foremost, I would like to express my gratitude to my supervisor, A. Hamed Majedi, for his support, encouragement and guidance.

I would like to thank my advisory committee members Adrian Lupascu, Andrew Heunis, Gaoxing Miao, Irene Goldthorpe and my external PhD examiner, Michael Hilke, for their valuable suggestions and feedbacks.

I am thankful to many great researchers for fruitful discussions that I have had during my PhD studies. This lengthy list includes, but is certainly not limited to: Adrian Lupascu, Anthony Leggett, Frank Wilhelm, Mohsen Keshavarz, Chris Wilson, Mehrbod Mohajer, Thomas McConkey, Hamid Mohebi, Mohsen Raeiszadeh, Iman Marvian, Sadegh Raeisi, Matteo Mariantoni, Hamid Molavaian, Zhizhong Yan, Razieh Anabestani and Jean-Luc Orgiazzi. In particular, I acknowledge a lot of long and stimulating conversations with my collaborators and friends Amin Eftekharian, Milad Khoshnegar, Mohammad Ansari and Haig Atikian.

I have greatly benefited from the CryptoWorks21 training program; I appreciate the effort by Michele Mosca at Institute for Quantum Computing (IQC) for making the CryptoWorks21 program so beneficial.

I would like to thank Jaume Gomis for supervising me when I was studying physics at the Perimeter Institute (PI). I am appreciative to my great colleagues at PI for their friendship and companionship: Isabeau Prémont-Schwarz, Chanda Prescod-Weinstein, Yidun Wan and Camille Boucher-Veronneau.

I am grateful to IQC and all its members for making a scientific and friendly atmosphere. I would like to thank Monica Dey, Roberto Romero, Sarah Landy, Annette Dietrich, Matt Cooper, Ryan Goggin for their constant help with technical and administrative issues at IQC and the department of electrical and computer engineering (ECE).

I am very lucky to have many wonderful friends in Waterloo who have all enriched my life in so many ways and I am deeply indebted to them. My heartfelt thanks to Behnaz for her unwavering encouragement and support. Last but not least, I would like to thank my parents, siblings and their families for all their love and support throughout my life.

To my parents.

Table of Contents

List of Tables **ix**

List of Figures **x**

1 Introduction **1**

1.1 Superconductivity in a Nutshell . . . 3
1.2 Josephson Junction . . . 5
1.2.1 Superconducting Nanowire Single Photon Detector . . . 6
1.3 Phase Slips in Superconducting Nanowires . . . 8
1.3.1 Thermally Activated Phase Slips (TAPS) . . . 10
1.3.2 Phenomenological Theory of QPS . . . 15
1.3.3 Microscopic Theory of QPS . . . 16
1.4 Applications of QPS Junction . . . 20
1.4.1 Quantum Phase Slip Qubits . . . 20
1.4.2 Quantum Standard for Electrical Current Based on QPS . . . 22
1.5 Objectives of This Thesis . . . 23
1.6 Outline of This Thesis . . . 26

I 1D Superconducting Nanowires **27**

2 Complex Conductivity of Superconducting Nanowires **28**

2.1 Introduction . . . 28

2.2 Complex Conductivity 29
2.3 Disscussion 32
2.4 Concluding Remarks 34

3 Stimulation of Quantum Tunnelling by a High-frequency Field in Zero-current State of a 1D Superconducting Nanowire 37

3.1 Introduction 37
3.2 Modelling of a QPS Junction in a High-frequency Field 40
3.3 Weak Dissipation 42
  3.3.1 QPS Junction with Dissipation 45
3.4 Discussion 47
3.5 Concluding Remarks 51

4 Proposal for QPS-based Energy-resolving High-frequency Radiation Detector 52

  4.0.1 Superconducting THz Detection Methods 53
4.1 The Physical Principle of the QPS-based THz Detector 54
  4.1.1 Design Parameters 54
4.2 Discussions 62
4.3 Concluding Remarks 63

II 2D Superconducting Nanostrips 64

5 Multi-layer SNSPD 65

5.1 Introduction 65
5.2 Pancake Vortices in a Superconducting Multi-layer System 68
5.3 Potential Barrier for Vortex Crossing 70
5.4 Electrical isolation of superconducting layers 76
5.5 Photon absorption 77
5.6 Concluding Remarks 78

6 Conclusions and Outlook 80

6.1 Contributions 80
6.2 Other Contributions Not Presented in Thesis 81
6.3 Outlook 82

APPENDICES 83

A The Effective Action of Superconducting Nanowires 84

A.1 The Model 84
A.2 Effective Action for 1D Nanowire 87

B Kernels 89

C Quantum Tunneling in a High-frequency Field 91

C.1 Semmiclassical Physics and Quantum Tunneling 91
  C.1.1 Tunneling in a time-dependent potential barrier 95

D Duality Between QPS and Josephson Junction 97

E Vortex Structure in 2D Films 102

F Transfer-matrix Method for Multi-layer Thin Films 105

References 109

List of Tables

4.1 Material properties of the superconducting nanowires used for simulations. 56

D.1 Table of duality transformations between QPS and Josepshon junction . . 101

List of Figures

1.1 The schematic diagram of a voltage-biased Josephson junction 6

1.2 Three different types of superconducting Josephson qubits shown, (a) charge qubit, (b) flux qubit and (c) phase qubit. 7

1.3 (a) The schematic of a SNSPD system with the biasing and the detection circuitry. (b) A small section of the superconducting nanowire hit by a single photon is depicted. (c) A photon detection event on the osciloscope. 9

1.4 A phase slip event is shown. The order parameter of a superconducting nanowire is plotted along the real and imaginary axis. 11

1.5 The free energy barrier between two minima is shown. 13

1.6 (a) The schematic of a proposed QPS qubit. (b) Energy levels of the system in terms of the applied magnetic flux is shown. 21

1.7 (a) The metrological triangle of electrical units. (b) The current-Voltage characteristic of a QPS junction under microwave irradiation of frequency f. 23

2.1 Plot of the local complex conductivity of superconducting nanowires in the limit of $T = 0$ and $\hbar Dk^2 \ll \hbar\omega, \Delta_0$. Conductivity is normalized by the Drude conductivity of the normal metal. σ_1 is zero for frequencies bellow 2Δ, and approaches σ_{1n} of normal metal for high frequencies. σ_2 is divergent at $\omega = 0$. 35

3.1 Quantum tunnelling of a particle from the metastable potential barrier under the influence of a high frequency field is shown. 39

3.2 The schematic circuit of a QPS junction including an ideal QPS element (a superconducting nanowire), the dissipative element R, the bias voltage V_{dc} and the driving source V_{ac}. 40

3.3 The tilted washboard potential $V(Q)$ and the classical turning points are shown. The motion between Q_1 and Q_2 is classically allowed; whereas, the motion between Q_2 and Q_3 happens through quantum tunnelling. 44

3.4 Numerical values of τ_S, t_0 and t_1 at four different temperatures. Here, $T^* = \omega_p\hbar/2\pi k_B$. The dotted red lines correspond to boundaries of the crossover from quantum tunnelling to thermal activation. Graphs are adopted from [1]. 46

3.5 Enhancement of the probability of quantum tunnelling as a function of the normalized frequency Ω/ω_p. Parameters used for the simulation are $V_{ac}/V_c = 0.1$, $\eta/\omega_p = 10$ and $4eV_c/\omega_p = 10$. 48

3.6 Quantum tunnelling of a particle from the metastable potential barrier for two cases of dissipative and non-dissipative tunnelling is shown. 50

4.1 The schematic of a QPS high-frequency detector is shown. The red segment in the middle, is the superconducting nanowire. A broadband bow-tie antenna collects the high-frequency field. 55

4.2 The QPS energy as a function of the normal resistance per length for four different materials NbSi, InO$_x$, NbN and Ti is shown. The R_n determines the dimensions of the superconducting nano wire. Parameters are listed in Table 4.1. 57

4.3 The inductive kinetic energy as a function of the normal resistance per length for four different materials NbSi, InO$_x$, NbN and Ti is shown. The R_n determines the dimensions of the superconducting nano wire. Parameters are listed in Table 4.1. 59

4.4 The plasma frequency $\omega_p/2\pi$ as a function of the normal resistance per length for four different materials NbSi, InO$_x$, NbN and Ti is shown. The R_n determines the dimensions of the superconducting nano wire. Parameters are listed in Table 4.1. 60

4.5 The ratio of E_{QPS}/E_L as a function of the normal resistance per length for four different materials is shown. For the charge number to be the good quantum number, it is required that $E_{QPS} > 4E_L$. The unwanted region of parameters is highlighted with red. 61

5.1 The schematic cross section of a N=3 SNSPD is shown. Each superconducting layer is separated by an insulating layer such that the Josephson current between the layers is negligible. All superconducting layers are independently biased. 66

5.2 A typical count rate versus the bias current in a SNSPD. 67

5.3 A schematic full vortex in an N=3 layer system made of 3 pancake vortices is shown. The magnetic field produced by pancake vortices varies on scale of $\lambda_\parallel$ (not shown). The figure is not drawn to scale ($\Lambda_D \gg D$). 69

5.4 Two pancake vortices residing at two different layers are shown. z_j is the verical distance and r is the horizontal distance between the two vortices. Two vortices attract each other. 71

5.5 Image vortices for a superconduting nanostrip are shown. The superconducting strip is indicated by two parallel dotted line. The two edges of the superconducting strip is replaced by an inifite series of vortices of alternating charges according to Eq. (5.4). 72

5.6 The potential barrier for vortex crossing according to Eq. (5.10) for different number of layers. 74

5.7 The potential barrier for vortex crossing according to Eq. (5.10) for different bias currents. 75

5.8 The normalized vortex crossing rate vs. normalized bias current for a N-layered SNSPD calculated using Eq.(5.14). 76

5.9 The schematic cross section of a N=3 SNSPD with a reflector is shown. A properly designed reflector under the substrate helps in improving the absorption rate by reflecting the transmitted power back into the layers for the second chance of absorption [2]. 77

5.10 The simulation of the ratio of the power absorption (A) to the total power entering a multi-layer SNSPD ($A + T$) for different number of layers at 1550nm is shown. 79

C.1 Potential barrier for a particle moving from left to right with energy E. Classical turning points are indicated by x_1 and x_2. According to Eq. (C.5), for $x_1 < x < x_2$, the time becomes complex. 93

C.2 The integration contour for the quantum tunnelling probability. The vertical sections correspond to the underbarrier motion. 93

D.1 The ratio of E_{QPS}/E_L as a function of the normal resistance per length for four different materials is shown. For the charge number to be the good quantum number, it is required that $E_{QPS} > 4E_L$. The unwanted region of parameters is highlighted with red. 98

D.2 Dual circuits of a Josephson junction and a QPS junction. The Josephson (QPS) junction is current (voltage) biased. Dynamics of the the two circuits are equivalent for dual parameters. 100

D.3 Current-voltage characteristics of a Josephson junction (left) and a QPS junction(right). For $I < I_c$, the Josephson junction is in the zero-voltage stated. For $V < V_c$ the QPS is in the zero-current state. 100

F.1 Optical wave incident on a thin film of thickness d. 106

F.2 An assembly of thin films with different thicknesses and refractives indices. 107

Chapter 1

Introduction

Superconductivity has a special position in the race towards realization of quantum information processing. Unique properties of superconductors makes them attractive in exploring and exploiting quantum phenomena in regimes accessible to the macroscopic world. Superconductors can be found in development of qubits which directly manifesst quantum nature or in systems that indirectly helps in exhibiting quantum behaviour like superconducting nanowire single photon detectors (SNSPD).

Quantum state of a superconducting condensate which consists of macroscopic number of particles can collectively be written as a single wave function, in analogy to the wave function solution of the Schrodinger equation. This property is one of the underlying causes of all the remarkable properties of superconductors like perfect conductivity and perfect diamagnetism. Like any other quantum many-body systems, superconductors are not immune to fluctuations. Fluctuations which can be quantum or thermal in nature modify the properties of superconductors. This modification becomes more important as we reduce their dimensions or introduce stronger disorder.

In low-dimensional superconductors, i.e., 1D and 2D superconductors, fluctuations have a more significant consequences compared to bulk. In 2D superconductors, topological excitations exist in the form of magnetic vortices which can lead to phase transitions. In a vortex the magnitude of the order parameter drops to zero locally and the phase acquire finite winding around the core. Vortices interact with each other and with the current in the film. A similar scenario happens in 1D superconductors where topological excitations are in the form of phase slips. In a phase slip, the magnitude of the order parameter drops to zero at a point along the superconducting nanowire and the phase jumps by integer multiple of 2π. Phase slips can be caused by thermal or quantum fluctuations.

Phase slips can interact with each other and can influence the macroscopic behaviour of the superconducting nanowires by causing finite resistivity in the superconducting phase.

Topological fluctuations are mostly restricting and unwanted; however, they can be useful too. In 2D superconducting nanostrips, motion of vortices can cause dissipative processes and reduce of the maximum current that nanostrips can carry. This results in the reduction of the quantum efficiency and dark counts in SNSPDs. On the other hand quantum phase slips (QPS) are capable of providing properties similar to Josephson junction which can have numerous applications. For instance, QPS phenomenon can be the basis of new types of qubits, quantum standard of current and as we will show later in this thesis new types of high-frequency detectors.

Our main goal in this thesis, in general, is to understand and control topological fluctuations in 1D and 2D superconducting nanostructures for improving quantum efficiencies of superconducting photon detectors or creating novel quantum devices. In 1D, we will investigate the effect of high-frequency field on superconducting nanowires. We will show that a high-frequency field can change the rate of QPS and how this can be exploited in designing new high-frequency detectors. In 2D, we will see how vortices behave in superconducting nanostrips and based on that we show how we can reduce them from entering the nanostrips and hence improving the efficiency of SNSPDs. The objective of this thesis is presented in details after background concepts are reviewed.

A comment on the usage of words “nanowire” and “nanostrips” is in order. In the literature the word “nanowire” is often used instead of “nanostrips”, e.g., in superconducting nanowire single photon detector. In this thesis we will also use the word “nanowire” for both 1D nanowires and 2D nanstrips as far as it is clear from the context what exactly is meant.

In this thesis, except Chapter 5, the CGS system of units is used which, in the literature, is typically adopted in theoretical work. In Chapter 5, the SI system of units is adopted which is more convenient in engineering applications. Throughout this thesis, $\hbar$ is explicitly stated.

For the rest of the introduction, we first introduce key concepts in superconductivity that will be used throughout this thesis. After a brief encounter with Josephson junctions, as key elements in superconducting devices, superconducting nanowires and nanostrips are introduced. As motivations for this research, some applications of superconducting nanowires are then presented. Then, we express the objectives of this research including goals and challenges. Finally, the organization of this thesis is provided.

1.1 Superconductivity in a Nutshell

The signature property of the majority of superconductors is the presence of a gap bellow a critical temperature. The appearance of the gap, along with the macroscopic coherence, allows the current to flow without experiencing any resistance or dissipation. This lack of resistivity, or in other words infinite conductivity, exists provided that the condensed electrons (Cooper pairs) which are isolated by the gap can not be excited (broken) to overcome the gap barrier and be a part of normal electron current that leads to dissipation [3].

The superconducting state happens when electrons, with energy near the Fermi surface, form weakly bound states known as Cooper pairs. Energy-wise, formation of Cooper pairs in the superconducting state is favourable for the system as it reduces the free energy of the system. The binding energy of electrons in a Cooper pair is $E_g = 2\Delta$, where Δ is known as the energy gap. Transition to the superconducting phase can only take place bellow a critical temperature T_c that varies for different materials. Typical critical temperatures in various materials can vary from a few mili-Kelvin to the present record of about 134 Kelvin. The search for finding superconductors with higher T_c is actively pursued around the globe. The two macroscopic hallmark of the superconducting phase are

- Infinite DC conductivity
- Expulsion of an external magnetic field (Meissner Effect)

In the Meissner effect, an external magnetic field can not penetrate into a superconductor except in a very thin layer, known as the penetration depth; however a strong magnetic field can destroy the superconducting phase if it exceeds a threshold level, known as the critical magnetic field H_c[1].

There are two major formalisms in studying superconductivity, BCS (Bardeen-Cooper-Shriffer) which is a microscopic description and GL (Ginzburg-Landau) which is a macroscopic (GL) theory in nature. Both theories are compatible with each other despite having different range of validity. In the GL formalism, the state of a superconductor is characterized by a complex-valued order parameter $\psi = |\psi| \exp(\varphi)$. The magnitude of the order parameter $|\psi|$ is related to the density of the Cooper pairs by the relation $n_s = |\psi|^2$.

---

[1] This is true for superconductors of the first type; in superconductors of the second type, there is an intermediate state in which above H_{c1} a part of the magnetic flux can penetrate into the sample in the form of flux vortices; however, when external magnetic field becomes too strong, an upper critical magnetic field H_{c2} is defined above which, the superconductivity is completely destroyed.

The phase of the order parameter, denoted by φ, is the analogue of the phase of the wave function in quantum mechanics. Magnitude and the phase of the order parameter play equally important roles in the physics of superconductors. In GL theory, electrons are considered as a fluid that can exist in two, i.e., normal and superconducting phases like a general second order phase transition. In addition, GL allows variation in the density of the superconducting electrons by considering the wave function as a complex-valued function of coordinates. The free energy of the GL theory can be written as

$$F = \int d^3r \left\{ \frac{1}{4m} \left| (-i\hbar\nabla - \frac{2e}{c}\mathbf{A})\psi \right|^2 - \alpha \left|\psi\right|^2 + \frac{1}{2}\beta \left|\psi\right|^4 + \frac{\mathbf{B^2}}{8\pi} \right\}, \tag{1.1}$$

where A is the magnetic potential, α and β are phenomenological parameters that characterize the phase of the matter and $\mathbf{B} = \nabla \times \mathbf{A}$ [3]. In Eq. (1.1), m is the mass and e is the charge of an electron. Variation of the GL free energy with respect to ψ and A yields two coupled equations of motion

$$\alpha\psi + \beta|\psi|^2\psi - \frac{\hbar^2}{4m}\left(\nabla - \frac{2ie}{\hbar c}\mathbf{A}\right)\psi = 0, \tag{1.2}$$

and

$$\begin{aligned} \mathbf{J} &= \frac{ei\hbar}{2m}\left(\psi\nabla\psi^* - \psi^*\nabla\psi\right) - \frac{2e|\psi|^2}{mc}\mathbf{A} \\ &= \frac{e\hbar|\psi|^2}{m}\left(\nabla\varphi - \frac{2e}{\hbar c}\mathbf{A}\right). \end{aligned} \tag{1.3}$$

Solving Eqs. (1.2) and (1.3) corresponds to finding the stationary conditions for the superconductor. From Eqs. (1.2) and (1.3) two characteristic lengths for the variation of the order parameter known as the coherence length (ξ) and variation of the electromagnetic field known as the London's penetration depth (λ) are obtained:

$$\begin{aligned} \xi(T) &= \frac{\Phi_0}{2\sqrt{2}\pi H_c(T)\lambda(T)}, \\ \lambda(T) &= \sqrt{\frac{2mc^2}{4\pi|\psi|^2(2e)^2}}, \end{aligned} \tag{1.4}$$

where $H_c(T)$ is the critical magnetic field. Roughly speaking, the ξ is the average distance between two electrons in a Cooper pair and the λ is the distance that the magnetic field penetrate inside a superconductor. As two examples, the coherence length and the penetration depth in aluminium are around 1550nm and 45nm respectively and for niobium they are 39nm and 52nm.

1.2 Josephson Junction

In the center of many applications of the superconductors are Josephson junctions. Josephson junctions are used in many devices and applications like, SQUIDs, parametric amplifiers, standard of voltage, radiation detector and generator and more recently qubits. A Josephson junction is made of two superconductors separated by a non-superconducting or a weak-superconducting barrier through which Cooper pairs can, quantum mechanically, tunnel from one superconductor to the other [3]. Fig. 1.1 shows the schematic of a Josephson junction biased with voltage V. The state of the two superconductors are specified by two phases φ_L and φ_R. According to the Josephson relations, the current and voltage are related to the phase difference:

$$\begin{aligned} I &= I_c \sin\delta, \\ V &= \frac{\Phi_0}{2\pi}\frac{d\delta}{dt}, \end{aligned} \tag{1.5}$$

where $\Phi_0 = hc/2e$ is the superconducting flux quantum, c is the speed of light, I_c is the critical current of the junction and $\delta = \varphi_L - \varphi_R$ according to Fig. 1.1. From Eq. (1.5) and using the relation for an inductor according to $V = L_J dI/dt$, we can see that a Josephson junction is in fact a nonlinear inductor with the inductance given by

$$L_J = \frac{\Phi_0}{2\pi I \cos\delta}. \tag{1.6}$$

A Josephson junction in conjunction with a capacitor C can form a LC resonator. These tunable resonators have recently been used as the building blocks of qubits for realization of quantum information processing. In the following, we briefly look at qubits made from Josephson junctions.

Qubits with Josephson Junctions

A Josephson qubit is a nonlinear resonator made from Josephson inductance and a capacitance which in some cases is the capacitance of the junction [4]. Non-linearity in Josephson junctions, discussed above, is crucial, otherwise, we would get an equally spaced energy spectrum, like the case of simple harmonic oscillators. It is desirable that the spacing between neighbouring energy levels, e.g., 0 and 1 be different from 1 and 2 and so on. This mismatch in energy spacing allows us to excite a transition between only two desired levels, e.g., $0 \leftrightarrow 1$ and not, for example, the transition between $2 \leftrightarrow 3$.

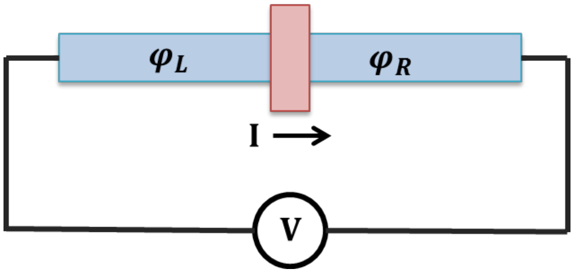

Figure 1.1: The schematic diagram of a voltage-biased Josephson junction. Two superconductors denoted by L and R are separated by a very thin insulator, normal or weekly superconducting material. The current is obtained from the relation $I = I_0 \sin \delta$, where $\delta = \varphi_L - \varphi_R$.

There are three major classes of superconducting qubits made from Josephson junctions, that are shown in Figure 1.2. In Fig. 1.2(a), a charge qubit is shown whose basis states are charge states. Charge states are excess Cooper pairs in the island formed from one electrode of the Josephson junction adjacent to one electrode of the capacitor. Superposition of different charge states is achieved by tunnelling of the Cooper pairs from the gate of the Josephson junction into the island; this process is controlled by a voltage source. The second class is the flux qubit, shown in Fig. 1.2(b). In flux qubits, the persistent current in the Josephson loop flows in two opposite directions, i.e., clockwise and counter clockwise or in a superposition of these two. These two oppositely flowing persistent currents are the basis states of a flux qubit. The state of a flux qubit is controlled by an external magnetic flux created by a separate circuit shown adjacent to the Josephson loop in Fig. 1.2(b). The third family of superconducting qubits is the phase qubit shown in Fig. 1.2(c). For a phase qubit, the effective potential of the system is shown in Fig. 1.2(d). The slope of the potential is controlled by the current source and it is chosen such that at each local minima only two energy levels, i.e., E_0 and E_1 exist. In all three classes of Josephson qubits, the lowest two levels are chosen as the two level system for a qubit.

1.2.1 Superconducting Nanowire Single Photon Detector

A superconducting nanowire single photon detector (SNSPD), is made of ultra-thin serially connected strips of nanowires, biased with a current close to the critical value. A simple scenario of a photon detection process is as follows: when the system is cooled down, an optical photon, that typically carries an energy in the range of an electron volt (eV), can

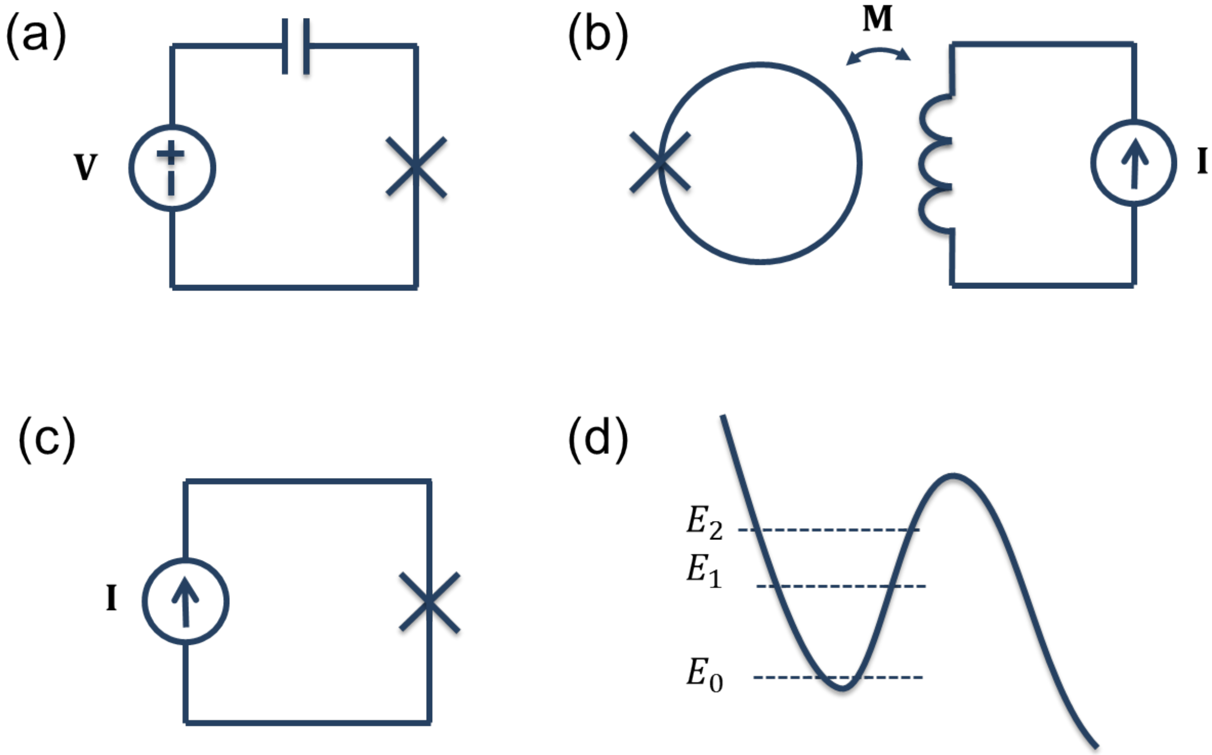

Figure 1.2: Three different types of superconducting Josephson qubits shown, (a) charge qubit, (b) flux qubit and (c) phase qubit. Josephson junctions are denoted by crosses (d) shows the effective potential for the phase qubit. The lowest three energy levels are shown for the phase qubit. Due to the nonlinearity of the Josephson junction $|E_1 - E_0| \neq |E_2 - E_1|$.

break a large number of Cooper pairs with the binding energy of the order of millielectron volt (meV). Locally, in the region that the photon hits the nanowire, the broken Cooper pairs push the superconductor into the normal phase (dissipative phase). Since the size is too small, the current can not detour the normal region without exceeding the critical current of the superconducting nanowire in side channels; therefore, the nanowire becomes normal (dissipative) in that small section and due to the dissipation a photon-induced voltage peak that indicates the presence of a photon can be observed. This simple description overlooks many details that can be found, for example in reference [5]. Fig. 1.3(a) shows the schematic of a typical SNSPD with the biasing and detection setup. The function of the bias-T is to combine and separate the dc and ac components of signals in the system. The dc component comes from the bias current and the ac component from the fast voltage signal that is produced in the event of the photon detection. The meandering of the superconducting nanowire is for increasing the active area of the device. A photon event in a SNSPD is marked by a voltage peak that surpasses a threshold, as shown in Fig 1.3(b). An amplifier which is not shown in Fig. 1.3 is usually employed to amplify the signal that comes from the photon induced voltage peak. Typical thickness for a SNSPD is about 4 to 6 nm and the width is about 80 to 120 nm. Popular materials being used are Nb, NbN, NbTiN and recently WSi. The Nb family of SNSPDs work at the liquid helium temperature; whereas, SNSPDs made of WSi require sub-kelvin temperature which is a big disadvantage. Despite that the optical absorption of WSi is significantly higher than Nb family which leads to a dramatically better quantum efficiency in SNSPDs made of WSi.

1.3 Phase Slips in Superconducting Nanowires

In this chapter we look at the physics of phase slips (PSs) in superconducting nanowires. Phase slip phenomenon plays an important role in the deviation of the behaviour of superconducting nanowires from bulk. The resistivity observed in superconducting nanowires can be explained by PSs. PS in superconducting nanowires are dual to Josephon junction and have a very interesting physics that can be used in variety of applications.

In general, PSs are due to fluctuations; however, fluctuations can have two different origins, i.e., thermal and quantum. Phase slips due to thermal fluctuation have been known since 1960s; however, phase slips due to quantum effects are known since 1990s and reliable experimental results have been available only since 2000s [13].

PSs due to thermal fluctuations are dominant in the vicinity of the critical temperature and quantum phase slips (QPSs) become important away from the critical temperature, close to zero Kelvin. A macroscopic theory that can explain PSs due to thermal fluctuations

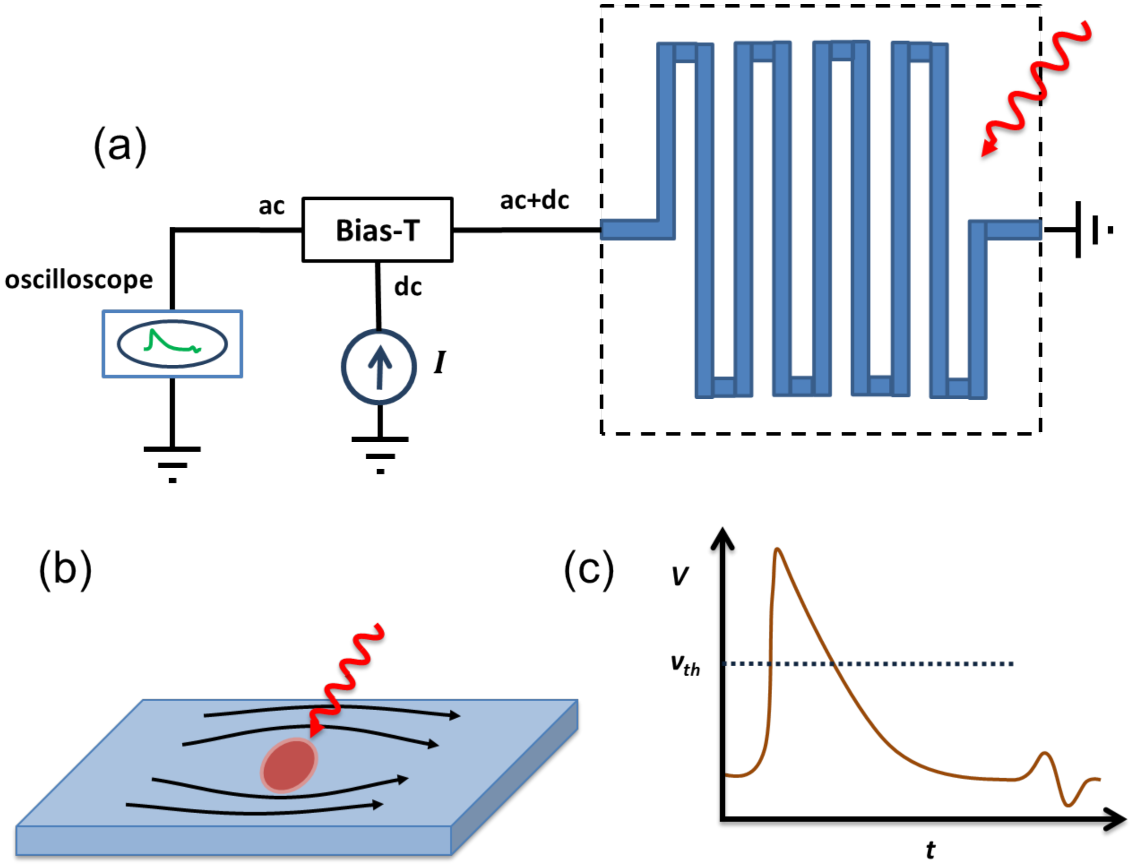

Figure 1.3: (a) The schematic of a SNSPD system with the biasing and the detection circuitry. The superconducting nanowire meanderline is dc-current-biased , in case of a photon incident a voltage peak appears on the osciloscope. (b) A small section of the superconducting nanowire hit by a single photon is shown. The nanowire is biased close to its critical current (I_c). A single photon breaks cooper pairs and create a normal-state hotspot. The transport current is pushed toward edges which is still superconducting. This causes the local current density exceds the local critical current density. A belt of normal-phase is formed across the superconducting nanowire which results in a voltage peak at the sciloscope. (c) A photon detection event on the osciloscope. An event is registered if the voltage peak surpasses the threshold voltage (v_{th}). The rise time and decay time are in the order of few pico seconds and about ten nano seconds, respectively.

was developed by Langer, Ambegaokar, McCumber and Halperin, and is known as the LAMH model [6, 7]. LAMH model will be introduced in the next section. For QPSs, there is also a macroscopic theory that qualitatively can explain the experimental results [8, 9]. The microscopic theory that can explain PSs and some other properties of the superconducting nanowires is the theory developed by Golubev and Zaikin (GZ) [10, 11, 12, 13] . The GZ model will be used later in this thesis to study the complex conductivity of superconducting nanowires .

1.3.1 Thermally Activated Phase Slips (TAPS)

Little [14], was the first to observe the decay of the persistent current on a quasi-one-dimensional superconducting wires. Based on his experimental results he proposed that Thermally Activated Phase Slips (TAPS) in superconducting nanowires can result in finite resistance bellow T_C where superconductors are supposed to exhibit perfect conductivity. He suggested that thermal fluctuations in the magnitude of the order parameter can explain this phenomenon.

This process can be explained as follows. We consider a superconducting nanowire with a constant voltage between the two ends as was, experimentally, observed by Little [14]. According to the Josephson junction relation (1.5), the phase difference between the two ends of the wire has to increase linearly with time. We also know, from the Ginzburg-Landau (GL) theory (will be introduced bellow) that the supercurrent $J \propto |\psi|^2 \nabla\varphi$; hence, the current will increase continuously until it reaches the critical limit and the nanowire becomes normal metal. To maintain a steady state supercurrent, there must be some mechanism through which the magnitude of the order parameter goes to zero somewhere along the wire. At this moment, the relative phase across this point can slip by 2π and therefore reducing the $\Delta\varphi$. This reduction in $\Delta\varphi$ prevents the growth of the supercurrent. These phase slips can give rise to a voltage and, consequently, resistivity of the superconducting nanowires bellow the critical temperature. A PS process is illustrated in figure (1.4) .

To quantitatively explain the results of Little's experiments [14], Langer and Ambegaokar (LA) [6] suggested that a current carrying state of a superconducting nanowire is metastable; whenever the system is thermally activated to pass over a free energy barrier to a state with lower energy, dissipation occurs. Each local minimum of the GL free energy corresponds to a current carrying state. The probability of transitions between each of local minima depends on the height of the free energy barrier between a saddle point relative to a local minimum. LA used the phenomenological Ginzburg-Landau (GL) theory for their model as is explained here.

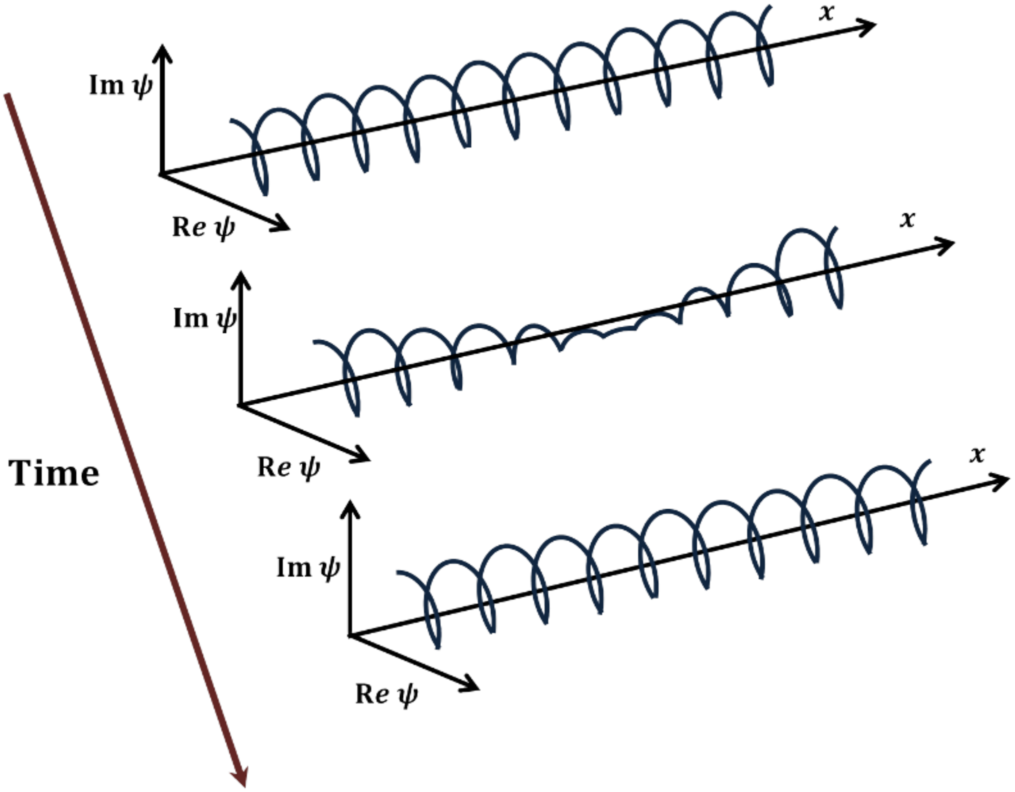

Figure 1.4: A phase slip event is shown. The order parameter of a superconducting nanowire is plotted along the real and imaginary axis; the x axis is along the length of the wire. Voltage at the two ends of the superconducting nanowire leads to increase and tightening of the loops; this consequently results in the increase of the current. In a steady state, the order parameter needs to loose loops to avoid the unlimited increase in the current. For this to happen, as shown in the middle plot, the magnitude of the order parameter goes to zero at some point along the wire and because of that the helix can unwind and cancel the tightening due to the voltage. A steady state is reached when the rate of the unwinding equates the rate of tightening due to the voltage.

The starting point for LA theory is the one dimensional form of the GL equation (1.1) in the form

$$F[\psi(x)] = \int dx \{ \left| \frac{d\psi}{dx} \right|^2 - \alpha \left|\psi\right|^2 + \frac{1}{2}\beta \left|\psi\right|^4 \}. \tag{1.7}$$

Here the vector potential has been dropped, because we are interested in samples with diameters much smaller than the penetration depth and for small current carrying states; therefore, the contribution from the vector potential is negligible [6]. Also, we have rescaled ψ, α and β such that the factor $2m$ disappears from (1.1) for the sake of simplicity. The stationary condition corresponding to local minima can be found from

$$\frac{\delta F}{\delta \psi(x)} = 0, \tag{1.8}$$

which results in the GL equation

$$-\frac{d^2\psi}{dx} - \alpha\psi + \beta\psi \left|\psi\right|^2 = 0. \tag{1.9}$$

By choosing a periodic boundary condition which ($\psi(-X/2) = \psi(X/2)$) which is a reasonable choice for loops and long wires, and assuming constant current, the solutions to Eq. (1.9) can be written as

$$\psi_k = f_k \exp(ikx), \qquad f_k = \frac{(\alpha - k^2)}{\beta}, \tag{1.10}$$

where $k = 2n\pi/X$. ψ can be pictured as a helix in the complex plane as shown in figure (1.4) . As the super-current increases, the helix becomes more tightened; a phase slip event corresponds to unwinding of one loop through fluctuations; due to a PS event the phase of the order parameter can change $\psi_k \to \psi_{k\pm 2\pi/X}$.

By finding the saddle point solution of Eq. (1.9), i.e., a solution that is uniform over the entire length of the wire except in some small part, LA found the free-energy barrier. They used the analogy of the equations to those of the motion of a particle in a central force and made use of the conservation of the energy for their calculation. Their lengthy calculations will not be repeated here. What they found was a solution that over a small region along the length of the wire, the amplitude of the order parameter could go to zero and the phase could change very rapidly; because of that the current carrying state of a superconducting nanowire can roll down the hill in the free energy and hence leads to the unwinding of the ψ. By using this solution in the GL free energy (1.7), LA calculated the barrier to be

$$\Delta F = \frac{8\sqrt{2}}{3} \frac{H_c^2}{8\pi} s\xi, \tag{1.11}$$

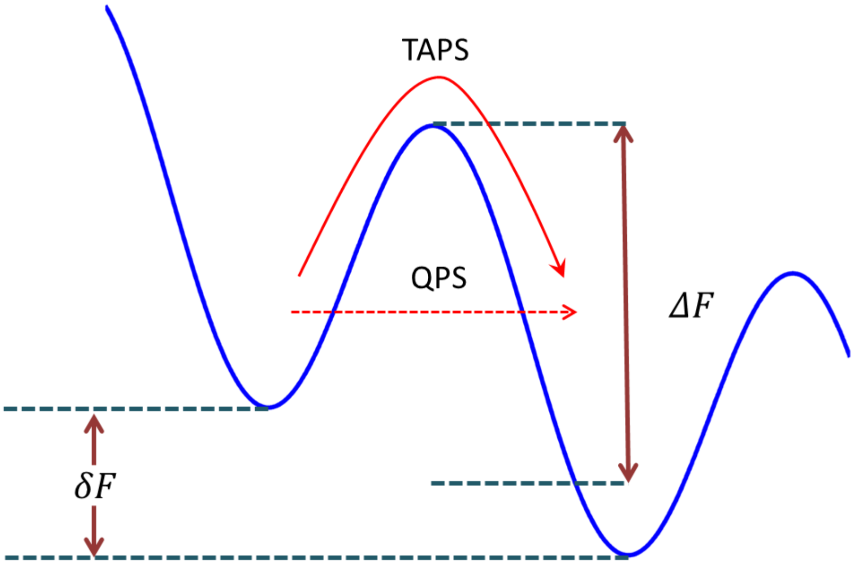

Figure 1.5: The free energy barrier between two minima is shown. The tilt (δF) in the free energy is caused by the presence of the bias current. This tilt makes transition to the lower state more favourable. In TAPS, the system climbs over the energy barrier and ends up in a lower energy. In QPS the system tunnels through the energy barrier.

where ξ is the GL coherence length, s the cross section of the nanowire, and H_c is the critical magnetic field. In Eq.(1.11), ignoring the numerical factor, ΔF can be interpreted as the condensation energy in the volume $S \times \xi$ where the superconducting nanowire goes normal. This originates from the fact that any change in ψ can not happen over any length smaller than ξ. At this point, LA added a current bias to the superconducting nanowire. Without a current, the transition to $k \to k \pm 2\pi/X$, which correspond to adding or removing a loop, can occur with the same probabilities. The presence of the current makes one of transitions more favourable by tilting the free energy diagram as shown in Fig. 1.5. The difference in the free energy barrier for jumps in two directions is related to the electrical work according to

$$\delta F = \Delta F_{+} - \Delta F_{-} = \int VIdt = I(\Delta\varphi)\frac{\hbar}{2e} = I\frac{\hbar}{2e}, \tag{1.12}$$

where the Josephson junction relation has been used.

To characterize a phase slip event, in addition to the free-energy barrier, we need to introduce an attempt frequency Ω [6]; we can write the rate of PS events to be

$$\begin{aligned}\frac{\Delta\varphi}{dt} &= \Omega\Big[\exp\left(-\frac{\Delta F - \delta F/2}{k_B T}\right) - \exp\left(-\frac{\Delta F + \delta F/2}{k_B T}\right)\Big] \\ &= 2\Omega\exp\left(-\frac{\Delta F}{k_B T}\right)\sinh\left(\frac{\delta F}{2k_B T}\right).\end{aligned} \tag{1.13}$$

Using the Josephson relation and Eq. (1.13), in the limit of a small current, the resistivity is

$$R = \frac{V}{I} = R_q \frac{\hbar}{k_B T}\Omega\exp\left(-\frac{\Delta F}{k_B T}\right), \tag{1.14}$$

where $R_q = \hbar/4e^2 = 6.5$ kilo-ohm is the quantum resistance for a Cooper pair.

The attempt frequency Ω is the last thing to calculate. LA theory was based on the time independent GL theory which lacks any time scale; therefore LA, for the attempt frequency, used $\Omega_{LA} \sim N\tau$ where N is the number of the electrons in the conductions band and τ is the relaxation time of electrons in a normal metal.

Later, McCumber and Halperin (MH) [7], improved the attempt frequency obtained by LA by using time dependent GL theory (TDGL). The TDGL equation can be written as

$$\frac{\partial\psi}{\partial t} = -\frac{4\pi}{sH_c^2\xi\tau_{GL}}\frac{\delta F}{\delta\psi^*}, \tag{1.15}$$

where τ_{GL}, the relaxation time of this diffusion equation, is defined

$$\tau_{GL} = \frac{\pi\hbar}{8k_B(T - T_c)}. \tag{1.16}$$

Using Eq. (1.15) and transforming it to a Fokker-Planck type equation, MH calculated the attempt frequency of Ω to be

$$\Omega_{MH} = \frac{L}{\xi}\sqrt{\frac{\Delta F}{k_B T}}\frac{1}{\tau_{GL}}. \tag{1.17}$$

Apart from the factor $(\Delta F/k_B T)^{1/2}$ which is of order unity, Eq. (1.17) can be interpreted by noting that at each point along the wire the attempt frequency is equal to $1/\tau_{GL}$; to get the total attempt frequency this local attempt frequency needs to be multiplied by X/ξ, the number of possible locations for a PS to occur.

The more accurate attempt frequency calculated by MH(Γ_{MH}) is of the order of 10^{10} smaller than Ω_{LA}; however, because of the exponential dependence on the temperature in Eq. (1.13), only a few mili-kelvin uncertainty in the temperature close to the critical temperature can cancel many order of magnitude in uncertainty of the attempt frequency. Combining the free energy barrier calculated by LA and the attempt frequency obtained by MH, the LAMH theory predicts the resistance of superconducting nanowires to be

$$R_{LAMH}(T) = R_q \frac{\hbar X}{\xi k_B T \tau_{GL}} \sqrt{\frac{\Delta F}{k_B T}} \exp\left(-\frac{\Delta F}{k_B T}\right). \tag{1.18}$$

Based on LAMH theory, the DC resistance decays exponentially bellow T_c. This can be seen by noting that $\Delta F \sim H_c^2 \xi s$, $H_c \sim (1-T/T_c)$ and $\xi \sim (1-T/T_c)^{-1/2}$ and as the result

$$R \sim \exp\left(-s\frac{(1-T/T_c)^{3/2}}{T/T_c}\right). \tag{1.19}$$

The vanishing of R_{LAMH} at T_c in Eq. (1.18) due to the divergence of ξ is the artefact of using GL theory which is invalid at temperatures very close to T_c.

According to the LAMH theory, the rate of TAPS is significantly suppressed at lower temperatures; therefore, no residual resistivity is expected away at temperatures much smaller than the critical temperatures. However, experiments revealed that the residual resistivity does not follow the exponential decay of the TAPS at low temperatures [8, 9]. This deviation from the LAMH model is attributed to the quantum phase slips (QPSs) which is the subject of the following section.

1.3.2 Phenomenological Theory of QPS

To explain the tail in the resistance of superconducting nanowires at low temperature, Giordano [8, 9] proposed the phenomenological model of QPS based on the theory of macroscopic quantum tunnelling (MQT) that was introduced in early 1980's by Caldeira and Leggett [15, 16]. Giordano argues that the phase difference of the order parameter $\Delta\varphi$ is quantized, therefore it can be treated quantum mechanically; hence, it is possible for the $\Delta\varphi$ to slips 2π by macroscopic quantum tunnelling without having to climb over the free energy barrier as shown in Fig. 1.5.

Giordano, heuristically, assumed that the rate of the QPS follows the same form as TAPS, provided that $k_B T$ is replaced with the quantum energy $\hbar/\tau_{GL}$. His argument can be understood in terms of the Heisenberg Uncertainty principle; a classically forbidden region with the energy height of ΔE, can be accessed for a short period of time of Δt as long as

$$\Delta E \sim \frac{\hbar}{\Delta t}. \tag{1.20}$$

For the physics of QPS, it follows that $\Delta E = \Delta F$ and $\Delta t = \tau_{GL}$. Eq. (1.20) for the case of TAPS would be for $\Delta F = k_B T$. Considering that the rest of the argument follows exactly the one for LAMH, the rate of QPS can be written as

$$\Gamma_{QPS} = b\frac{R_q X}{\xi}\sqrt{\frac{\Delta F \tau_{GL}}{\hbar}} \exp\left(-a\frac{\Delta F \tau_{GL}}{\hbar}\right). \tag{1.21}$$

Eq. (1.21) is obtained from Eq. (1.18) after the substitution of $k_B T \rightarrow \hbar/\tau_{GL}$ and including two numerical factors a and b of order unity to compensate the uncertainties in our derivation.

1.3.3 Microscopic Theory of QPS

The microscopic theory of QPS has been proposed by Golubev and Zaikin (GZ) [10, 11, 12, 13] that takes into account the effect of dissipation inside and outside of the phase slip core. Their approach is based on the imaginary time effective action of the superconducting nanowires (see Appendix A) that considers different effects of non-equilibrium dissipation and electrodynamics inside and outside the core during a QPS event.

The GZ theory offers many improvement over the phenomenological model of LAMH and Giordano which are based on TDGL. Unlike the TDGL theory that is only applicable close to T_c, GZ theory is valid down to $T = 0$ where QPSs become dominant. GZ model can explain the effect of quasi-particles inside and the excitation of the electromagnetic wave outside the QPS core, while TDGL can not.

The proper treatment of the electromagnetic field is crucial as QPSs are coupled to the environment. A longitudinal electromagnetic wave known as Mooij-Schon plasma mode [17] that propagates along superconducting nanowires , transfer the energy away from the QPS core to be dissipated elsewhere, e.g., the contact leads. If the dissipation gets too big, the barrier height can become large and therefore, the QPS rate can decrease significantly and even vanishes. GZ theory predicts QPS in wire with cross-section area of the order of 100 nm^2.

Some details of the derivation of the effective action of the GZ theory is given in Appendix A. Here, important results relevant to the calculation of the rate of QPS from the GZ theory is reviewed. According to the GZ theory the rate of a single QPS has the form:

$$\Gamma_{QPS} = \Omega \exp\left(-S_{QPS}/\hbar\right), \tag{1.22}$$

where S_{QPS}, the effective action, can be written as

$$S_{QPS} = S_{core} + S_{out}. \tag{1.23}$$

S_{core} contains information about the QPS center and is determined by the dissipation of the normal current in the core and the condensation energy. S_{out} considers the propagation of the electromagnetic fields out of the QPS core and has the form:

$$S_{out} = \mu \ln\left[\frac{\min(\frac{c_0\hbar}{k_B T}, X)}{\max(c_0\tau_0, x_0)}\right], \tag{1.24}$$

where τ_0 and x_0 are the typical duration and size of the QPS core respectively, and the parameter

$$\mu = \frac{\pi}{4\alpha}\sqrt{\frac{C}{L_k}}, \tag{1.25}$$

sets the scale for the electromagnetic hydrodynamic contribution. In the definition of μ, $\alpha = e^2/\hbar c$, C is the wire capacitance per unit length, $L_k = (4\pi\lambda_L^2/s)$ is the kinetic inductance per unit length, λ_L the magnetic penetration depth, and s is the cross section of the superconducting nanowire. In Eq. (1.24), c_0, the phase velocity of Mooij-Schon plasmon modes [17] is defined

$$c_0 = 1/\sqrt{L_k C}. \tag{1.26}$$

In Eq. (1.24), τ_0 and x_0 are determined from the minimization of the S_{core}. The dimensionless hydrodynamic factor μ characterizes the damping of the electromagnetic field inside the superconducting nanowire away from the QPS core. When $T \to 0$k , S_{out} diverges such that for long superconducting nanowires a single QPS event to happen is highly unlikely.

Evaluation of the S_{core} is a cumbersome task; however, if we restrict ourselves to just knowing S_{core} up to a numerical factor of order unity we can make use of trial functions for the magnitude and the phase of the order parameter that satisfy some dynamical requirements of a QPS. These conditions are: (1) $|\delta\Delta(x,\tau)|$ needs to vanish at $x = 0$ and $\tau = 0$; moreover, $|\delta\Delta(x,\tau)|$ needs to coincide with the mean field value outside of the QPS core. (2) $\varphi(x,\tau)$ should change by 2π across the core. One of the many choices of the trial functions are:

$$|\delta\Delta(x,\tau)| = \Delta_0 \exp\left(-\frac{x^2}{2x_0^2} - \frac{\tau^2}{2\tau_0^2}\right), \tag{1.27}$$

which $|\delta\Delta(x,\tau)|$ indicates the deviation from the mean field value Δ_0 and

$$\varphi(x,\tau) = -\frac{\pi}{2}\tanh\left(\frac{x\tau_0}{x_0\tau}\right). \tag{1.28}$$

Using the trial functions of Eqs. (1.27) and (1.28) and after minimizing S_{core} with respect to x_0 and τ_0, Golubev and Zaikin obtained:

$$\begin{aligned} x_0 &= a\sqrt{\frac{\hbar D}{\Delta_0}} = a\xi, \\ \tau_0 &= b\frac{\hbar}{\Delta_0}, \\ S_{core} &= \pi f N_0 s\sqrt{\hbar D\Delta_0} = f\frac{R_q X}{R_N\xi}, \end{aligned} \tag{1.29}$$

where N_0 is the density of the states at the Fermi level; and a, b and f are numerical factors of order one that depend on details of the trial functions. These numerical factors can be determined from fitting our results to the experimental data. It must be stressed that the above results are valid when the capacitive effects are small, i.e., short wires with lengths

$$X \ll \xi\frac{e^2 N_0 s}{C}. \tag{1.30}$$

This condition is satisfied for samples with lengths typically less than 10 μm [10, 11, 12, 13].

For short superconducting nanowires ($X < 10\,\mu$m), S_{core} is larger than the hydrodynamic part S_{out}; therefore, in minimizing S_{QPS} with respect to x_0 and τ_0, we can neglect the effect of the S_{out} and its contribution can be accumulated as a part of the constant factor f. Therefore the action of the QPS can be written:

$$S_{QPS} \approx S_{core} = f\frac{R_q X}{R_N\xi}. \tag{1.31}$$

Using the instanton method, Golubev-Zaikin calculated the pre-factor attempt frequency Ω to be:

$$\Omega = g\frac{S_{QPS}X}{\tau_0 x_0}, \tag{1.32}$$

where g is a numerical constant of order one. The QPS rate in the limit of zero current and short wire can be written

$$\Gamma_{QPS} \approx k\frac{\Delta_0 R_q X^2}{\hbar R_N\xi^2}\exp\left(-f\frac{R_q X}{R_N\xi}.\right), \tag{1.33}$$

where k again is a numerical factor in place of combinations of other numerical factors introduced above. The results of Eqs. (1.31) and (1.32) are approximations which are valid in short superconducting nanowires in the limit of zero current bias.

It is important to note that, in the case of a single QPS at a time in a superconducting nanowire, the electromagnetic part of the QPS could be neglected compared to S_{core}; however S_{out} determines the dynamic of the interaction between QPSs when there are more than one QPS events at the same time along the wire. In long wires, similar to Berezinskii-Kosterlitz-Thouless (BKT) type transition, superconducting nanowire can have a superconductor to metal (insulator) transition which is driven by the wire cross-section.

At low temperatures and finite current, GZ theory considers the effect of the logarithmic interaction between two bound pairs of QPS which becomes important. This interaction is not considered in the Giordano's model. The logarithmic interaction between two QPSs has the form:

$$S_{int} = \frac{\hbar\mu}{2} \ln\left(\frac{(x_1 - x_2)^2 + c_0^2(\tau_1 - \tau_2)^2}{\xi^2}\right). \tag{1.34}$$

By calculating the imaginary part of the free energy which is a measure of the metastability ($\Gamma = 2\text{Im}F$), GZ found the QPS rate for long wires ($X \gg c_0\hbar/k_BT$) to be:

$$\begin{aligned}\Gamma_{QPS} = \frac{Xy^2}{2\tau_0 x_0}\frac{\sqrt{\pi}\Gamma(\mu-1/2)}{\Gamma(\mu)\Gamma(2\mu-1)}&\left|\Gamma(\mu - \frac{1}{2} + i\frac{\Phi_0 I}{\pi 2ck_BT})\right| \\ &\times \exp\left(\frac{\Phi_0 I}{2ck_BT}\right)\left[\frac{2\pi\tau_0 k_BT}{\hbar}\right]^{2\mu-2},\end{aligned} \tag{1.35}$$

where the fugacity y is defined according to

$$y \sim \frac{S_{core}}{\hbar}\exp\left(-\frac{S_{core}}{\hbar}\right). \tag{1.36}$$

Consequently, the average voltage drop across a superconducting nanowire is found to be

$$\begin{aligned}V &= \frac{\Phi_0}{c}\left[\Gamma_{QPS}(I) - \Gamma_{QPS}(-I)\right] \\ &= \frac{X\Phi_0 y^2}{c\tau_0 x_0}\frac{\sqrt{\pi}\Gamma(\mu-1/2)}{\Gamma(\mu)\Gamma(2\mu-1)}\left|\Gamma(\mu - \frac{1}{2} + i\frac{\Phi_0 I}{\pi 2ck_BT})\right| \\ &\qquad \times \sinh\left(\frac{\Phi_0 I}{2ck_BT}\right)\left[\frac{2\pi\tau_0 k_BT}{\hbar}\right]^{2\mu-2},\end{aligned} \tag{1.37}$$

where $\Gamma(x)$ is the Euler gamma function. According to Ref. [13], at low temperatures ($T \ll \Phi_0 I$), the behaviour of the resistance R is found from Eq. (1.37) to be

$$R(T) = \frac{V(T)}{I} \propto y^2 I^{2\mu-3}, \tag{1.38}$$

which shows a nonlinear current-voltage characteristic. The resistivity in Eq. (1.38) is valid for very long wires and for low temperature ($T \ll \Phi_0 I$) but not very close to zero; moreover, it is required that $\mu > \mu^*$, where $\mu^* \approx 2$. Otherwise, unbound QPS would require accounting for many-body effects.

1.4 Applications of QPS Junction

In 2006, Mooij and Nazarov put forward a theory that would link the physics of coherent QPSs to the physics of Josephson junction [18]. In brief, according to this duality, a QPS junction and Josephson junction share dual dynamics upon appropreate transformation. A detailed account of this duality-theorem is presented in Appendix D. Based on this duality, a spectrum of applications can be envisioned for superconducting nanowires as source of coherent QPS. Amongst them are

- Qubit [19, 18, 20]
- Quantum Standard of Current [18, 21]
- Single Charge Transistor [22, 23]
- High-frequency Radiatio Detector (see Chapter 4)

In the following we look at the development in qubit and quantum standard of current applications. The radiation detector which is our contribution is differed to Chapter 4.

1.4.1 Quantum Phase Slip Qubits

In 2005, Mooij and Harmans [19] proposed that quantum phase slips (QPS) formed along thin wires can replace Josephson junctions in a qubit. The biggest advantage over Josephson junction qubits would be the absence of an oxide layer and hence a better noise and

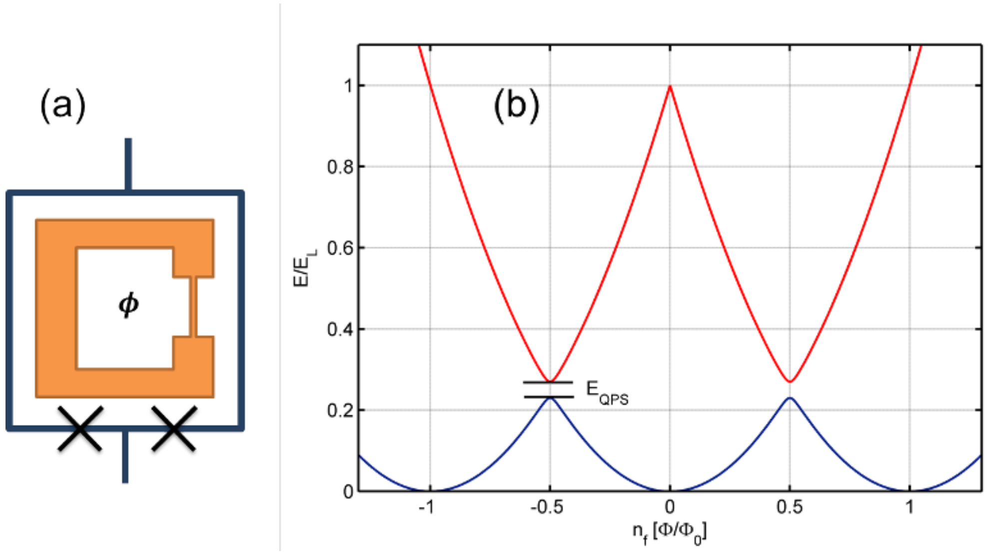

Figure 1.6: (a) The schematic of a proposed QPS qubit. A is the length of the thin wire where the QPS events take place. The outer circuit is a SQUID made of two Josephson junctions denoted by two crosses. (b) Energy levels of the system in terms of the applied magnetic flux is shown. The fluxoid number n_f is changed by each QPS event. The energy gap at the anti-crossings at $n_f = 1/2 + \mathbb{Z}$ equals the E_{QPS}

decoherence performance, which are the two main obstacles in the development of quantum computing. Moreover, the fabrication of superconducting nanowire is much easier compared to fabrication of Josephson junctions which is a multi-steps process.

If QPSs exist, then this effect can be used as a coherent coupling between two macroscopic states separated by the energy barrier. During a PS event, the energy of $I\Phi_0$ is dissipated where $\Phi_0 = hc/2e$ and I is the current. Consider a loop made of a superconducting material with a section made of a very thin wire and is biased with external magnetic flux; after a macroscopic quantum tunnelling event, the energy of the system would be the same but the persistent current will be reversed; therefore a QPS should result into a superposition of two opposed current states. The schematic of a QPS qubit is shown in Fig 1.6 . In Fig. 1.6(a) a thin wire in a closed superconducting loop is depicted. The two crosses denote two Josephson junctions in a superconducting quantum interference device (SQUID) for measuring the state of the qubit. The loop is biased with magnetic flux Φ. Fig. 1.6(b) shows energy levels as a function of applied flux. A QPS event can change n_f.

In 2012, Astafiev and collaborators reported the first experimental observation of coherent quantum phase slip [20]. In a narrow segment of a superconducting loop made of strongly disordered In_2O_3 on a SiO_2 substrate, they observed superposition of different quantum states labelled by their flux quanta. The narrow segment of the superconducting loop is 40nm ×400 nm and the thickness of the film is 35nm.

1.4.2 Quantum Standard for Electrical Current Based on QPS

One of the potential applications of QPS is in meteorology for a standard of current. At present, there exist reliable quantum standards for voltage and resistance based on the Josephson relation and the quantum hall effect respectively; however, a reliable quantum standard for current does not exist; although, there have been efforts based on Single Electron Transport since 1990s. The metrological triangle of electrical units is shown in Fig. 1.7(a). A new approach for a quantum standard of current is basd on QPS effect in a superconducting nanowire[21] . Based on theoretical predictions, a QPS junction behaves as an exact dual of a Josephson junction provided that the current and the voltage are exchanged [18]. For example, a Josephson junction at a low current behaves like a perfect conductor, and a QPS junction at low voltage acts as a perfect insulator (See Appendix D and Fiq. D.3). In Josephson junctions, we have control over the phase and the charge is not well defined, but in QPS, charge is a good quantum number despite phase fluctuations along the thin wire. During a QPS event, the stored charge remains fixed.

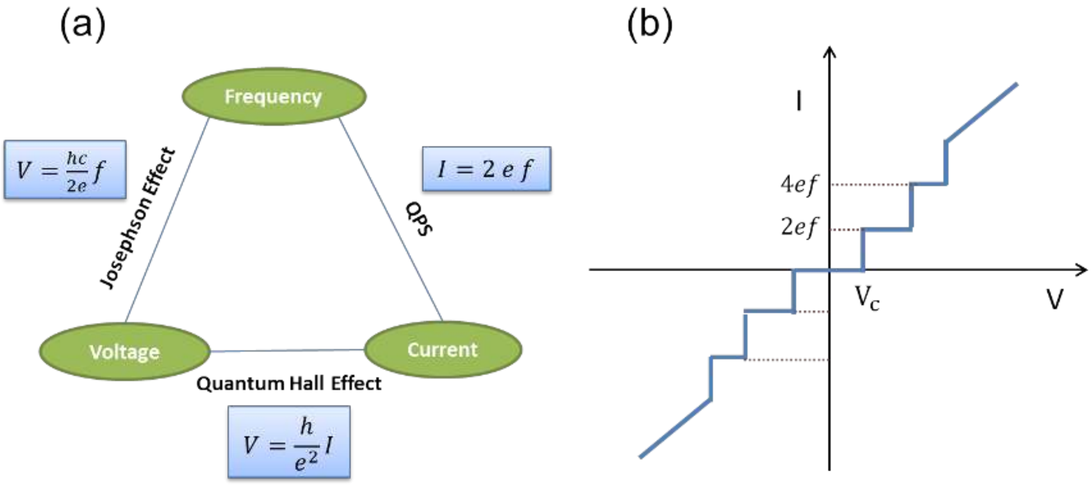

Figure 1.7: (a) The metrological triangle of electrical units [24]. Units of voltage and current are related to the quantum flux and fundamental electric charge by the Josephson and QPS effect with that of the frequency. Voltage and current are related by the von-Klitzing constant (h/e^2) through the quantum hall effect phenomenon. (b) The current-Voltage characteristic of a QPS junction under microwave irradiation of frequency f. The flat current plateau is used as the basis for a standard of current, [21, 25]

A Josephson junction biased with current exhibits flat voltage plateaux under microwave irradiation; this property is the basis for a voltage standard. Similarly, a voltage-biased QPS junction under irradiation has flat current plateaux that can be used for a standard of current. This is shown in Fig. 1.7(b).

1.5 Objectives of This Thesis

Our main task in this thesis is to better understand and control topological excitations in superconducting nanostructures. Topological excitations in 1D nanowires and 2D nanostrips are quantum phase slips (QPS) and vortices respectively. Our objectives from this study are to:

- Design novel devices using superconducting nanostructures
- Improve the performance of the existing quantum superconducting nanodevices

- Explore new physics

As we learned in this introduction, 1D Superconducting nanowires have a very rich physics and have great potential in many applications as an alternative to Josephson junctions, new qubits, quantum standard of currents and many more. Our goal is to better understand the effect of high-frequency field on 1D superconducting nanowires. The interaction of nano-structures and high-frequency field takes place in almost all applications. For this reason, we theoretically study the behaviour of 1D superconducting nanowires exposed to high-frequency electromagnetic field and calculate the complex conductivity from the effective action of the GZ theory using Kubo formalism. The results demonstrate deviation from the bulk conductivity in the nonlocal limit and similar to the bulk in the local limit. It will then be argued that the complex conductivity calculated from the Kubo formalism does not capture all the physics involved like the influence of the high-frequncy on the quantum tunnelling and QPS.

The study of the influence of the high-frequency field on the QPS within the GZ theory is very difficult, because GZ theory involves two dimensions, i.e., space (x) and time (t). To avoid this, we transform the problem to a Josephson junction type problem via the Mooij-Nazarov duality theorem. This transformation reduces the degree of freedom of the problem to one, i.e. charge (q). Therefore, the semi-classical techniques developed previously for the Josephson junction exposed to high-frequency field can be applied to the QPS case. By applying a similar method as deveoped by Ivelev and Mel'nikov, we obtain that the high frequency is capable of exponentially enhancing the rate of QPS in superconducting nanowires.

The observation of exponentially enhancement of the QPS rate becomes a motivation for proposing a novel high-frequency detector based on 1D superconducting nanowires. To show the plausibility of the realization of this type of detectors, different candidate materials are studied and design parameters are obtained.

In the second part of this thesis, 2D superconducting nanostrips which are mostly used in superconducting nanowire single photon detectors (SNSPDs) are studied. Vortices play an important role in the transport properties of thin films. This role becomes more significant as the thickness and the width of the nanostrips are reduced. In SNSPDs, vortex crossing is the major cause of the dark counts and the reduction of the quantum efficiency [26, 27]. In the vortex hopping, the vortices formed on the edges of the nanostrips due to the bias current enter the structure and cross the width of the wire. This crossing is a dissipative process that leaves a belt of normal state across the superconducting nanostrips. This normal belts results in dark count and lowering the quantum efficiency of SNSPDs. The rate of vortex hopping can be reduced by increasing the potential barrier of tunnelling across the superconducting nanowire. The potential barrier for the vortex hopping increases with the thickness and width and decreases with the bias current; however, increasing the thickness and width and decreasing the bias current adversely reduce the quantum efficiency of triggering an event in case a photon is absorbed in SNSPDs. The maximum current that a superconducting nanowire can support is directly related to the quantum efficiency of the triggering mechanism in SNSPD. The higher the bias current, the higher is the probability that an absorbed photon results in a click. In superconducting nanowires, the critical current density is always smaller than the critical current density of the bulk. The main reason for that is the proliferation of vortex crossing at high bias current. Therefore, vortex crossing is directly and indirectly a limiting factor in the performance of SNSPDs. Another major shortcoming of SNSPDs is the low probability of the photon absorption. This is because the thickness of the thin-film of about 4 nm to 6 nm is much smaller than the wavelength of the photon; moreover, the absorption coefficient of the material is limited. Increasing the thickness would improve the photon absorption rate but would suppress the quantum efficiency of triggering an event in case a photon is absorbed.

Our goal is to increase the photon absorption rate, increase the quantum efficiency and decrease the dark count rate, simultaneously. Curiously, all these objective can be met in a multilayer structure. The multilayer structure is designed such that the gap between layers is much smaller than the London penetration depth. London penetration depth is the scale at which a vortex varies in space. The gap is also large enough such that the Josephson current among layers is negligible and each layer is electrically isolated. In such a multilayer structure, it can be shown that the energy barrier for vortex crossing is elevated without compromising the quantum efficiency of the photon absorption. this results in a significant decrease in the vortex crossing. Due to a dramatic decrease in the vortex crossing, the dark count is significantly suppressed and the experimental critical current of the nanowire approaches the value of the bulk matter. Increase in the critical current directly improves the quantum efficiency of the photon detection.

Moreover, a multilayer structure significantly improves the photon absorption rate of the structure by increasing the optical path of the photon inside the detector. The absorption rate is an exponential function of the optical path in a superconductor which increases dramatically in multilayer structures.

1.6 Outline of This Thesis

Apart from the introduction; conclusions and outlook; and appendices, the present thesis is divided into two major parts: in Part I, the high frequency behaviour of 1D superconducting nanowires and in Part II, the motion of vortices in 2D superconducting nanostrips are studied. Details of each chapters are as follows:

Part I - 1D Superconducting Nanowires
In Chapter 2, the complex conductivity of a 1D superconducting nanowire is calculated from the effective action of GZ theory using the Kubo formalism. The local limit of the non-local complex conductivity of the 1D superconducting nanowire is then shown. In Chapter 3, the effect of a high frequency field on the rate of the QPS is calculated. Exponential enhancement in the quantum tunnelling rate in two limits of weak and strong dissipation is obtained. In Chapter 4, based on the result of the previous chapter, we outline a new type of high frequency detector based on the effect of high frequency field on QPS in superconducting nanowires.

Part II - 2D Superconducting Nanostrips
In Chapter 5, vortex physics in superconducting nanowire single photon detectors is the focus of the study. It will be shown that multi-layer structures would decrease the probability of dissipative tunnelling of vortices. This is demonstrated by calculating the energy barrier for vortex tunnelling. We will then discuss the effect of an increase in the potential barrier on the dark count rate and the critical current of SNSPDs. The increase in the optical absorption of photons in a multi-layer structure is calculated using the transfer matrix method.

Concluding Remarks and Appendices
In Chapter 6, our contributions and open problems are summarized. In Appendices A, the GZ effective action of the superconducting nanowires is presented. In Appendix B, the explicit form of the kernels used in the complex conductivity of superconducting nanowires are listed. In Appendix C, the concept of the semi-classical physics and quantum tunnelling in the semi-classical physics is reviewed. We then give the summary of the method of semiclassical physics in quantum tunnelling in the presence of high-frequency field introduced by [28]. In Appendix D the Mooij-Nazarov theory of the duality between QPS junctions and Josephson junction is presented. Dual equations and parameters are listed. In Appendix E, the physics of vortex in thin films which is the basis of our study in multi-layer structures is reviewed. In Appendix F the transfer matrix method that is used in calculating the optical absorption in multi-layer SNSPDs is given.

Part I

1D Superconducting Nanowires

Chapter 2

Complex Conductivity of Superconducting Nanowires

2.1 Introduction

In this chapter, the effect of low-dimensionality on the conductivity of superconducting nanowires is studied. We are interested in knowing how 1D superconductors differ from bulk material in terms of electromagnetic properties at high-frequncy. For this, the high frequency conductivity of the superconducting nanowires from the GZ theory is calculated. As we learned in the previous chapters and Appendix A, the GZ theory provides us with the effective action that governs the dynamics of the superconducting nanowires coupled to the electromagnetic field. In calculating the conductivity, in essence, what we do is to excite the superconducting nanowire with a time dependent electromagnetic field and observe how superconducting nanowires respond to that perturbation. What relates the induced current in the superconducting nanowire to the electromagnetic field is known as the complex conductivity $\sigma(\omega, k)$ defined as:

$$J(\omega, k) = \sigma(\omega, k)E(\omega, k), \tag{2.1}$$

where ω and k are the frequency and the wave vector of the electromagnetic field.

By exposing a system to a time dependent electromagnetic field, that system is driven out of equilibrium condition and therefore, the time dependence of the system needs to be considered. Non-equilibrium dynamics of the superconductors, in general, is a complicated subject to deal with; however, if the perturbation is not too strong and it is possible to assume that the system is still in the vicinity of an equilibrium state we can apply the method of the linear-response theory developed by Kubo [29]. In Kubo's formalism, expectation value of operators in the non-equilibrium case can be related to parameters that can be calculated within the equilibrium dynamics.

2.2 Complex Conductivity

In this section we calculate the complex conductivity of superconducting nanowires following Kubo's [1] method. The effective action of the GZ theory is written in terms of the electromagnetic potentials V and A, and not the electromagnetic fields E and B; therefore, it is easier to work, instead of σ with K defined by

$$J(x) = \int_{t'<t} d^2x' K(x, x')A(x') + \mathcal{O}(A^2). \tag{2.2}$$

The presence of a convolution integration implies that the conductivity can, in general, as we will see in the case of the superconducting nanowires, be non-local. The constraint on the temporal integration $t' < t$ simply ensures that causality is not violated [2].

In the gauge that scalar potential is set to zero, the electric field can be written as $E = -\frac{1}{c}\partial_t A$; therefore the conductivity σ can be obtained from K by

$$\sigma(\omega, k) = -\frac{c}{\omega} K(\omega, k)\Big|_{i\omega\to\omega+i0}. \tag{2.3}$$

Based on the Kubo's method the explicit knowledge of the current J is necessary, but we do not have that in our disposal; instead, we have the effective action that contains the electromagnetic potentials. We know that the current couples linearly to the vector potential in the form of

$$\delta S[\Delta, A] = \frac{s\hbar}{c}\int dx d\tau J.A; \tag{2.4}$$

therefore, we can write the current J as

$$J = \frac{c}{s\hbar}\frac{\delta S_c[\Delta, A]}{\delta A}. \tag{2.5}$$

---

[1] Kubo's formalism also known as the linear response method.

[2] The Kramers-Kronig relation is the result of this condition.

Here S_c is the part of the effective action that contains electromagnetic potential coupled to the current; hence, the kinetic part of the electromagnetic field in the action is not included. With this definition for the current, its expectation value can be written as

$$\begin{aligned}\langle J(x)\rangle &= -\frac{c}{s\hbar}\frac{1}{\mathcal{Z}}\frac{\delta}{\delta A(x)}|_{A=0}\mathcal{Z} \\ &= -\frac{c}{s\hbar}\frac{\delta}{\delta A(x)}|_{A=0}\ln\mathcal{Z},\end{aligned} \tag{2.6}$$

where $\mathcal{Z}$ is the partition function of the theory containing the electromagnetic potentials and the order parameters. Since our interest is in the linear response of the system to the electromagnetic field, the partition functional can be expanded to the first order in terms of the electromagnetic potentials according to

$$\mathcal{Z}[\Delta, A] \simeq \mathcal{Z}[\Delta, 0] + \int dx' \frac{\delta\mathcal{Z}[\Delta, A]}{\delta A(x')}|_{A=0}A(x'). \tag{2.7}$$

Using Eq. (2.7), Eq. (2.6) can be written

$$\langle J(x)\rangle = -\frac{c}{s\hbar}\int dx' \left(\frac{\delta^2}{\delta A(x)\delta A(x')}|_{A=0}\ln\mathcal{Z}[\Delta, A]\right)A(x'). \tag{2.8}$$

Comparing this with Eq. (2.8) and using Eq. (2.2) we can write

$$K(x, x') = -\frac{c}{s\hbar}\frac{\delta^2}{\delta A(x)\delta A(x')}\Big|_{A=0}\ln\mathcal{Z}[\Delta, A], \tag{2.9}$$

which simplifies further to

$$K(x, x') = -\frac{c}{s\hbar}\frac{1}{\mathcal{Z}}\frac{\delta^2}{\delta A(x)\delta A(x')}\mathcal{Z}[\Delta, A]\big|_{A=0}. \tag{2.10}$$

where we have assumed that the expectation value of the current with respect to the unperturbed action is zero.

Recalling the effective action that is in momentum space and taking into account the translational invariance of the response, i.e., $K(x - x')$, in the Fourier domain K can be written as

$$K(\omega, k) = -\frac{c2(2\pi)^2}{s\hbar}\frac{1}{\mathcal{Z}}\frac{\delta^2}{\delta A(\omega, k)\delta A^*(\omega, k)}\mathcal{Z}[\Delta, A]\big|_{A=0}. \tag{2.11}$$

In writing Eq. (2.11), it was used that in 1D nanowires the form of the current-potential interaction has the form

$$\delta S_c[\Delta, A] = \frac{s\hbar}{2}\int \frac{d\omega dk}{(2\pi)^2}\frac{1}{c}\left(A^*J + AJ^*\right). \tag{2.12}$$

The Euclidean effective action of a superconducting nanowire from the GZ theory from Eq. (A.16), is given by

$$\begin{aligned} S_E = \frac{s}{2}\int \frac{d\omega dk}{(2\pi)^2}\Big\{ & \frac{AA^*}{Lsc^2} + \frac{CVV^*}{s} + \hbar\tilde{\chi}_D(kVV^* + \frac{k\omega}{c}VA^* + \frac{k\omega}{c}V^*A + \frac{\omega^2}{c^2}AA^*) \\ & + \hbar\tilde{\chi}_J(VV^* - \frac{i\omega}{2e}V\varphi^* + \frac{i\omega}{2e}V^*\varphi + \frac{\omega^2}{4e^2}\varphi\varphi^*) \\ & + \hbar\frac{\tilde{\chi}_L}{4m^2}(k^2\varphi\varphi^* - \frac{i2ke}{c}\varphi A^* + \frac{i2ke}{c}\varphi^*A + \frac{4e^2}{c^2}AA^*) + \tilde{\chi}_\Delta|\delta\Delta|^2\Big\}. \end{aligned} \tag{2.13}$$

At this stage we can take advantage of the freedom to fix the gauge and remove the electric potential by choosing the gauge $V = 0$; hence, the action simplifies to

$$\begin{aligned} S_E = \frac{s}{2}\int \frac{d\omega dk}{(2\pi)^2}\Big\{ & \frac{AA^*}{Lsc^2} + \hbar\frac{\tilde{\chi}\omega^2}{c^2}AA^* + \hbar\frac{\tilde{\chi}_J\omega^2}{4e^2}\varphi\varphi^*) \\ & + \hbar\frac{\tilde{\chi}_L}{4m^2}(k^2\varphi\varphi^* - \frac{i2ke}{c}\varphi A^* + \frac{i2ke}{c}\varphi^*A + \frac{4e^2}{c^2}AA^*) + \tilde{\chi}_\Delta|\delta\Delta|^2\Big\}. \end{aligned} \tag{2.14}$$

Using Eq. (2.14), the response function, Eq. (2.11), is obtained

$$\begin{aligned} K_(p,\omega) = -\frac{1}{\mathcal{Z}[A]}\int D\varphi D\delta\Delta\Big\{ & -\Big(\frac{\tilde{\chi}_D\omega^2}{c} + \frac{\tilde{\chi}_L e^2}{m^2c}\Big) \\ & + \frac{s\hbar}{c2(2\pi)^2}\Big(\frac{\tilde{\chi}_L pe}{2m^2}\Big)^2\varphi^*(p)\varphi(p)\Big\}\exp(-S_E/\hbar). \end{aligned} \tag{2.15}$$

Some simplifications can be done by noting that in Eq. (2.15), the first term does not contain any field in the path integral and the second term can be written as the functional average; therefore we get

$$K_(k,\omega) = \Big(\frac{\tilde{\chi}_D\omega^2}{c} + \frac{\tilde{\chi}_L e^2}{m^2c}\Big) - \frac{s\hbar}{c2(2\pi)^2}\Big(\frac{\tilde{\chi}_L ke}{2m^2}\Big)^2\left\langle\varphi^*(k)\varphi(k)\right\rangle. \tag{2.16}$$

To calculate the correlation function in the second term, we can again exploit the fact that we are interested in the linear-response in terms of the vector potential; therefore, any terms containing the vector potential (A) in the calculation of the two point correlation function of the phase of the order parameter φ can be ignored. This significantly simplifies the calculation of the two points correlation function. The action is quadratic in terms of all the fields including φ; therefore, all path integral calculations reduce to the straightforward Gaussian functional integrations. The two-points correlation function of φs becomes the inverse of the coefficient of the quadratic part of φs according to:

$$\langle \varphi^*(k)\varphi(k)\rangle = \frac{2(2\pi)^2}{s\hbar}\frac{1}{\tilde{\chi}_J\frac{\omega^2}{4e^2}+\tilde{\chi}_L\frac{k^2}{4m^2}}. \tag{2.17}$$

From Eq. (2.17) and Eq. (2.16), it follows that

$$K(k,\omega) = \frac{\tilde{\chi}_D\omega^2}{c}+\frac{\tilde{\chi}_L e^2}{m^2 c}-\frac{\hbar(\tilde{\chi}_L k e)^2}{c(2m^2)^2\big(\tilde{\chi}_J\frac{\omega^2}{4e^2}+\tilde{\chi}_L\frac{k^2}{4m^2}\big)}. \tag{2.18}$$

Eq. (2.18), further, simplifies to

$$K(k,\omega) = \frac{\omega^2}{c}\Big(\tilde{\chi}_D+\frac{\tilde{\chi}_L\tilde{\chi}_J}{\tilde{\chi}_J\frac{\omega^2 m^2}{e^2}+\tilde{\chi}_L k^2}\Big). \tag{2.19}$$

Having the response function $K(\omega,k)$, the complex conductivity in Eq. (2.3) becomes:

$$\sigma(\omega,k) = -i\omega\Big(\chi_D+\frac{\chi_L\chi_J}{\chi_L k^2-\chi_J\frac{\omega^2 m^2}{e^2}}\Big), \tag{2.20}$$

where the χs are the real time version of the kernels introduced in Appendix A and are listed in Appendix B. In obtaining the Eq. (2.3), we have switched back to the real time from the Euclidean time (imaginary time) by the transformation $i\omega \to \omega$. We remind here that kernels with tildes are imaginary time version of the real time kernels (see Appendices B and A).

Eq. (2.20) is the main result of this chapter. In the next section, we will discuss in more details the physics behind the complex conductivity of superconducting nanowires that we obtained in Eq. (2.20).

2.3 Disscussion

The complex conductivity of 1D superconducting nanowires in Eq. (2.20), in addition to ω, depends on the wave vector k through the kernels which makes it non-local. We note that, curiously, in the local limit σ which happens for the case of $k \to 0$, Eq. (2.20) coincides with the conductivity of the bulk σ_{BM}, obtained by Mattis and Bardeen [30]; the conductivity of the bulk is given

$$\sigma_{MB}(\omega) = -i\omega\Big(\chi_D - \frac{e^2\chi_L}{\omega^2 m^2}\Big). \tag{2.21}$$

This can be interpreted this way that in small scales, which correspond to small wave vectors ($k \to 0$), the conductivity is not altered by the shrinkage in size. Restricting to local-small scales, effects from the bulk of the sample are negligible.

It is convenient to write the complex conductivity in terms of its real and imaginary parts

$$\sigma = \sigma_1 + i\sigma_2 \tag{2.22}$$

where the sign of the imaginary part is an arbitrary convention. The real part of the complex conductivity is responsible for absorption of the electromagnetic field in a superconducting nanowire. The energy absorbed for electromagnetic field E per unit volume is $\sigma_1 E^2$.

In Eq. (2.20), the complex conductivity $\sigma(\omega, k)$ depends on kernels χ_D, χ_J andχ_L which come from calculating Feynman's loop diagrams in the derivation of the effective action [10, 11, 12, 13]. The closed analytical form for χs kernels, in general, are not known; however, in some limits, they are available. We are are mostly interested in the low temperature limit where QPSs dominate; hence, in the limit of $T = 0$ and $\hbar D k^2 \ll \hbar\omega, \Delta_0$ the kernels can be calculated [13]. In this limit, the complex conductivity in Eq. (2.21) for $k = 0$ becomes:

For $\hbar\omega < 2\Delta_0$

$$\begin{aligned} \sigma_1(\omega) &= 0, \\ \sigma_2(\omega) &= \frac{2\sigma_D\Delta_0}{\hbar\omega}\mathrm{E}\big(\frac{\hbar\omega}{2\Delta_0}\big). \end{aligned} \tag{2.23}$$

For $\hbar\omega > 2\Delta_0$

$$\sigma_1(\omega) = \sigma_D\left[(1 + \frac{2\Delta_0}{\hbar\omega})\mathrm{E}(\frac{\hbar\omega - 2\Delta_0}{\hbar\omega + 2\Delta_0}) - \frac{4\Delta_0}{\hbar\omega}\mathrm{K}(\frac{\hbar\omega - 2\Delta_0}{\hbar\omega + 2\Delta_0})\right], \tag{2.24}$$

$$\sigma_2(\hbar\omega) = \sigma_D \left[\hbar \mathrm{E}(\frac{2\Delta_0}{\hbar\omega}) - (1 - \frac{4\Delta_0^2}{(\hbar\omega)^2}) \mathrm{K}(\frac{2\Delta_0}{\hbar\omega}) \right]. \tag{2.25}$$

To show the equivalence of Eqs. (2.23) and (2.24) with the results of Ref. [30], the following identities of the elliptic functions have been used:

$$\begin{aligned} K(t) &= (1+r)K(r), \\ E(t) &= (1+t')E(r) - t'K(t), \end{aligned} \tag{2.26}$$

with $t' = (1-t^2)^{1/2}$ and $r = (1-t')/(1+t')$.

In Eqs. (2.23) and (2.24), σ_D is the Drude conductivity of the normal metal defined by

$$\sigma_D = 2e^2 N_0 D, \tag{2.27}$$

where N_0 is the density of states at the Fermi level and D is the diffusion constant defined

$$D = \nu_F l/3. \tag{2.28}$$

The local complex conductivity in the limit of $T = 0$ and $\hbar D k^2 \ll \hbar\omega, \Delta_0$ is plotted in figure (2.1).

The real part which is related to the absorption of the electromagnetic field in the superconductor is zero for $\hbar\omega < 2\Delta$. This is because, at small frequencies, photons are not energetic enough to break Cooper pairs and since there are no quasi-particles available at $T = 0$, the absorption is zero. For $\hbar\omega > 2\Delta_0$, photons can break Cooper pairs and create quasi-particles that participate in conduction; these quasi particles can dissipate energy. At higher frequencies, $\approx 10\Delta_0$, all the Cooper pairs are broken and superconducting nanowires behave like a normal metal. therefore; at optical frequencies there is no difference between superconductors and normal metals in terms of conductivity.

The imaginary part of the conductivity becomes divergent at $\omega = 0$; this shows the acceleration of the supercurrent in the absence of any dissipation for small frequencies.

2.4 Concluding Remarks

In this chapter, the complex conductivity of superconducting nanowires from the effective action of the GZ theory was calculated. The complex conductivity that we obtained differs from the bulk obtained by Mattis-Bardeen [30]; however, in the local case ($k = 0$), the complex conductivity of superconducting nanowires coincides with the bulk. We,

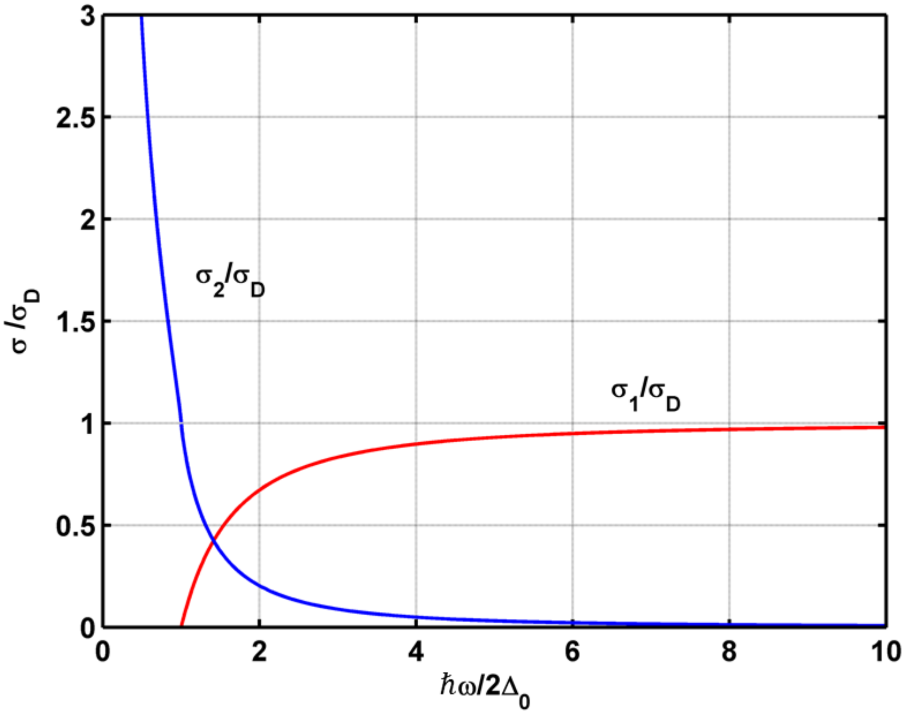

Figure 2.1: Plot of the local complex conductivity of superconducting nanowires in the limit of $T = 0$ and $\hbar D k^2 \ll \hbar\omega, \Delta_0$. Conductivity is normalized by the Drude conductivity of the normal metal. σ_1 is zero for frequencies bellow 2Δ, and approaches σ_{1n} of normal metal for high frequencies. σ_2 is divergent at $\omega = 0$.

analytically, calculated the conductivity in the limit of $T = 0$ and and $\hbar Dk^2 \ll \hbar\omega, \Delta_0$. For arbitrary, T, ω and Dk^2, numerical integration of the kernels is needed.

Superconducting nanowires are in the dirty limit which makes the local limit a good approximation. The local approximation is also a good approximation for even wavelengths up to visible light; however, we know that at such high frequencies the superconductors behave like normal metal.

A possible explanation for the complex conductivity of the superconducting nanowire being identical to the bulk in the local limit is that the complex conductivity was calculated in the linear-response regime; whereas, deviation might occur if nonlinear responses is studied.

In calculating the complex conductivity of superconducting nanowires in the path integral formalism, instantonic effects were not taken into account. Instantons are non-trivial solutions of the path integral in imaginary time that correspond to quantum tunnelling. As it will be explained in details in the next chapter, it is expected that a high frequency field would increase the QPS rate; therefore, we expect that a high frequency field would change the DC conductivity of the superconducting nanowire. This effect, however, can not be captured in a perturbation calculation as we did in this chapter. It is worth pointing out that a QPS effect occurs in the scale of ξ which is typically less than 10 nm. This disturbance in the density of cooper pairs is much smaller than the wavelength of even visible light; therefore, for high frequency fields of up to visible light we do not expect a significant change in the high frequency complex conductivity. In the next chapter we study the effect of the high frequency field on the QPS rate and its effect on the DC conductivity.

Chapter 3

Stimulation of Quantum Tunnelling by a High-frequency Field in Zero-current State of a 1D Superconducting Nanowire

3.1 Introduction

In the previous chapter, the complex conductivity of 1D superconducting nanowires from the Golubev-Zaikin effective action was calculated. The linear response method that was used is based on the perturbation theory, i.e., the expansion in the current-current correlation in terms of the lowest order correction. This method, however, is not capable of accounting for non-perturbative corrections in the conductivity which in this case is the corrections due to quantum tunnelling.

The manifestation of the QPS is the residual resistivity that is observed in superconducting nanowires at sufficiently low temperatures when the thermal activation is suppressed [31, 13]. Intuitively, it is expected that a high frequency field would increase the QPS rate in the superconducting nanowire. Therefore, we expect that a high frequency field would increase the DC resistivity of the superconducting nanowire.

At first glance, the straight-forward approach in investigating the effect of high frequncy field is to generalize the method used by Golubev and Zaikin in the non-driven case to the case of time periodic driven potential due to the alternating field. This would require calculating the instantonic contribution to the effective action and then finding the rate of the tunnelling by calculating the rate $\Gamma = 2\mathrm{Im}\{F\}$. An obvious complication arises from the fact that we need to calculate the imaginary part of the free energy (F) in a time dependent (non-equilibrium) setting; however, the free energy is defined for an equilibrium state. Therefore, the applicability of this method is not obvious. Moreover, in calculating the imaginary part of the free energy, at the final stage, analytic continuation of the time parameter is required which becomes mathematically more involved when an alternating contribution is added.

The major source of difficulty is that the effective action depends on two parameters x and τ, which requires double integration and then analytical continuation. To avoid the presence of two parameters x and τ in the theory, we exploit the duality property of the QPS to the Josepshon junction phenomenon. Josephson junction relations can be described solely in terms of one field, φ, which is the phase difference between two superconducting electrodes of a junction and one parameter t. The detailed account of duality between QPS and Josephson junction is presented in Appendix D.

According to the QPS-Josephson junction duality, the behaviour of a superconducting nanowire in the regime $E_{QPS} \gg E_L$ is described by the classical field q and one parameter t, where q indicates the charge number. This dynamics is dual to the classical dynamics of a resistively shunted Josephson junction. Using the duality, results obtained for Josephson junctions can be translated for the case of QPS.

The effect of an alternating bias current on thermal activation of Josephson junction has been observed [32], where the microwave radiation increases the rate of thermal activation. The physics of this increase in the activation is that phase φ which behaves as a particle in the titled washboard potential gains energy from the alternating field and therefore the height of the energy barrier for thermal activation is reduced. The same behaviour is expected for quantum tunnelling where the widths of the tilted washboard potential is smaller for excited states. This leads to an increase in the rate of quantum tunnelling which results in larger DC resistivity.

In a previous study [33], superconducting nanowires were subjected to microwave irradiation at high power and frequencies in the range of 2 GHz to 15 GHz. AT low temperatures they observed a reduction in the switching current and it was concluded that the microwave irradiation causes enhancement of QPS . They even observed Shapiro steps. In [33], in order to calculate the effect of the microwave irradiation on the switching current distribution, the irradiation is modelled as an alternating bias current and the potential barrier for the QPS is time-averaged over a period of the high frequency field.

The quantitative analysis in [33] does not explain the physics how the enhancement is

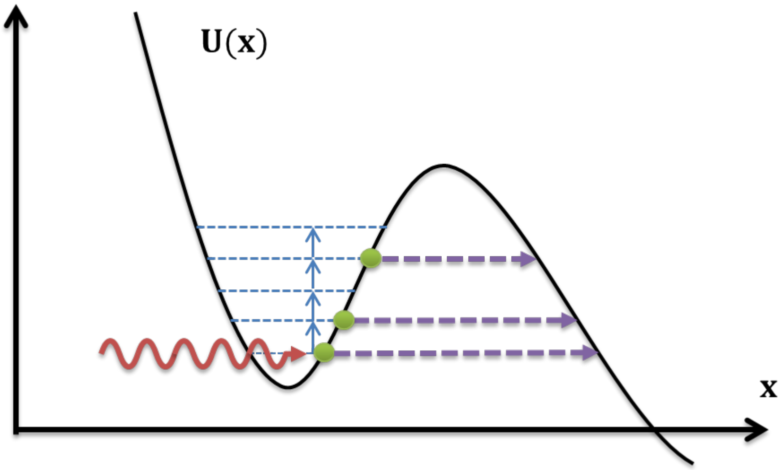

Figure 3.1: Quantum tunnelling of a particle from the metastable potential barrier under the influence of a high frequency field is shown. If the frequency of the incoming field matches the energy spacing between states, the particle can absorb one or more photons and tunnel at higher energies. The higher number of photon absorption leads to higher energy and easier tunnelling; however, multi photon processes becomes less probable.

induced in the superconducting nanowire. Also, in the time-averaging process the effect of the multi-photon process is not considered.

Here, we analyse the effect of weak high frequency irradiation on the superconducting nanowire. In our analysis the probability of multi-photon processes in the enhancement of QPS is considered. In a multi-photon process, the charge that is trapped in a local minima can absorb a photon and then tunnel or with a lower probability absorb two photon and then tunnel and so forth. Absorption of more photons is less probable; however, upon absorption of more photons, the energy gap between the energy of the system and the peak of the potential barrier decreases; therefore the probability of the quantum tunnelling increases. This situation is shown in Fig. 3.1.

Our chosen approach in investigating the dynamics of superconducting nanowire in the high frequency field, is to first use the QPS-Josepshon junction duality to reduce the dynamics of the system to a one-dimensional problem. Second, use the semiclassical quantum mechanic approach developed by Ivlev and Mel'nikov [28, 34, 1] in studying quantum tunnelling in a high-frequency field to our problem. The theory of semi-classical quantum physics and its application in studying the effect of high-frequency field in tunnelling for a

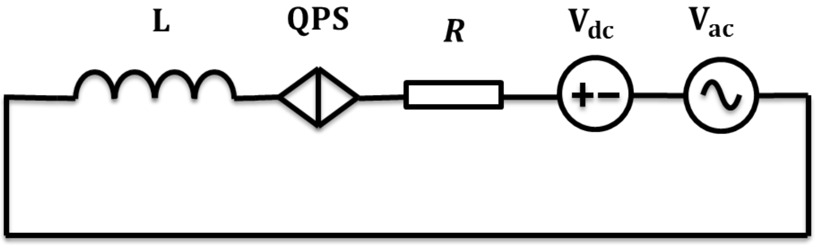

Figure 3.2: The schematic circuit of a QPS junction including an ideal QPS element (a superconducting nanowire), the dissipative element R, the bias voltage V_{dc} and the driving source V_{ac}. The inductor contains both the kinetic inductance and geometric inductance ($L = L_k + L_g$). In superconducting nanowires $L_k \gg L_g$, therefore, $L = L_k$.

general system is reviewed in details in the Appendix C.

3.2 Modelling of a QPS Junction in a High-frequency Field

Our starting point is the circuit shown in Fig. 3.2, where the effect of a high frequency field is modelled as an alternating voltage source in series with a bias DC voltage. The inductor L is total of the kinetic inductance (L_k) and the geometric inductance (L_g) of the circuit. In superconducting nanowire, the kinetic inductance is much larger than the geometric inductance and hence, the geometric inductance can be ignored; therefore, we have:

$$L \approx L_k. \tag{3.1}$$

We also assume that $E_{QPS} \gg E_L$. This condition is well satisfied for sufficiently long wires. In this limit, charge is well defined and localized, whereas phase is subject to large fluctuations (see App. D). In this case the charge can be modelled as a classical field.

Using the Eq. (D.8) from Appendix D, the equation of motion of a QPS junction shown in Fig. 3.2 can be written as

$$2eL_k\frac{d^2q}{dt^2} + 2eR\frac{dq}{dt} + V_c \sin(2\pi q) = V_{dc} + V_{ac}\cos\Omega t, \tag{3.2}$$

where Ω is the frequency of the driving voltage. The factor of 2π behind q can be absorbed by the change of variable to:

$$2\pi q \to Q. \tag{3.3}$$

Eq. (3.2) then becomes

$$L_k \frac{2e}{2\pi}\frac{d^2Q}{dt^2} + R\frac{2e}{2\pi}\frac{dQ}{dt} + V_c \sin Q = V_{dc} + V_{ac}\cos\Omega t. \tag{3.4}$$

For further convenience, Eq. (3.4) can be written as:

$$\frac{d^2Q}{dt^2} + \eta\frac{dQ}{dt} + \omega_p^2\left(\sin Q - k_{dc} - k_{ac}\cos\Omega t\right) = 0 \tag{3.5}$$

where the following parameters have been introduced:

$$\begin{aligned} V_c &= \frac{2\pi}{2e}E_{QPS}, \\ \eta &= \frac{R}{L_k}, \\ \omega_p &= \sqrt{\frac{2\pi V_c}{2eL_k}}, \\ k_{dc} &= \frac{V_{dc}}{V_c}, \\ k_{ac} &= \frac{V_{ac}}{V_c}. \end{aligned} \tag{3.6}$$

The definition of the plasma frequency ω_p is compatible with the definition in Table D:

$$\begin{aligned} \omega_p &= \frac{1}{\hbar}\sqrt{2E_{QPS}E_L} \\ &= \frac{1}{\hbar}\sqrt{2\frac{2eV_c}{2\pi}\frac{h^2}{2(2e)^2L_k}} \\ &= \sqrt{\frac{2\pi V_c}{2eL_k}}, \end{aligned} \tag{3.7}$$

where the inductive energy is defined

$$E_L = \frac{\phi_0^2}{2L_k}, \tag{3.8}$$

where $\phi_0 = h/2e$. The Eq. (3.5) is similar to the equation of RCSJ model of Josephson junction [35, 36], with high-frequency driving field. The effect of the high-frequency field on the quantum tunnelling of the RCSJ model is studied by Ivelev and Mel'nikov [1, 34, 28, 37] that we follow here and apply it to the QPS case.

It needs to be stressed that what we are interested in studying here is different from the physics of the Shapiro steps [38]. In the physics of Shapiro steps, the amplitude of the high-frequency field is large and the Josephson junction is driven into non-zero-voltage-state; consequently, the phase of the Josephson junction is locked to the frequency of the high-frequency field and therefore constant voltage steps are observed. However, in what follows, we assume that the amplitude of the high-frequency driving field is very small ($V_{ac} \ll V_c$) and we are in the zero-current state of the QPS junction ($V_{dc} < V_c$). However, the smallness of V_{ac} does not necessary indicate that the effect itself would be small. As it will be shown, the effect can be exponentially large (see also Appendix C.1.1).

In the following we will study the decay of the zero-current state in two limits of weak and strong dissipation. In the limit of weak dissipation ($R = 0$), the system can be studied by 1D quantum mechanics. In contrast, inclusion of dissipation will require extra steps and techniques that will be studied later in this chapter [16, 15].

3.3 Weak Dissipation

In the limit of weak dissipation ($R = 0$), the Lagrangian of the system can be obtained from Eq. (3.5) and is

$$\mathcal{L} = \frac{E_{QPS}}{2\omega_p^2} \left(\frac{dQ}{dt} \right)^2 + E_{QPS} \left(\cos Q + k_{dc} Q + k_{ac} Q \cos \Omega t \right). \tag{3.9}$$

From Eq. (3.9), the time-independent potential in the absence of the alternating field is given by

$$V(Q) = -E_{QPS}(\cos Q + k_{dc} Q), \tag{3.10}$$

which is a tilted washboard potential. For semi-classical description to be valid, it is required that $E_{QPS} \gg \Omega \gg 1/\tau_s$; moreover, since the approach chosen here is adiabatic in nature, it is necessary to have $\Omega/2\pi \ll 1/\tau_c$, where τ_c is the characteristic relaxation time of the system [37]. According to Eqs. (C.7) and (C.15), the probability of tunnelling is given by

$$\begin{aligned}
&\Gamma \approx \exp\left(-S\right), \\
&S_0 = -i\int_{C_-+C_+} dt\left[\frac{E_{QPS}}{2\omega_p^2}\left(\frac{dQ}{dt}\right)^2 - V(Q)\right], \\
&S_1 = -iE_{QPS}k_{ac}\int_{C_-+C_+} dtQ(t)\cos\Omega t,
\end{aligned} \tag{3.11}$$

where the contour of integration is shown in Fig.C.1. In Eq. (3.11), $Q(t)$ is the solution to

$$\frac{d^2Q}{d\tau^2} - \omega_p^2\left(\sin Q - k_{dc}\right) = 0, \tag{3.12}$$

which is obtained from Eq.(3.5) with $\eta = 0$ and $t \to i\tau$. Eq. (3.12) can be viewed as the equation of motion of the particle Q in the inverted potential V in Eq. (3.10).

To solve Eq. (3.11), the singularities of the unperturbed problem are extracted from the relation

$$\omega_p t = \sqrt{\frac{E_{QPS}}{2}}\int dQ\frac{1}{\sqrt{E - V(Q)}}, \tag{3.13}$$

The dynamics of $Q(t)$ follows the shape of the potential in Fig.3.3 where the point particle Q is trapped in one of the valleys and the classical turning points are determined by

$$V(Q_{1,2,3}) = E. \tag{3.14}$$

The energy E in Eqs.(3.13) and (3.14) is determined from the condition that the time of the under-barrier motion between Q_1 and Q_2 is $i/2k_BT$ according to Eq.(C.13). Using Eq.(3.13), we get

$$\frac{\omega_p}{k_BT} = \sqrt{2E_{QPS}}\int_{Q_2}^{Q_3} dQ\frac{1}{\sqrt{V(Q) - E}}. \tag{3.15}$$

The singularities of the trajectory correspond to the points where $V(Q)$ becomes infinite. The singularities are of the logarithmic form and are given by [37]

$$\begin{aligned}
Q_1(t) &= +2i\ln\left[\omega_p\left(t - i\tau_s + t_1\right)\right], \\
Q_2(t) &= -2i\ln\left[\omega_p\left(t - i\tau_s - t_1\right)\right], \\
Q_3(t) &= -2i\ln\left[\omega_p\left(t + i\tau_s + t_1\right)\right], \\
Q_4(t) &= +2i\ln\left[\omega_p\left(t + i\tau_s - t_1\right)\right],
\end{aligned} \tag{3.16}$$

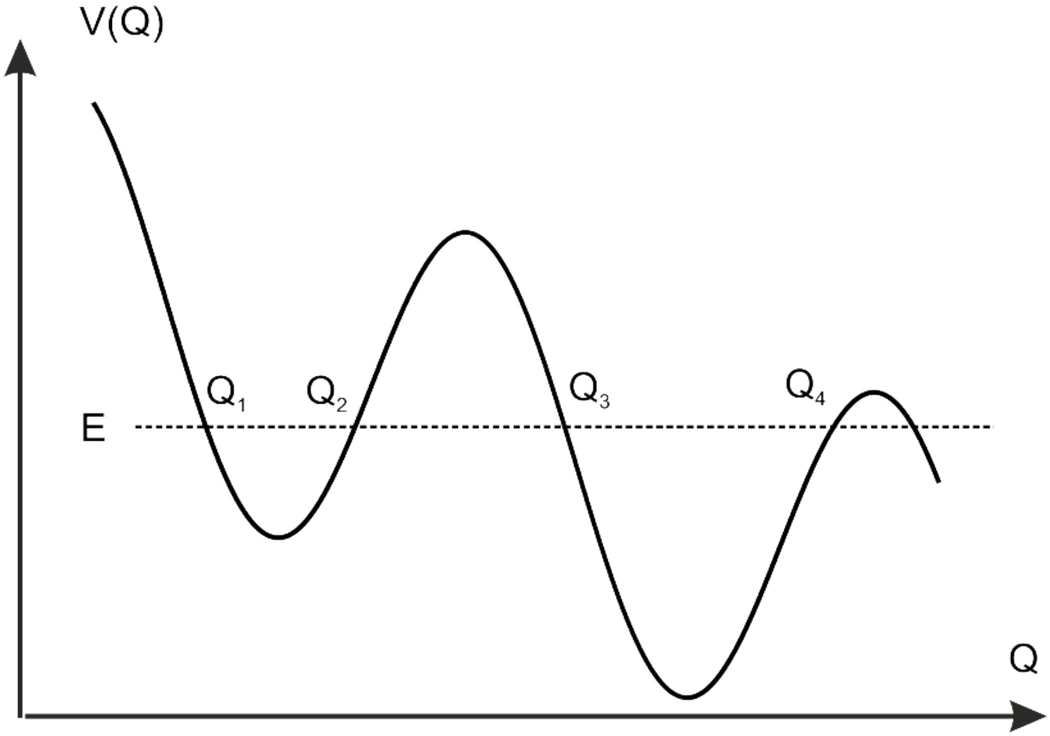

Figure 3.3: The tilted washboard potential $V(Q)$ and the classical turning points are shown. The motion between Q_1 and Q_2 is classically allowed; whereas, the motion between Q_2 and Q_3 happens through quantum tunnelling.

where

$$\omega_p(i\tau_s + t_1 - \frac{1}{2}t_0) = \left(\frac{E_{QPS}}{2}\right)^{1/2} \int_{Q_3}^{i\infty} dQ \frac{1}{\sqrt{E - V(Q)}}, \tag{3.17}$$

and the oscillation period in the classically allowed region of the potential well is given by [37]

$$\omega_p t_0 = \sqrt{2E_{QPS}} \int_{Q_1}^{Q_2} dQ \frac{1}{\sqrt{E - V(Q)}}. \tag{3.18}$$

The motion of the Q in the classically allowed region (between Q_1 and Q_2 in Fig. 3.3) is periodic with period t_0; hence, singularities in Eq. (3.16) are also repeated with period t_0. Therefore, the integration contour in Eq. (3.11) can be made into a square containing only the four singularities given in Eq. (3.16). Using Eq. (3.16) in Eq. (3.11), and after time averaging [1] the probability of the tunnelling is found to be

$$\Gamma(V_{ac}) = \Gamma_0 \exp\left[\frac{4eV_{ac}}{\hbar\Omega}\left|\frac{\sin\Omega t_1}{\sin\Omega t_0/2}\right| \exp\Omega\tau_s\right], \tag{3.19}$$

where Γ_0 is the tunnelling probability without the oscillating field ($V_{ac} = 0$). The calculation of t_0, t_1 and τ_s is done numerically in [1] for the case of Josephson junction and are adopted in Fig. 3.4.

The above calculations are valid as long as the quantum tunnelling is the dominant form of the decay of the metastable state. This requires the temperature to be bellow the cross over temperature (T_0) from thermal activation to the quantum tunnelling. In the dissipation-less case the cross over temperature is given by:

$$T_0 = \frac{\hbar\omega_p}{2\pi k_B}\left(1 - k_{dc}\right)^{1/4}. \tag{3.20}$$

The resonance effect that can happen in Eq. (3.19) when $\Omega t_0/2 = n\pi$ for integer n is the artefact of considering the linear contribution to the tunnelling probability due to the alternating current. Linear contribution in this semi-classical approach makes energy levels equidistant. The resonance effect will smear out, if correction due to higher order correction in V_{ac} is considered.

3.3.1 QPS Junction with Dissipation

In the case where the QPS junction has a finite dissipation ($\eta \neq 0$), the Lagrangian formalism of the dissipation-less case can not be directly applied. Instead the theory developed by Caldeira and Leggett [15, 16]; and also by Larkin and Ovchinnikov [39] can be used to take into account the effect of the dissipation on the quantum tunnelling. In those theories, dissipation is modelled as the coupling of the system to bosonic degrees of freedom of the environment. Then, the low-energy effective action of the system is derived to properly take account of the dissipation [15, 16, 39]. In analogy to the Josephson junction [39, 1], in the semiclassical limit, the effective action of a QPS junction with dissipation can be written as:

$$\begin{aligned} S = &- iE_{QPS}\int_C \left\{ \frac{1}{2\omega_p^2}\left(\frac{dQ}{dt}\right)^2 + \cos Q + k_{dc}Q + k_{ac}Q\cos\Omega t \right. \\ &\left. + \frac{4ik_B^2\pi\eta T^2}{\hbar^2\omega_p^2}\int_C \frac{dt_1}{\sinh^2\left[\pi k_B T(t_1 - t)/\hbar\right]}\sin^2\frac{Q(t) - Q(t_1)}{4}\right\} dt, \end{aligned} \tag{3.21}$$

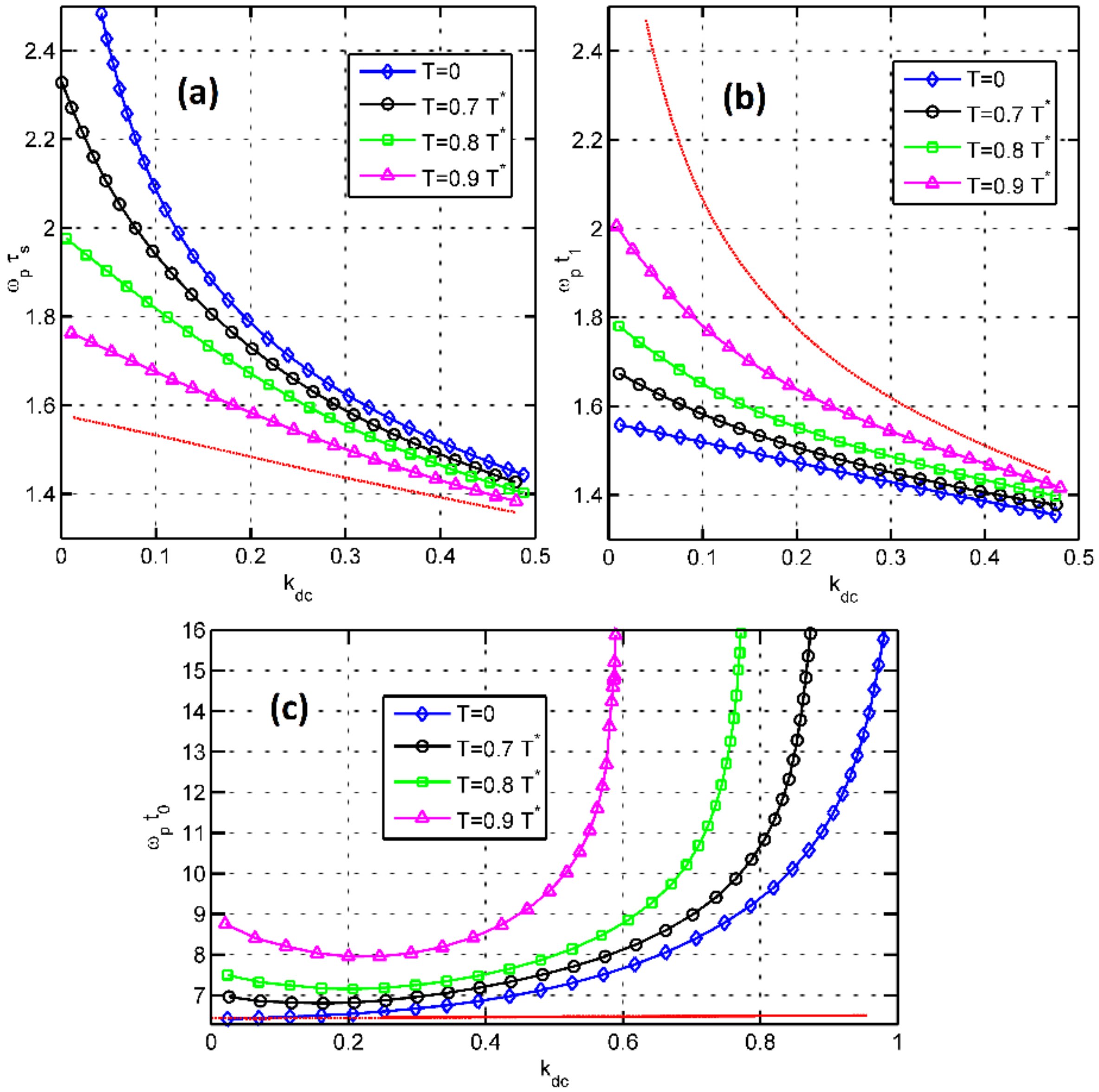

Figure 3.4: Numerical values of τ_S, t_0 and t_1 at four different temperatures. Here, $T^* = \omega_p\hbar/2\pi k_B$. The dotted red lines correspond to boundaries of the crossover from quantum tunnelling to thermal activation. Graphs are adopted from [1].

where the contour C is shown in Fig. C.1. The equation of the motion from the variation of Eq. (3.21) is given by

$$\begin{aligned}&\frac{d^2Q}{dt^2}+\eta\frac{dQ}{dt}+\omega_p^2\left(\sin Q-k_{dc}-k_{ac}\cos\Omega t\right)-\\&\qquad 2i\pi\eta T^2\int_{\tilde{C}}\frac{dt_1}{\sinh^2\left[\pi k_BT(t_1-t)/\hbar\right]}\sin\frac{Q(t)-Q(t_1)}{2}=0\end{aligned} \tag{3.22}$$

where the difference between $\tilde{C}$ and C is that close to $t=t_1$, it is a semicircle inside C. This requires adding a half residue term for compensation.

In the limit of the strong dissipation $\eta\gg\omega_p$ and close to the critical current ($1-k_{dc}\ll 1$), the term with second derivative can be omitted. In this limit, the time of the under-barrier motion is given by [1] :

$$\tau_s=\frac{\eta}{\omega_p^2}. \tag{3.23}$$

Following the same procedure as in the limit of weak dissipation, similar to Josephson jnction case [37], the tunnelling probability in the presence of an alternating current in the limit of strong dissipation becomes

$$\Gamma(V_{ac})=\Gamma_0\exp\left[\frac{4eV_{ac}}{\hbar\Omega}\sinh\frac{\Omega\eta}{\omega_p^2}\right], \tag{3.24}$$

where Γ_0 is the tunnelling probability in the absence of the high-frequency field. Eq. (3.24) is valid for $T<T_0$ where T_0 is the crossover temperature from the quantum tunnelling to the thermal activation regime given by:

$$T_0=\frac{\hbar\omega_p^2}{2\pi k_B\eta}\left[2(1-k_{dc})\right]^{1/4}. \tag{3.25}$$

The enhancement of the tunnelling probability in Eq. (3.24) is shown in Fig.3.5 for parameters $V_{ac}/V_c=0.1$, $\eta/\omega_p=10$ and $4eV_c/\omega_p=10$.

3.4 Discussion

Plugging the relevant parameters for the QPS junction in Eq. (3.24) from Eqs. (3.6) and (3.8) we obtain:

$$\Gamma(V_{ac})\approx\frac{E_{QPS}}{\hbar}\exp\left[\frac{4eV_{ac}}{\hbar\Omega}\sinh\frac{\hbar^2\Omega R}{2E_{QPS}E_LL_K}\right]. \tag{3.26}$$

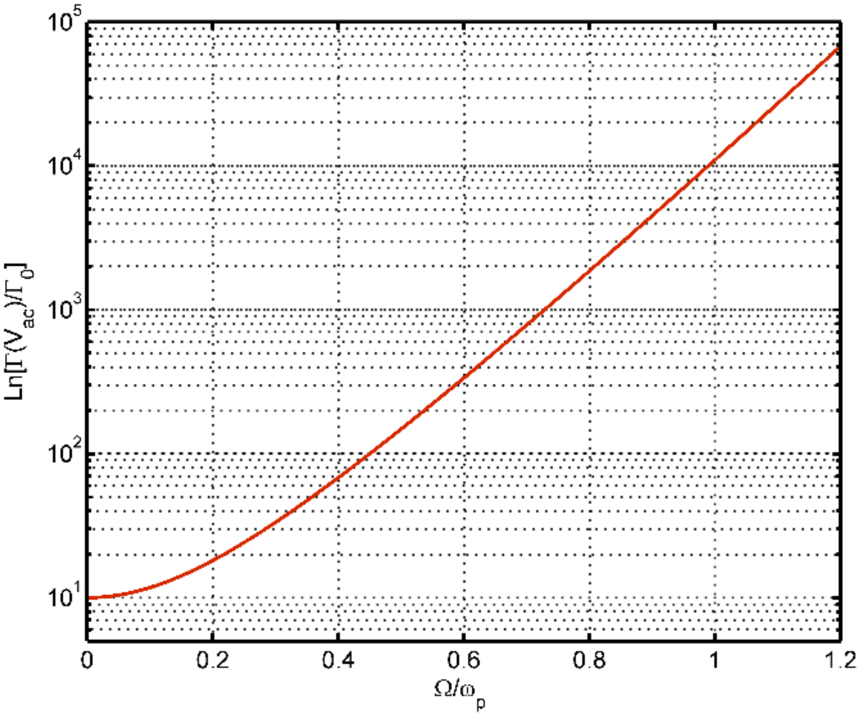

Figure 3.5: Enhancement of the probability of quantum tunnelling as a function of the normalized frequency Ω/ω_p. Parameters used for the simulation are $V_{ac}/V_c = 0.1$, $\eta/\omega_p = 10$ and $4eV_c/\omega_p = 10$.

The most interesting feature of Eq. (3.26) is that the exponential enhancement factor is inversely proportional to the tunnelling factor in the absence of the high-frequency field. Therefore, the exponential enhancement in the presence of the high-frequency field is more noticeable in systems with low tunnelling rate.

In the absence of the V_{dc}, the tilt in the potential barrier disappear and therefore the probability of tunnelling to right and left becomes equal and the average current becomes zero ($\bar{I} = 0$). In the presence of the voltage bias, the average current is given by:

$$\bar{I} = 2e\left(\Gamma_{\rightarrow} - \Gamma_{\leftarrow}\right) \tag{3.27}$$

where $\Gamma_{\rightarrow}$ indicates tunnelling to the right (lower energy) and $\Gamma_{\leftarrow}$ tunnelling to the left (higher energy) of the tilted washboard potential barrier. Since we are mostly interested in the bias voltage close to the critical voltage (V_c), the $\Gamma_{\leftarrow}$ goes to zero; hence, by dropping the index ($\Gamma = \Gamma_{\rightarrow}$), we arrive at

$$I \approx 2e\Gamma(V_{ac}), \tag{3.28}$$

where $\Gamma(V_{ac})$ is given by Eqs. (3.19) and (3.24) for low-dissipation and high-dissipation cases respectively. According to Eq. (3.28), the influence of high-frequency irradiation on the superconducting nanowire can be observed in the current.

The effect of dissipation on the exponential enhancement in Eq.(3.24) is apparent. The bigger is the resistance R the larger is the enhancement. Intuitively, this can be understood from Eq. (3.23), where τ_s reflects the time of the underbarrier motion. The time of the underbarrier motion grows with larger dissipation. The cartoon in Fig. 3.4 shows quantum tunnelling of a particle trapped in a meta-stable potential in the presence and absence of dissipation. Without dissipation, the energy of the particle is unchanged before and after tunnelling; whereas, with dissipation, the particle loses energy to the environment and therefore has to emerge from the barrier with lower energy which results in a longer under barrier motion. According to the semiclassical description of quantum tunnelling in Sec. C.1, during the quantum tunnelling the time parameter becomes imaginary and therefore the alternating potential changes

$$\cos\Omega t \rightarrow \cosh\Omega\tau. \tag{3.29}$$

Therefore, the oscillatory driving potential becomes exponential which is the underlying physics behind the exponetial enhancement in Eqs. (3.19) and (3.24). It can be seen that the longer is the undebarrier motion the bigger this factor becomes.

The observation of the enhancement is more likely to be observed in low-quality QPS junctions, where the quality factor Q_{QPS} is defined as

$$Q_{QPS} = \sqrt{\frac{2\pi}{2e}\frac{L}{R^2}V_c}. \tag{3.30}$$

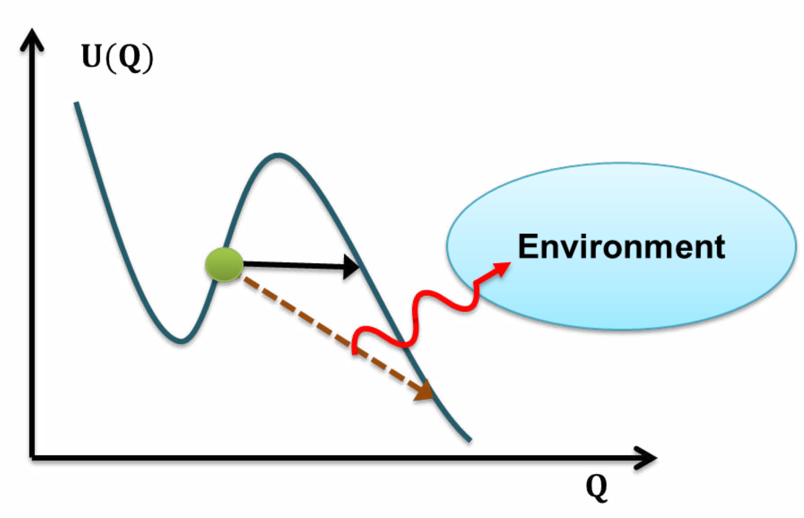

Figure 3.6: Quantum tunnelling of a particle from the metastable potential barrier for two cases of dissipative and non-dissipative tunnelling is shown. The black solid arrow represent tunnelling with no dissipation. The energy of the particle after the tunnelling is the same as the energy of the particle before tunnelling. The dotted arrow indicates tunnelling with dissipation. In this case the particle loses some energy to the environment. The emerging particle has less energy than before tunnelling and has to travel longer underbarrier distance.

Another reason for low-Q QPS junctions to be better candidates in observing tunnelling enhancement is that in low-Q systems, discreteness of the energy levels is suppressed, therefore the semi classical approach is more accurate.

A comment on the range of validity of the method we used in this section is in order. As it is seen from Eq. (3.24), the enhancement in the tunnelling probability for $\Omega\eta \gg \omega_p^2$ is itself an exponentially large factor ($\sim eV_{ac}\Omega^{-1}\exp(\Omega\eta/\omega_p^2)$). This indicates that the range of the validity of the semi-classical approach in this case is limited to $V_{ac} \sim \Omega e^{-1}\exp(-\Omega\eta/\omega_p^2)$. Beyond this, higher order correction in terms of V_{ac} to the action is required [40].

3.5 Concluding Remarks

The effect of a high-frequency field on the zero-current state of a QPS junction was studied. The approach chosen was to use the duality transformation between Josephson junction and a QPS junction to reduce the dynamics of a QPS junction into a circuit model and then study the effect of high-frequency field. The similar problem has been studied for the case of Josephson junction using semiclassical physics [28, 34, 1] which we adopted for the case of QPS junction. We observed that a high frequency field can enhance the probability of the quantum tunnelling exponentially. We obtained the enhancement in two cases of small dissipation and strong dissipation. For small dissipation, the enhancement exhibits resonance effect which is non-physical and need to be smeared out. We observed that the exponential enhancement is more pronounced when the quantum tunnelling in the absence of the high-frequency field is small. In strong dissipation limit the enhancement in the quantum tunnelling rate is more likely to be observed. The enhancement in the quantum tunnelling and its dependence on the frequency can be exploited in designing energy-resolving high-frequency detectors which is the subject of the next chapter.

Chapter 4

Proposal for QPS-based Energy-resolving High-frequency Radiation Detector

The exponential enhancement of the probability of the quantum tunnelling observed in Eqs. (3.19) and (3.24) can be exploited in designing detectors of millimetre and sub-millimetre radiation that are capable of determining the frequency of the incoming energy. In this chapter we introduce a new type of high-frequency detectors based on enhancement of QPS phenomenon in superconducting nanowires.

Of particular interest in high-frequency detection is an energy resolving detector in the THz frequency. The THz radiation spans frequencies from 0.3 THz to 3 THz. This frequency range is situated between microwave and far infrared waves and technologically is the least developed in the electromagnetic field spectrum. There is a great interest in developing THz sources and THz detectors and it is an active and growing field of research. THz technology can be used in many applications, like:

- Medical imaging
- Material characterization
- THz astronomy
- Security
- Communication

Superconductors, both LTS and HTS are widely used in developing THz sources and detectors particularly for applications in astronomy [41].

4.0.1 Superconducting THz Detection Methods

In this section a general overview of different methods used for detection of the THz radiation, particularly in astronomy is given.

In general, two types of superconducting detectors exist for THz detection, i.e., bolometric and pair breaking detectors [41].

Bolometric detectors operate on the basis that the incident energy can significantly change the resistance of a small superconducting island near its phase transition. Transition edge detector (TES) is the most sensitive type of the bolometric detectors. In TES detectors, the superconducting element is biased close to phase transition. This transition is very steep such that a weak incident radiation can results in a significant change in the resistance. For stability reason, the superconductor is voltage-biased and the change in the current is monitored by a superconducting interference device (SQUID).

Pair breaking detectors work on the basis that the absorbed radiation break cooper pairs and therefore the density of quasi-particles is changed. For this to work the energy of the incident photons needs to be larger than the pairing energy of the cooper pairs. Measuring the change in the number of quasiparticles indicates the presence of the radiation. Superconducting tunnel junction (STJ) detectors and kinetic inductance (KI) detectors are two examples of pair breaking detectors.

In STJ detectors, the SNS junction is dc-biased just bellow the energy gap. The absorbed photons in the superconductor break cooper pair and produce quasiparticles. The quasi-particles tunnel across the junction and result in the increase in the junction current proportional to the photon energy.

In KI detectors, the incident photons on a superconducting strip break cooper pairs and create quasiparticles. This leads to a decrease in the density of the cooper pairs and consequently increase in the kinetic inductance of the strip. The superconducting strip is combined with a capacitor to form a resonator with its resonance frequency dependent on the energy of the incident photons. By monitoring the resonance frequency, the presence and energy of the radiation is determined.

4.1 The Physical Principle of the QPS-based THz Detector

The proposed detector is made of a low-Q QPS junction that is voltage biased close to the critical voltage. A THz antenna is the source of the high-frequency voltage and is placed right across the superconducting nanowire. The current in the loop is measured constantly, the change in the current and the amplitude determines the nature of the detected radiation. A schematic of this system is shown in Fig. 4.1.

The antenna shown in Fig. 4.1 is a broadband patch bow-tie antenna [42]. The properties of a bow-tie antenna is determined by the length and the angle of the two metals. Since angle is distance independent, therefore, the bandwidth of a bow-tie antenna is larger than a half-wavelength dipole antenna; nevertheless, the limited length of the bow-tie antenna limits the bandwidth. For a fixed frequency detection, the bow-tie antenna can be replaced with a half wave-length dipole antenna [42]. The radiation pattern of the bow-tie antenna, similar to a dipole antenna, is symmetric toroidal. However, for specific applications like astronomy that the source of the radiation has a fixed location. The simple bow-tie antenna can be replaced with high gain directive antenna that would increase the induced V_{ac}.

The superconducting nanowire is replaced imediately in the gap between two parts of the antenna. This will guarantee that the maximum V_{ac} is induced along the nanowire. Other elements like the resistance and the voltage-bias source are placed outside of the antenna in the loop.

Presence of a THz radiation results in the decay of the zero-current state of the QPS junction which causes a change in the current of the circuit. Depending on the design parameters, the detection of the change in the current might be hard to achieve. A lock-in amplifier or a SQUID can be used for current monitoring in case the current change is difficult to be monitored with conventional methods.

The resistance R plays the important role of reducing quality factor (Q) of the QPS junction. Its value is chosen such that the required enhancement in Eq. (3.24) is achieved, which depends on other parameters of the system.

4.1.1 Design Parameters

In this section, we investigate design parameters for a sample $\Omega/2\pi = 300$ GHz detector. We will look at different superconducting materials to see the applicability of them in our

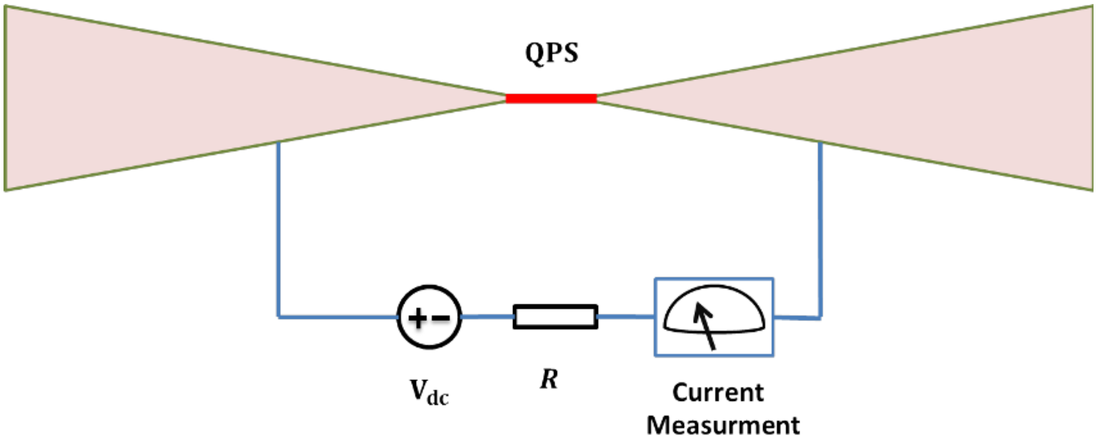

Figure 4.1: The schematic of a QPS high-frequency detector is shown. The red segment in the middle, is the superconducting nanowire. A broadband bow-tie antenna collects the high-frequency field. The resistance R adds dissipation to lower the quality factor of the QPS junction. The QPS junction is biased close to the critical voltage V_{DC}. The system is initially biased in the zero-current state. The current of the loop is constantly monitored. Change in the current is the signature of the radiation and its amplitude determines the frequency. For the center frequency of $\Omega/2\pi = 300$ GHz, the length of the antenna is $\sim \lambda/2 = 500\mu m$. The length of the superconducting nano wire is arbitrarily chosen $\approx 2\mu m$. The figure is not drawn to scale.

design and based on the properties we will chose the rest of the set-up.

As before, we assume that The QPS energy is related to the QPS rate according to Eq. (D.6). The QPS rate from the GZ theory is given by

$$\Gamma_{QPS} = c_1 \frac{\Delta}{\hbar} \frac{R_q}{R_n} \frac{X^2}{\xi^2} \exp\left(-0.3 c_2 \frac{R_q}{R_n} \frac{X}{\xi}\right), \tag{4.1}$$

where R_n is the normal resistance per 1 nm of the superconducting nanowires. The two constants c_1 and c_2 account for uncertainties in derivation of Eq. (4.1) which are of order one. We set $c_1 = c_2 = 1$. Although Eq. (4.1) is given by GZ theory, the factor 0.3 in the exponent is adopted from the fit of experimental data to the Giordano model in the work of [43, 19].

In order to choose the appropriate material and parameters for the detector, we study properties of four different materials NbSi, InO$_x$, NbN and Ti. Properties of these materials are listed in Table 4.1. The coherence length ξ for superconducting nanowire is related to the bulk parameter through

$$\xi \sim 0.85\sqrt{\xi_{\text{bulk}} l_0} \tag{4.2}$$

where, l_0 is the mean free path of the electrons. 1D superconducting nanowires are always in the dirty limit.

Table 4.1: Material properties of the superconducting nanowires used for simulations.

Material	Δ [meV]	ξ [nm]
NbSi	0.18	15
InO$_x$	0.41	20
NbN	1.6	4
Ti	0.06	80

The data for NbSi, InO$_x$, NbN and Ti are adopted from [44], [20], [45] and [46] respectively.

Fig.4.2 shows E_{QPS} for four different materials as a function of normal resistance per length. The resistance per length R_n determines the cross-section area of the superconducting nanowire. Since R_n is inversely proportional to the cross-section area of wire, higher R_n requires thinner nanowires which makes the operation more difficult. Thinner superconducting nanowires support smaller currents which makes it more difficult to detect.

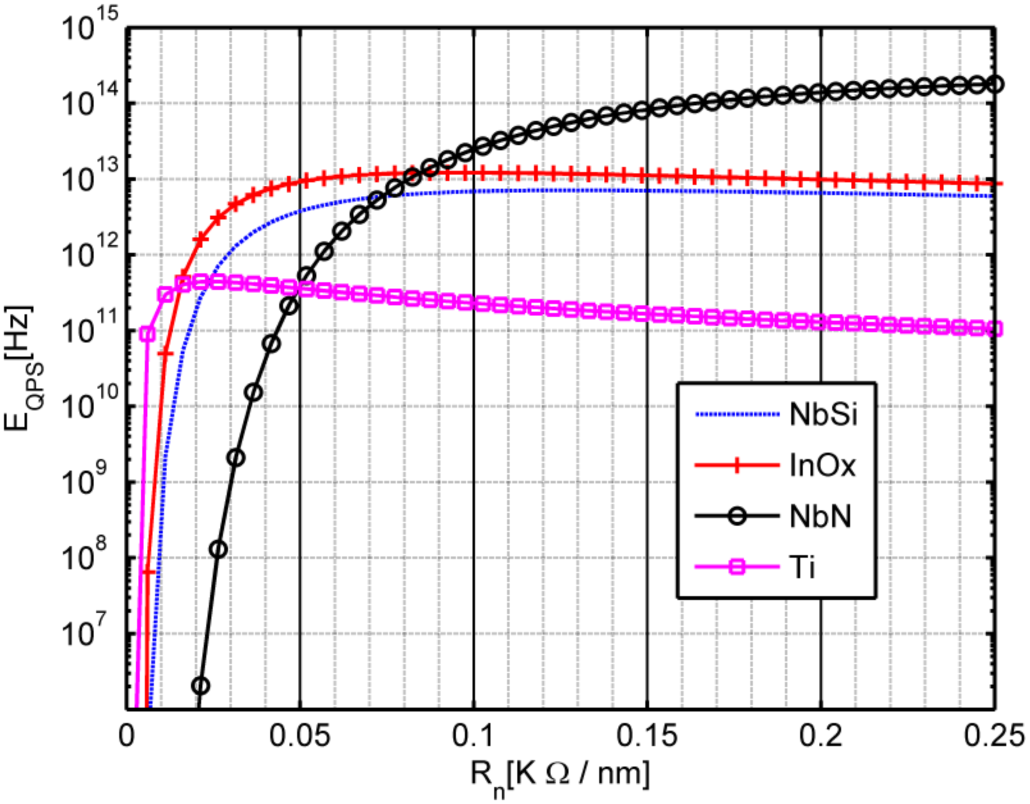

Figure 4.2: The QPS energy as a function of the normal resistance per length for four different materials NbSi, InO_x, NbN and Ti is shown. The R_n determines the dimensions of the superconducting nano wire. Parameters are listed in Table 4.1.

Another important energy scale in QPS junctions is the kinetic inductive energy E_L which plays an important role in the dynamics (see Appendix D). The kinetic inductive energy is given by

$$E_L = \frac{\Phi_0^2}{2L_k}, \tag{4.3}$$

where the kinetic inductance is found from

$$L_k = \frac{\hbar R_N}{\pi \Delta}. \tag{4.4}$$

In Eq. (4.4), R_N is the total normal state resistance of the superconducting nanowire which is given by $R_N = XR_n$, where X is the length of the superconducting nanowire. In Eq. (4.3), the geometric inductance and external inductance are assumed to be much smaller than the kinematic inductance L_k of the superconducting nanowire.

In Fig. 4.3 and Fig. 4.4 the inductive kinetic E_L energy and the plasma frequncy ω_p of the four nanowire as a function of normal resistance per length are shown. The plasma frequency ω_p is given in Eq. (3.7).

Since the superconducting nanowire is intended to be working in the regime where charge is a good quantum number; this requires that at least $E_{QPS} > 4E_L$. The ratio of E_{QPS}/E_L is shown in Fig. 4.5. The acceptable region of parameters is anywhere above 4.

Now we restrict ourself to a specific frequency of $\Omega/2\pi = 0.3$ THz. We choose the length of the superconducting nanowire to be $X = 2\mu$m. To satisfy the conditions of the semiclassical approach of the previous chapter, we choose $E_{QPS} = 1.5$ THz. This leads to the critical voltage of

$$V_c = \frac{2\pi}{2e} E_{QPS} = 1.5 \times 10^{12} \hbar (2\pi)^2 / 2e = 19\text{mV}. \tag{4.5}$$

Assuming the induced alternating voltage collected by the antenna has the amplitude of $V_{ac} = 100$ nV, then $4eV_{ac}/\hbar\Omega \sim 10^{-3}$. Therefore, from Eq. (3.26), to have a significant enhancement it is necessary to have

$$\frac{\Omega \eta}{\omega_p^2} \gg \sinh^{-1}(10^3) \approx 8, \tag{4.6}$$

where the dissipation η with dimension radian per second is defined in Eq. (3.6). If we choose NbSi as the candidate material for the detector, from Figs. 4.2, 4.3, 4.4 and 4.5 we

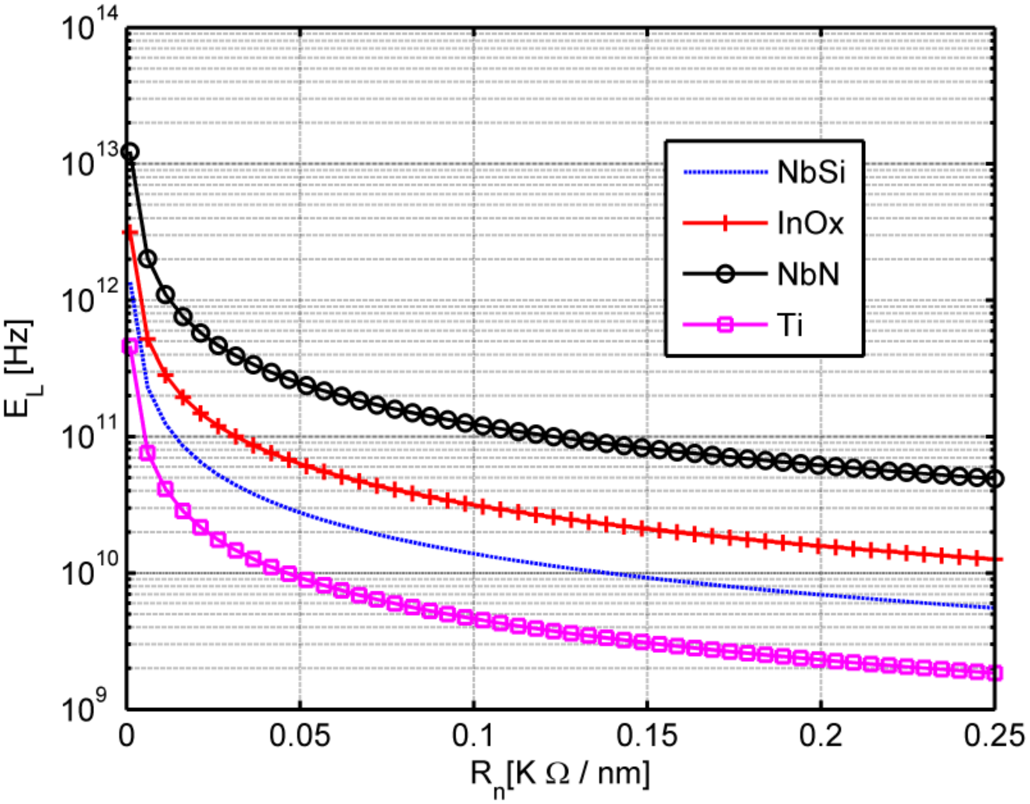

Figure 4.3: The inductive kinetic energy as a function of the normal resistance per length for four different materials NbSi, InO$_x$, NbN and Ti is shown. The R_n determines the dimensions of the superconducting nano wire. Parameters are listed in Table 4.1.

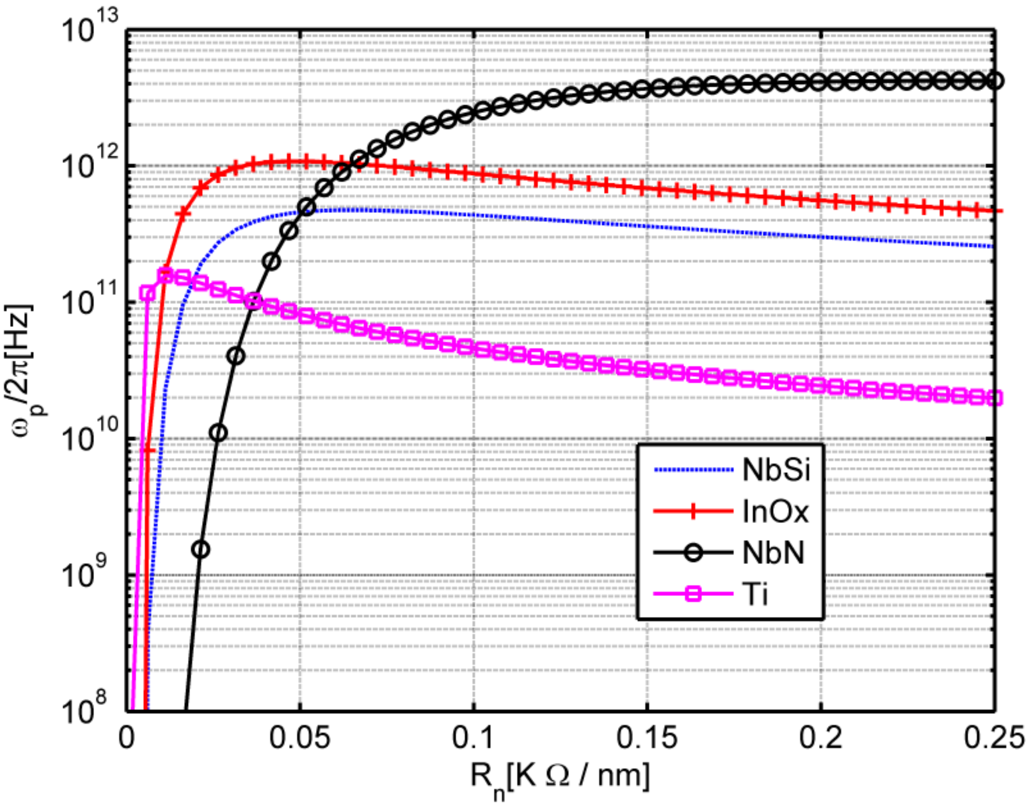

Figure 4.4: The plasma frequency $\omega_p/2\pi$ as a function of the normal resistance per length for four different materials NbSi, InO_x, NbN and Ti is shown. The R_n determines the dimensions of the superconducting nano wire. Parameters are listed in Table 4.1.

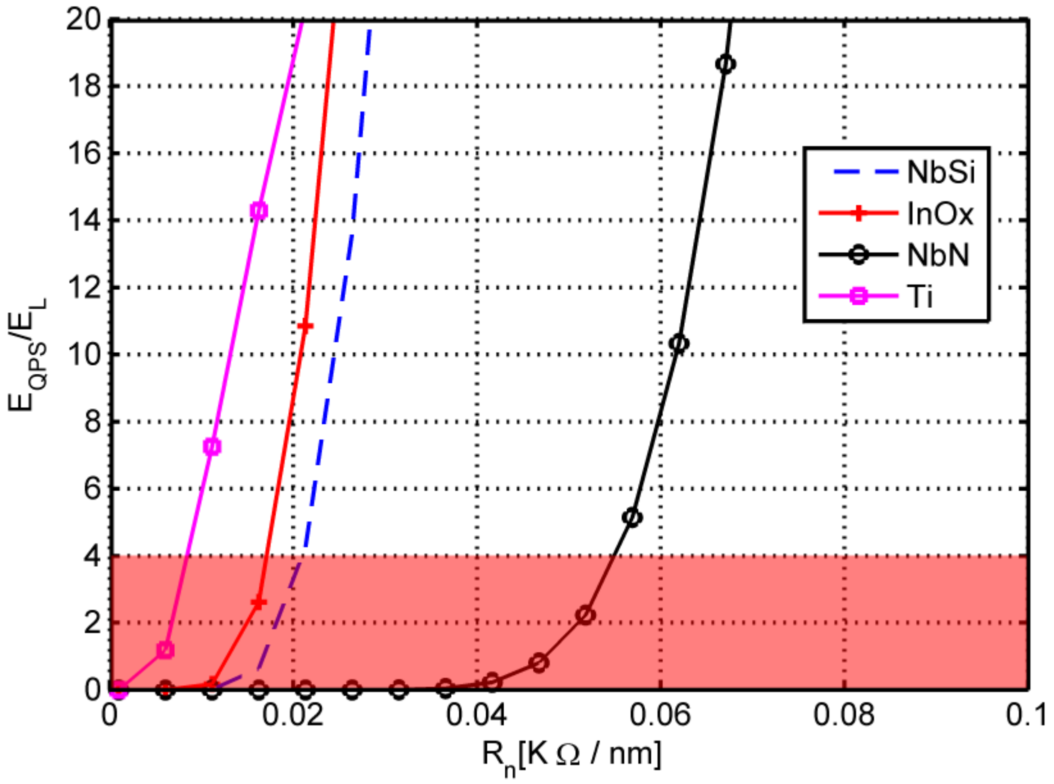

Figure 4.5: The ratio of E_{QPS}/E_L as a function of the normal resistance per length for four different materials is shown. For the charge number to be the good quantum number, it is required that $E_{QPS} > 4E_L$. The unwanted region of parameters is highlighted with red.

obtain the following parameters:

$$\begin{aligned} X &= 2 \quad \mu\text{m}, \\ R_n &\approx 0.3 \quad \text{K Ohm/nm}, \\ E_{QPS} &\approx 1.4 \quad \text{THz}, \\ E_L &\approx 40 \quad \text{GHz}, \\ \frac{E_{QPS}}{E_L} &\approx 35, \\ \frac{\omega_p}{2\pi} &\approx 0.3 \quad \text{THz}, \\ L_k &\approx 75 \quad \text{nH}. \end{aligned} \tag{4.7}$$

Using parameters obtained in Eq. (4.7) in Eq. (4.6), in order to have enhancement the value of the external resistance R needs to be roughly

$$R > 180 \text{ K Ohm}. \tag{4.8}$$

For an on chip resistance, NiCr thin-film resistors can be used.

4.2 Discussions

One of the significant advantages of the proposed detector is the simplicity of the fabrication using electron-beam lithography. The superconducting nanowire and the antenna can be fabricated lithographically on the same substrate. Avoiding shunting parasitic capacitances might be challenging that requires extra attention.

In the proposed structure of Fig. 4.1, the electric field is in the plane directed from one side of the antenna to the other. This is the desired polarisation for a superconducting nanowire detector.

The width of the QPS element is in the order of 10 nm to 20 nm, therefore, a large number of them can be fabricated in parallel which makes them good candidates for applications that require many elements like imaging or for higher detection and coupling efficiency.

In the proposed method the detector is made of quasi 1D nanowires ($r < \xi$), therefore the presence of vortices can be ignored. This is because structures smaller than 4.4ξ can not support vortices. The absence of vortices might improve the noise performance of detectors.

Another advantage is that, the operating temperature of the proposed structure is bellow T_0 which is the cross over between quantum tunnelling and thermal activation. Therefore, thermal noise is greatly suppressed.

4.3 Concluding Remarks

In this chapter we outlined a new type of high-frequency detectors based on the QPS phenomenon in superconducting nanowires. A basic set-up for such a detector was introduced. We then investigated the possibility of such realization in the materials used in studying of QPS in superconducting nano wires. It was shown that the theoretical restrictions can be met by choosing correct design parameters. We stress that the proposed design is based on the theoretical work presented in Chapter 3 which involved many approximations. A more accurate theoretical work might be needed for a more accurate design.

Part II

2D Superconducting Nanostrips

Chapter 5

Multi-layer SNSPD

5.1 Introduction

The inherent limitation in the performance of superconducting nanowire single-phton detectors (SNSPDs) is the low optical coupling efficiency from a free space source [5]. The nature of the photon detection mechanism demands superconducting thin films of thicknesses of about 4nm to 7nm. The superconducting layer, which is much smaller than the wavelength of the electromagnetic wave, is semi-transparent to incident photons. Increasing the thickness of the film improves the absorption rate; however, it adversely reduces the efficiency of triggering photon detection events. The use of microcavity [2] or surface plasmonic structures [47] have been proposed to improve the coupling efficiency; however, they all suffer from the limited bandwidth and also not being suitable for free space operation. Employing new families of superconducting materials, like amorphous tungsten silicide (WSi) [48], has also been investigated to address the absorption problem. A remarkable system quantum efficiency of 93% has been reported for WSi system; however, very low operating temperature of 120 mK, slow reset time, and weak jitter performance are among the drawbacks of this system.

A multi-layer structure, shown in Fig. 5.1, is capable of improving the performance of SNSPDs in both the quantum efficiency, and dark count. A multi-layer structure increases the photon absorption probability in the system by increasing the effective thickness of the absorptive layer. Nevertheless, a multi-layer structure is designed such that adjacent layers are Josephson decoupled (the inter-layer Josephson current is negligible). Therefore, the efficiency of the triggering mechanism at these parallel layers is not affected.

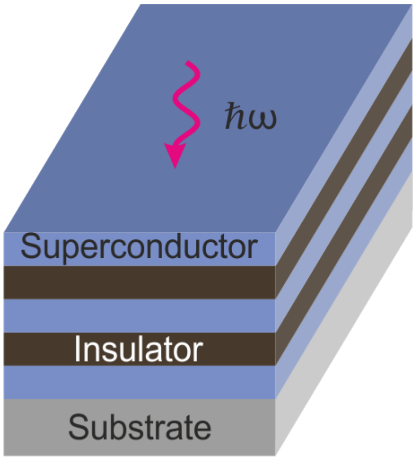

Figure 5.1: The schematic cross section of a N=3 SNSPD is shown. Each superconducting layer is separated by an insulating layer such that the Josephson current between the layers is negligible. All superconducting layers are independently biased.

The single-photon sensitivity of SNSPDs is highly bias current dependent. The higher bias current provides a higher photon detection rate, but the structure becomes more prone to dark counts. The maximum experimental critical current ($I_{\mathrm{c,e}}$) that can be achieved in superconducting nanowires is much smaller than the critical repairing current that theory predicts [27, 49]. This is due to the proliferation of fluctuations at high bias current that destroys superconductivity in ultra-thin samples. The performance of a typical SNSPD is shown in Fig. 5.2. In Fig. 5.2, the count rate in the logarithmic scale is shown versus the bias current. The maximum achievable count rate is bounded by the dark count curve. At $I_b = I_{\mathrm{c,e}}$, the SNSPD enterers the latching mode and it stops counting[5].

In superconducting nanowires with widths capable of supporting vortices ($w > 4.4\xi$), which are typically used in SNSPDs, fluctuations are primarily originated from the vortex crossings [26, 27]. From the discussions of the first part of this thesis on phase slips we learned that when $w \gg \xi$ the potential barrier for phase slippage becomes so large that the probability becomes negligible. In nanowires of $w \geq 4.4\xi$, vortices cause dissipative fluctuations in two distinct mechanisms. The dominant mechanism is the crossing of the vortices generated at the edges of the nanowire by the bias current [26, 27]. The motion of the vortices from the edge into the nanowire can cause a normal-state belt across the strip. The normal belt manifests itself in a voltage spike that results in a dark count. Another mechanism of fluctuation is the spontaneous formation of vortex-antivortex pairs (VAPs) and their motion toward edges in opposite directions[26, 27]. This phenomenon, also known

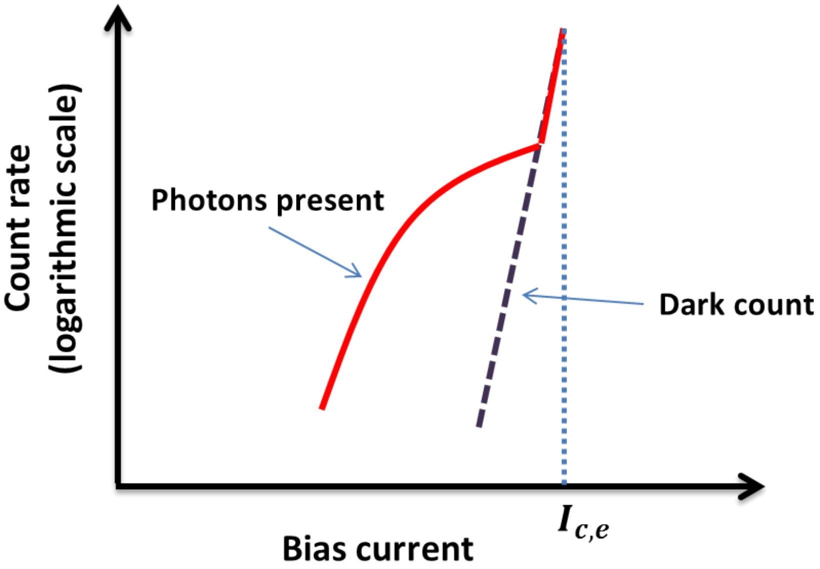

Figure 5.2: A typical count rate versus the bias current in a SNSPD. The count rate is shown in the logarithmic scale. The dashed straight line to the right represents the dark count rate when no photon is present. The photon count curve follows the dark count curve after the intersection. The operating bias current of a SNSPD is chosen such that the maximum photon count rate is achieved with minimum dark counts. At $I_b = I_{\mathrm{c,e}}$, the SNSPD enters the latching mode and it can no longer count photons [5].

as VAP unbinding, can also cause a normal belt across the strip and results in a dark count. Nucleation of VAPs does not depend on the bias current; however, the VAP unbinding is dependent on the bias current (see the paper by A. J. Leggett in [50]). It will be shown that the potential barrier for VAPs unbinding in most cases is bigger than the potential barrier for vortex crossing; therefore, vortex crossing is mostly the dominant process in dark count. It is desirable to increase the maximum current that a superconducting nanowire can support and at the same time decrease the dark count. Curiously, the reduction of fluctuations addresses both issues simultaneously.

A multi-layer structure decreases fluctuations due to thermally activated vortex crossing by effectively increasing the energy barrier. The underlying physics is that the electromagnetic field variation of vortices occurs on scale of the London penetration depth, λ, (λ of NbN is $\approx$ 400nm). In a multi-layer superconducting system with spacing smaller than the London penetration depth, the electromagnetic behaviour of a vortex is affected by other layers as well; therefore, a vortex experiences (a pancake vortex in a multi-layer system, see section 5.2) a bigger potential barrier in the crossing. Vortices encounter an effectively thicker superconductor, and therefore, a higher potential barrier. This leads to a significantly lower rate for vortex crossing which consequently results in higher experimental critical current as well as lower dark count rate.

In this chapter the SI system which is more suitable for engineering applications is adopted; whereas, in previous chapters the CGS system which is more convenient for theoretical works were used.

In the following, we will first review the physics of 2D pancake vortices. Then we will calculate the potential barrier for vortex crossing in a multi-layer SNSPD. The potential barrier enables us to calculate the rate of vortex crossing for different number of layers. The optical properties of a multi-layer structure is then studied and the optical absorption for different number of layers is calculated. We also comment on the electrical isolation of different layers. In Appendix E, the physics of vortices in thin films which is the basis of 2D pancake vortices is reviewed in details. In Appendix F, the transfer-matrix method which is used in this chapter is reviewed.

5.2 Pancake Vortices in a Superconducting Multi-layer System

In an N-layered thin superconductor, a 3D-vortex is made of N 2D-vortices, known as pancake vortices, that each resides in a separate layer (see Fig. 5.3). Each pancake

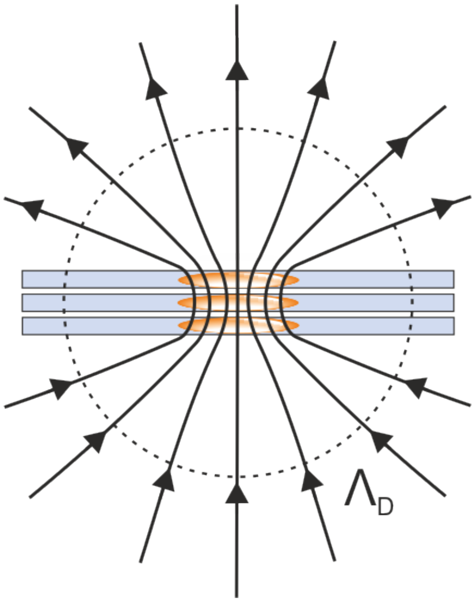

Figure 5.3: A schematic full vortex in an N=3 layer system made of 3 pancake vortices is shown. The magnetic field produced by pancake vortices varies on scale of $\lambda_\parallel$ (not shown). The figure is not drawn to scale ($\Lambda_D \gg D$).

vortex traps a fraction of the total quantum flux. This reduction in the flux is due to the modification of the transverse screening current by other layers. In this section, we review the physics of pancake vortices relevant to our further analysis (see [51, 52]).

In an N-layered system shown in Fig. 5.4 the thickness of a single superconducting layer is d and the length of a period is s, so that the total thickness of the system is $D = Ns$. The London penetration of the superconducting material is λ and the average penetration depth for current parallel to the layers is $\lambda_\parallel = (s/d)^{1/2}\lambda$ [53]. In an analogy to the Pearl vortex model [54], the characteristic screening length is defined as $\Lambda_D = 2\lambda_\parallel^2/D$ (see Appendix E). Assuming a single pancake vortex is residing at the center of layer i, the magnetic potential and the screening current can be calculated at other layers using the London's equation

$$2\pi r \left[A_\phi(r, z_j) + \frac{\mu_0 N \Lambda_D}{2} K_\phi(r, z_j) \right] = \phi_0 \delta_{ji}. \tag{5.1}$$

In the limit of $r \ll \Lambda_D$, which is relevant for SNSPDs, and assuming $D \ll \lambda_\parallel$, the induced sheet current density in layer j due to a single pancake vortex located in layer i is given by [51, 55]

$$K_\phi(r, z_j) = \begin{cases} \frac{\phi_0}{2\pi\mu_0 N \Lambda_D r}, & j = i, \\ -\frac{\phi_0 \lambda_\parallel}{2\pi\mu_0 N^2 \Lambda_D^2 r} \times & \\ \quad \left[\exp\left(-\frac{|z_j|}{\lambda_\parallel}\right) - \exp\left(-\frac{\rho_j}{\lambda_\parallel}\right)\right], & j \neq i. \end{cases} \tag{5.2}$$

Here, r and z_j are the cylindrical coordinates from the location of the pancake vortex and $\rho_j = (z_j^2 + r^2)^{1/2}$. According to Eq. (5.2), the circulating screening current at layer $n \neq i$ is opposite in direction to the screening current at the layer $n = i$; this leads to an attractive force between two pancake vortices residing at two different layers; whereas, it is attractive for two pancake vortices in the same layer. It is seen from Eq. (5.2) that the induced current density at the layer $n \neq i$ is by a factor of about $N\Lambda_D/r$ smaller than the current in the layer $n = i$ for $r \ll \Lambda_D$ and can be ignored. The current density in this limit resembles that of a Pearl vortex in a single layer film [54].

The radial force between two pancake vortices is calculated from $F_r(r) = K_\phi(r)\phi_0$ where K_ϕ is the current density of a pancake vortex at the location of the second one. The potential energy between two pancake vortices of opposite charge (anti-pancake vortex) in the same layer follows from the integration of the force as follows:

$$U = \frac{E_N}{N} \ln\left(\frac{r}{\xi}\right). \tag{5.3}$$

Here, $E_N = \phi_0^2/2\pi\mu_0\Lambda_D$, where ξ is the coherence length of the system that sets the cut-off in the energy integration. The potential energy in Eq. (5.3) reflects only of a pancake vortex, not a full 3D-vortex; however, when $D \ll \lambda_\parallel$, the potential energy between a 3D-vortex and 3D-anti-vortex in a layered structure is calculated knowing that an equal amount of magnetic flux passes through all layers; therefore, in this limit, the total potential energy is N times larger than Eq. (5.3). This is understood from the physics of Pearl vortices of a single thin layer where the field variation occurs on scale of $\lambda_\parallel$ [54].

5.3 Potential Barrier for Vortex Crossing

In this section we calculate the potential barrier for vortex crossing across the width of the superconducting strip in a multi-layer setting. Two factors contribute to the potential barrier: the self energy of interaction with edges and the Lorentz force due to the bias current. In a semi-infinite 2D-plane, the self energy resists the penetration of the vortex into the superconductors. This is modified in a strip when two edges interact with the

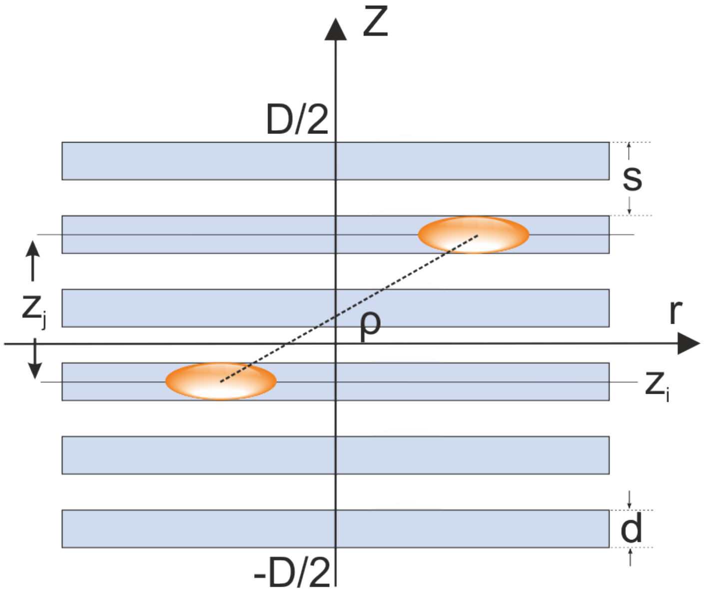

Figure 5.4: Two pancake vortices residing at two different layers are shown. z_j is the verical distance and r is the horizontal distance between the two vortices. Two vortices attract each other.

vortex. The effect of the Lorentz force due to the bias current is always to pull the vortex into the superconductor.

The effect of the film's edge on a vortex at distance δ can be modelled by placing an anti-vortex image at distance 2δ [56]; hence, Eq. (5.3) is applicable in describing the edge effect. Similarly, the effects of both edges can be modelled as an infinite series of alternating positive and negative image charges located at

$$v_n^+ = \delta + 2wn \quad \text{and} \quad v_n^- = 2wn - \delta, \quad n \in \mathbb{Z} \tag{5.4}$$

where w is the film width. Fig. 5.5 shows the position of the images vortices. The total potential energy for a test vortex at position x from the infinite vortex configuration is given by:

$$U = \frac{E_N}{N} \sum_{n=-\infty}^{+\infty} \ln\left(\frac{x + \delta - 2wn}{\xi}\right) - \frac{E_N}{N} \sum_{n=-\infty}^{+\infty} \ln\left(\frac{x - \delta - 2wn}{\xi}\right). \tag{5.5}$$

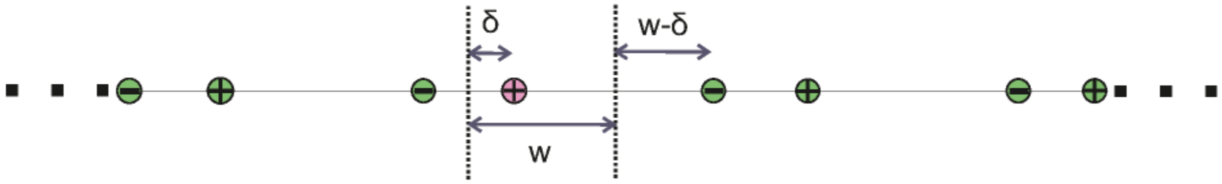

Figure 5.5: Image vortices for a superconduting nanostrip are shown. The superconducting strip is indicated by two parallel dotted line. The two edges of the superconducting strip is replaced by an inifite series of vortices of alternating charges according to Eq. (5.4).

After some algebra, Eq. (5.5) simplifies to[1]

$$U = \frac{E_N}{N} \ln \left(\frac{\sin \frac{(x+\delta)\pi}{2w}}{\sin \frac{(x-\delta)\pi}{2w}} \right). \tag{5.7}$$

The self energy of the interaction of a vortex with edges can be obtained from Eq. (5.7) by $x \to \delta$; however, This limit leads to an infinity. By introducing the cut-off ξ, the self energy of 3D vortex in an N-layered superconducting strip is given by

$$U_{S,N} = E_N \ln \left(\frac{2w}{\pi\xi} \sin \left(\frac{\pi\delta}{w} \right) \right), \tag{5.8}$$

which is N times larger than a single pancake vortex in an N-Layered spercondcuting strip. $U_{S,N=1}$ coincides with the self energy of a vortex in an isolated strip as given in [57].

Another contribution to the potential barrier comes from the Lorentz force of the bias current in displacing the vortex away from the edge. Assuming the bias current of each layer is I_b, the Lorentz energy due to N bias current acting on the 3D-vortex is

$$U_{L,N} = -N\phi_0 I_b \delta / w. \tag{5.9}$$

---

[1] In simplifying Eq. (5.5) the following identity was used:

$$\sin(y) = y \prod_{n=1}^{\infty} \left(1 - \frac{y^2}{\pi^2 n^2} \right). \tag{5.6}$$

The potential barrier for vortex crossing including the self energy of the interaction with the edges and the Lorentz action of the bias current is given by

$$U_N = E_N \left[\ln \left(\frac{2w}{\pi\xi} \sin \left(\frac{\pi\delta}{w} \right) \right) - \frac{N\pi}{w} \frac{I_b}{I_B} \delta \right], \tag{5.10}$$

where $I_B = \phi_0 / 2\mu_0 \Lambda_D$. Eq. (5.10) for different value of N is shown in Fig. 5.6. In Fig. 5.6, $I_b \approx I_{c,e}$ where the experimental critical current $I_{c,e}$ is chosen roughly 1/4 of the theoretical critical current I_c given by [57]

$$I_c \approx \frac{2w}{\pi e \xi} I_B. \tag{5.11}$$

where $e \approx 2.718$. Eq. (5.10) for different value of I_b is shown in Fig. 5.7 where $I_{c,e}$ is chosen 1/4 of the theoretical critical current given by Eq. (5.11).

The maximum of the energy barrier occurs at distance of $\delta_m = (w/\pi) \tan^{-1}(I_B / N I_b)$ and is equal to

$$\begin{aligned} U_{N,m} = & E_N \left[-\frac{1}{2} \ln \left(\frac{\xi^2 \pi^2}{4w^2} + \frac{N^2 \pi^2 \xi^2 I_b^2}{4w^2 I_B^2} \right) \right. \\ & \left. - \frac{N I_b}{I_B} \tan^{-1} \left(\frac{I_B}{N I_b} \right) \right]. \end{aligned} \tag{5.12}$$

From the Eq. (5.10) the rate of thermal activation for vortex crossing follows [27]

$$R_{V,N} = \alpha_V N I_b \exp \left[-U_{N,m} / k_B T \right], \tag{5.13}$$

where k_B is the Boltzman constant, T is the temperature and the prefactor α_V depends on the attempt frequency and the geometry. The coefficient $N I_b$ in Eq. (5.13) indicates that the vortices formed at the edges of superconducting nanowires are self-generated by the bias current. The exponent is the dominant factor in Eq. (5.13); therefore, we can ignore the variations and uncertainties in α_V. Substituting Eq. (5.12) in Eq. (5.13) and using $U_{N,m} = N U_{1,m}$, we obtain

$$R_{V,N} = R_{V,1} N \exp \left[-(N-1) U_{1,m} / k_B T \right], \tag{5.14}$$

where $U_{1,m}$ is the potential barrier for a single layer. Eq. (5.14) shows that the rate of thermally activated vortex crossing drops dramatically by adding more layers. In Fig. 5.8, the normalized dark count rate from Eq. (5.14) for up to three layers is shown. This sharp

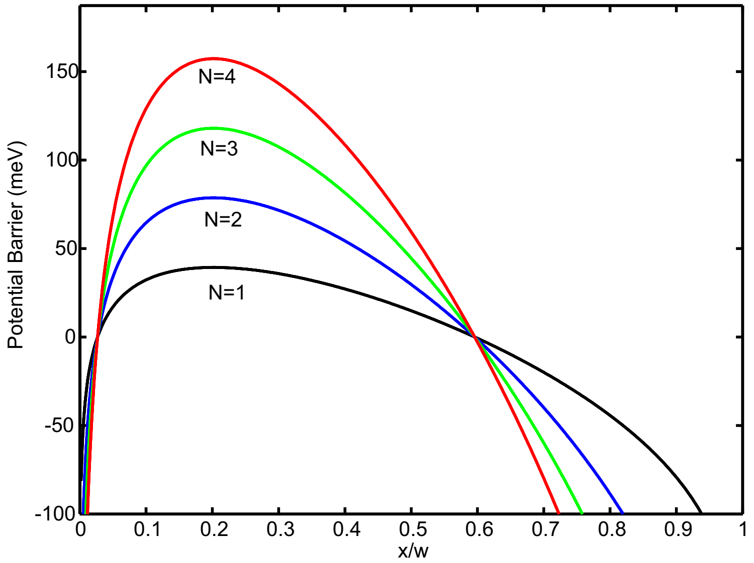

Figure 5.6: The potential barrier for vortex crossing according to Eq. (5.10) for different number of layers. Here, $I_b = I_{c,e}$ where $I_{c,e}$ is the experimental critical current which is arbitrarily chosen about 1/4 of the theoretical critical current given by Eq. (5.11) [57, 27]. The itersection points correspond to the zeros of the potential barrier that occurs at identical distances from the edge of the strip for all N.

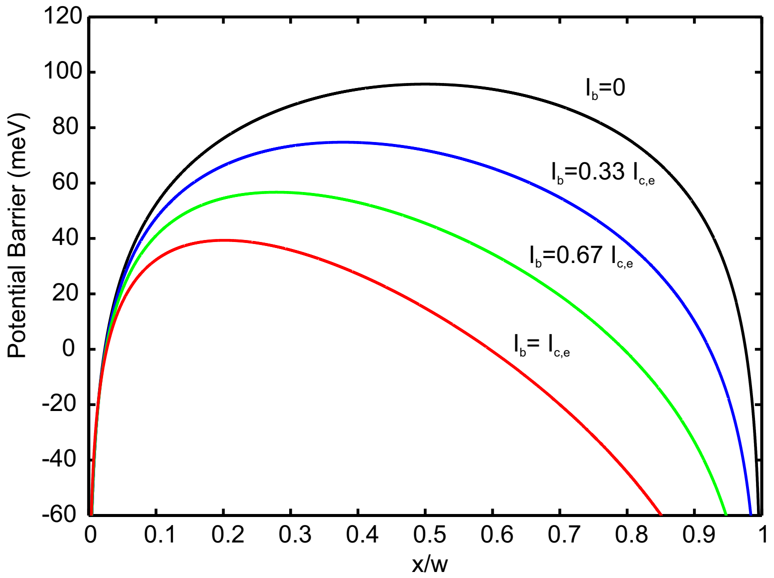

Figure 5.7: The potential barrier for vortex crossing according to Eq. (5.10) for different bias currents. The number of layer $N = 1$. For higher N, like Fig. 5.6, the height of the curves would be multiplied by N. Here $I_{c,e}$ is the experimental critical current which is arbitrarily chosen about 1/4 of the theoretical critical current given by Eq. (5.11) [57, 27].

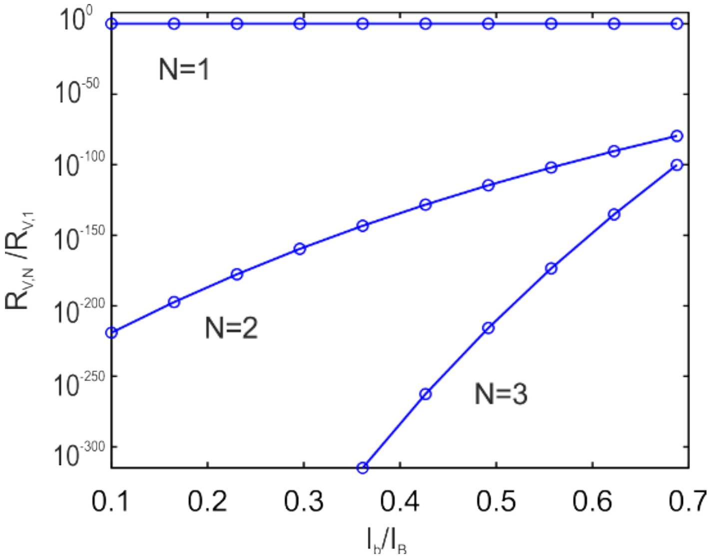

Figure 5.8: The normalized vortex crossing rate vs. normalized bias current for a N-layered SNSPD calculated using Eq.(5.14). By doubling the number of layers, the vortex crossing rate drops dramatically when the bias current is close to the experimental critical current. Parameters used are: d = 5nm, s = 12nm, ξ = 4.2nm, λ = 400nm, T = 4.2K, and w = 50nm.

decline in the dark count rate has significant consequences: (1) With reduction in the rate of the vortex crossing, the experimental critical current approaches the theoretical critical current. Typically, the experimental critical current is by a factor of about two smaller than the theoretical critical current [26, 27]. (2) As a consequence of the increase in the critical current, the SNSPD becomes sensitive to lower energy photons and therefore the bandwidth is expanded. This is easily understood in the hot spot model of photon detection in SNSPDs [5]. Lower energy photons result in a smaller hot region in the SNSPD which can not cause a normal belt across the wire; however, higher bias current can compensate for that and still forms a normal belt and trigger a detection. (3) Dark counts in SNSPDs which are mostly due to thermally activated vortex crossing are significantly suppressed.

5.4 Electrical isolation of superconducting layers

The thickness of the insulating layers has opposite effects on the electric and magnetic properties of the system; therefore, there is a trade-off involved in determining the thick-

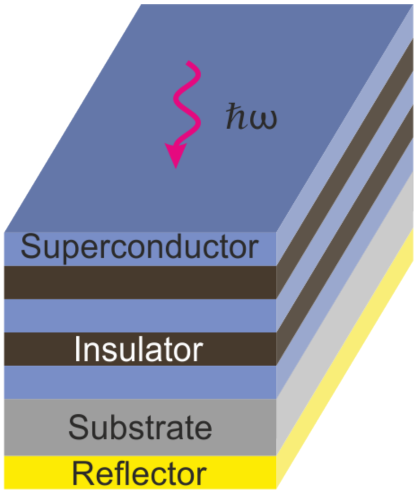

Figure 5.9: The schematic cross section of a N=3 SNSPD with a reflector is shown. A properly designed reflector under the substrate helps in improving the absorption rate by reflecting the transmitted power back into the layers for the second chance of absorption [2].

ness. To make sure that each layer works as an independent SNSPD, the tunnelling current between layers need to be much smaller than the bias current, i. e., $I_{Jc} \ll I_B$, where I_{Jc} is the maximum Josephson current between two superconducting layers separated by an insulating layer. The maximum Josephson current at any temperature can be obtained from the Ambegaokar-Baratoff theory [58] according to

$$I_{Jc} = \frac{\pi \Delta(T)}{2eR_0} \tanh\left(\frac{\Delta(T)}{2k_B T}\right), \tag{5.15}$$

where $\Delta(T)$ is the energy gap, and R_0 is the normal state resistance of the junction. From Eq. (5.15), it is seen that thick insulating layers with high R_0 is better for electrical insulation; however, to keep the pancake vortices magnetically coupled the thickness needs to be kept minimal provided that the condition $I_{Jc} \ll I_B$ is met.

5.5 Photon absorption

The structure of a multi-layer SNSPD is shown in Fig. 5.1. By using the transfer-matrix method [59] we calculate the absorption (A), transmission (T) and reflection (R) coefficients of an incident optical beam. The method of the transfer matrix method is explained in details in Appendix F. In simulations, the angle of the incident photons in Eq. (F.10) is considered normal to the SNSPD.

The simulations for different number of superconducting layers separated by two different insulating materials for two different spacings are shown in Fig. 5.10. The plot shows the ratio of the power absorption to the total power that enters the SNSPD from free space. An anti-reflection coating on top of the structure can minimize the amount of the power being reflected [2]. A properly designed reflector under the substrate, as shown in Fig. 5.9 also helps in improving the absorption rate by reflecting the transmitted power back into the layers for the second chance of absorption [2]. In the simulation the effect of a reflector is not considered. A reflector would shift up the curves in Fig. 5.10 considerably. From Fig. 5.10, it can be seen that adding a second layer to the SNSPD improves the power absorption by about 40% compared to a single layer.

Simulations show that the power absorption is not very sensitive to the thickness and the material of the insulating layer. Nevertheless, the effect of the thickness of the insulating material becomes more noticeable as N increases. The absorption ratio would change considerably for different substrate materials. Substrates with higher (lower) refractive index would shift down (up) the lines in Fig. 5.10.

5.6 Concluding Remarks

It was shown that multi-layer SNSPDs are capable of achieving characteristics of an ideal SNSPD in terms of quantum efficiency, dark count rate and bandwidth. More layers provide higher probability of the photon absorption. Moreover, a multi-layer structure imposes a higher potential barrier for thermally activated vortices to cross the width of the SNSPDs. This has two significant consequences: (1) The experimental critical current approaches the theoretical value. In a single layer device, the experimental critical current is significantly smaller than the theoretical value due to the proliferation of the vortex crossings that drives the superconductor into normal phase at high bias current. Achieving a higher bias current results in a higher quantum efficiency and in a more sensitive device to lower energy photons. (2) By reducing the rate of thermally activated vortex crossing which is the dominant source of fluctuations, the dark count performance of the proposed structure is greatly improved.

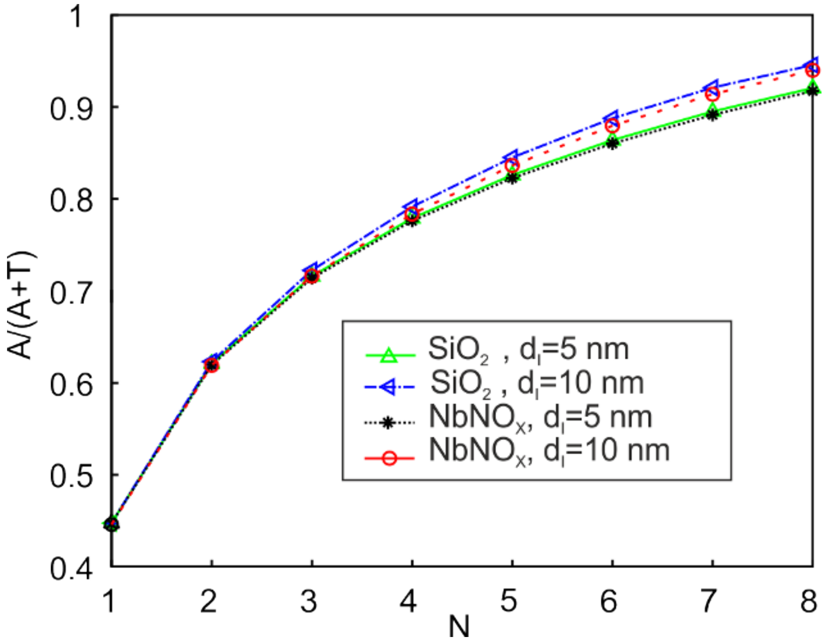

Figure 5.10: The simulation of the ratio of the power absorption (A) to the total power entering a multi-layer SNSPD ($A + T$) for different number of layers at 1550nm is shown. The materials of the 5nm superconducting layers and the substrate are chosen NbN and SiO_2, respectively. Simulations were carried out for two different insulating layers (SiO_2 and $NbNO_x$) at two different thicknesses (5nm and 10nm). The refractive indices of NbN, SiO_2 and $NbNO_x$ are respectively 5.23+i5.82, 1.54 and 2.28 [60].

Chapter 6

Conclusions and Outlook

6.1 Contributions

In this thesis, I studied the properties of superconducting nanostructures for quantum detection of electromagnetic radiation. For this, I investigated the electrodynamics of topological excitations in superconducting nanostructures, i.e. quantum phase slips in 1D-nanowires and vortices in 2D-nanostrips. My main objective was to develop novel nanodevice or improve the performance of the existing quantum nanodevices. My contributions in this thesis can be categorized into two major categories:

1D-Superconducting Nanowires

In 1D nanowires, the high frequency electrodynamics of the superconducting nanowires was studied. I calculated the complex conductivity of a superconducting nanowire from the microscopic GZ theory. Then, I calculated the effect of the high-frequency field on the rate of QPS using the Mooij-nazarov duality and the semiclassical description of Ivelev-Mel'nikov. It was shown that the QPS rate is exponentially enhanced in high-frequency field. Based on this finding, I proposed new type of high-frequency radiation detector based on QPS. I calculated design parameters for a 300 Ghz detector using typical superconducting nanowires material. The part of my thesis is reflected in the following publication:

A Jafari-Salim, M. Ansari, A. Eftekharian, and A. H. Majedi. *1D-Superconducting Nanowires in High-Frequency Fields*, In preparation.

2D-Superconducting Nanostrips

In 2D nanostrips, the behaviour of vortices in SNSPDs was studied. My goal was to improve the performance of SNSPDs in terms of quantum efficiency and dark count. I showed that by making SNSPDs into multilayer structures, it is possible to achieve high quantum efficiency and low dark count. It was also shown that in a multilayer SNSPD the probability of photon absorptions is significantly increased. This work is published in [61]

A Jafari-Salim, A. Eftekharian,and A. H. Majedi. *High Quantum Efficiency and Low Dark Count Rate in Multi-layer Superconducting Nanowire Single-photon Detectors* J. Appl. Phys. 115, 054514 (2014).

6.2 Other Contributions Not Presented in Thesis

Apart from the research that were reflected in this thesis, I have also been involved in many other projects involving nano-devices and quantum information processing. Some selected works are as follows:

Quantum Ground State Effect on Fluctuation Rates

In this work, the importance of the ground state on the initial state of the vortex before thermal activation and quantum tunnelling is studied. It was shown that the correct initial state for the vortex has non-zero energy due to confining property of the potential barrier near the edges of the strip. This modifies the rate of the vortex crossing compared to fixed zero-value initial state that previously was chosen in literature. This prediction was confirmed and demonstrated by experiments. This work is published in the following paper [62]:

A. Eftekharian, H. Atikian, M. K. Akhlaghi, A. Jafari Salim, and A. H. Majedi. *Quantum Ground State Effect on Fluctuation Rates in Nano-patterned Superconducting Structures* Appl. Phys. Lett. 103, 242601 (2013).

Tripartite Entanglement in Quantum Dot Molecules

In this work, the possibility of the realization of tripartite entanglement in a double-quantum-dot system is studied. It was shown that a hybrid tripartite entanglement of two photons and the spin of the charge carrier is achievable in a finely tuned system. For this, the sequential decay of a charged bi-exciton down to a single charged carrier (electron or hole) was investigated and the higher order entangled states were identified for appropriate size and inter-dot spacing. This work is published in [63]:

M. Khoshnegar, A Jafari-Salim, M. H. Ansari, and A. H. Majedi. *Toward Tripartite Hybrid Entanglement in Quantum Dot Molecules* New J. Phys. 16, 023019 (2014).

SNSPD on Diamond

In this work, a superconducting single photon detector was fabricated on diamond substrate and it is optical and electrical properties were characterized. Realization of SNSPDs on diamond paves the way for the integration of single photon source based on nitrogen-vacancy centers (NV) in diamond and single photon detectors for optical quantum information processing. This work is reported in [64]:

H. Atikian,A. Eftekharian, A. Jafari Salim, M. J. Burek, J. T. Choy, A. H. Majedi, and M. Loncar. *Superconducting Nanowire Single Photon Detector on Diamond* Appl. Phys. Lett. 104, 122602 (2014).

6.3 Outlook

Superconducting nanostructures continue to become more important in the realization of quantum information processing. The results obtained in this thesis reveal great potentials in superconducting nanostructures for new devices and applications. Furthermore, it was shown that the performance of current quantum devices can be improved significantly. Attempt in realisation of the designs in this thesis is our next step. The biggest challenge will be the fabrication of the proposed structures. Apart from difficulties regarding fabrication, there are still many unsolved theoretical aspects in the physics of nanostructures, particularly 1D nanowires that need to be addressed. The semiclassical method that we employed in studying the effect of high-frequency field on 1D nanowires puts limits on the validity of the results we obtained. A more fundamental treatment of the matter is desirable.

APPENDICES

Appendix A

The Effective Action of Superconducting Nanowires

In this section, we review the derivation of the effective action of a superconducting nanowire in Golubev-Zaikin (GZ) theory; the effective action derived in this section will be the basis of our calculations on the conductivity of superconducting nanowires . Here, we will not repeat details of each steps; instead we confine ourselves to outline of the derivation given in [10, 11, 12, 13]. Details of quantum field theoretic methods in condensed matter physics that are extensively used in the derivation can be found in [65, 66].

A.1 The Model

The model which the effective action is derived from is a Hamiltonian with a short range attractive BCS interaction and a long range repulsive Coulomb interaction. The dynamics of the electromagnetic fields are also included in the Hamiltonian. With this model the partition function can be written

$$\mathcal{Z} = \mathrm{Tr}\exp\left(\frac{-\hat{H}}{k_B T}\right). \tag{A.1}$$

It is convenient to cast the partition function $\mathcal{Z}$ in terms of a path integral over anti-commuting electronic fields $\bar{\psi}$ and ψ and the commuting gauge fields V and $\mathbf{A}$, with the

Euclidean action

$$
\begin{aligned}
S = \int dx \Big(& \bar{\psi}_\sigma [\partial_\tau - ieV + \xi(\nabla - \frac{ie}{\hbar c}\mathbf{A})]\psi_\sigma \\
& - \lambda \bar{\psi}_\uparrow \bar{\psi}_\downarrow \psi_\downarrow \psi_\uparrow + ienV + [\mathbf{E}^2 + \mathbf{B}^2]/8\pi \Big) \, .
\end{aligned} \tag{A.2}
$$

where $\xi(\nabla) \equiv -\nabla^2/2m - \mu + U(x)$ is the kinetic term for electrons in a single conduction band, $U(x)$ describes the potential for impurities, λ is the BCS coupling constant, $\sigma = \uparrow, \downarrow$ is the spin index, and en denotes the background charge density of the ions. Here dx denotes $d^3\mathbf{x}d\tau$. The electromagnetic fields, in terms of the gauge fields can be written as $\mathbf{E} = -\nabla V + (1/c)\partial_\tau \mathbf{A}$ and $\mathbf{B} = \nabla \times \mathbf{A}$ for imaginary time formulation. In this chapter, we use units such that $\hbar$ and k_B are equal to one.

In order to decouple the BCS interaction term and introduce a collective field of superconducting order parameter $\tilde{\Delta} = \Delta e^{i\varphi}$, we use the standard Hubbard-Stratonovich transformation

$$
\begin{aligned}
\exp\left(\frac{\lambda}{\hbar}\int dx \bar{\psi}_\uparrow \bar{\psi}_\downarrow \psi_\downarrow \psi_\uparrow\right) = & \left[\int \mathcal{D}^2 \tilde{\Delta} e^{-\frac{1}{\hbar\lambda}\int dx \Delta^2}\right]^{-1} \\
& \times \int \mathcal{D}^2 \tilde{\Delta} e^{-\frac{1}{\hbar}\int dx \left(\frac{1}{\lambda}\Delta^2 + \tilde{\Delta}\bar{\psi}_\uparrow \bar{\psi}_\downarrow + \tilde{\Delta}^* \psi_\downarrow \psi_\uparrow\right)} \, ,
\end{aligned} \tag{A.3}
$$

where $\mathcal{D}$ denotes a functional differential form. We will ignore the first factor in (A.3) which is for normalization. The partition function can then be written

$$
\begin{aligned}
\mathcal{Z} &= \int \mathcal{D}^2 \tilde{\Delta} \int \mathcal{D}^3 \mathbf{A} \int \mathcal{D}V \mathcal{D}^2 \Psi e^{\left(-S_0/\hbar - \int dx \bar{\Psi} \mathcal{G}^{-1} \Psi/\hbar\right)} \, , \\
S_0[V, \mathbf{A}, \Delta] &= \int dx \left(\frac{\mathbf{E}^2 + \mathbf{B}^2}{8\pi} + ienV + \frac{\Delta^2}{\lambda}\right) \, .
\end{aligned} \tag{A.4}
$$

Here, we have used Nambu notation for the electronic fields and the matrix green function defined by

$$
\begin{aligned}
\Psi &= \begin{pmatrix} \psi_\uparrow \\ \bar{\psi}_\downarrow \end{pmatrix} \, , \quad \bar{\Psi} = \begin{pmatrix} \bar{\psi}_\uparrow & \psi_\downarrow \end{pmatrix} \, ; \\
\tilde{\mathcal{G}}^{-1} &= \begin{pmatrix} \hbar\partial_\tau - ieV + \xi(\nabla - \frac{ie}{\hbar c}\mathbf{A}) & \tilde{\Delta} \\ \tilde{\Delta}^* & \hbar\partial_\tau + ieV - \xi(\nabla + \frac{ie}{\hbar c}\mathbf{A}) \end{pmatrix} .
\end{aligned} \tag{A.5}
$$

Now, we can perform the Gaussian integral over the electronic degrees of freedom to obtain

$$\mathcal{Z} = \int \mathcal{D}^2\tilde{\Delta} \int \mathcal{D}^3\mathbf{A} \int \mathcal{D}V \exp\left(-\frac{1}{\hbar}S_{\text{eff}}\right), \tag{A.6}$$

where the effective action is

$$S_{\text{eff}} = -\operatorname{Tr}\ln\tilde{\mathcal{G}}^{-1} + S_0[V, \mathbf{A}, \Delta]. \tag{A.7}$$

Here Tr denotes tracing over both Nambu space matrices and over internal coordinates or momenta and frequencies. We can use the gauge invariance of the theory to rewrite (A.7) in a more convenient form

$$S_{\text{eff}} = -\operatorname{Tr}\ln\mathcal{G}^{-1} + S_0[V, \mathbf{A}, \Delta], \tag{A.8}$$

where

$$\mathcal{G}^{-1} = \begin{pmatrix} \hbar\partial_\tau + \xi(\nabla) - ie\Phi + \frac{m\mathbf{v}_s^2}{2} - \frac{i\hbar}{2}\{\nabla, \mathbf{v}_s\} & \Delta \\ \Delta & \hbar\partial_\tau - \xi(\nabla) + ie\Phi - \frac{m\mathbf{v}_s^2}{2} - \frac{i\hbar}{2}\{\nabla, \mathbf{v}_s\} \end{pmatrix}. \tag{A.9}$$

Here Φ and $\mathbf{v_s}$ are gauge invariant combinations defined by

$$\Phi = V - \frac{\hbar\dot{\varphi}}{2e}, \quad \mathbf{v}_s = \frac{1}{2m}\left(\nabla\varphi - \frac{2e}{\hbar c}\mathbf{A}\right). \tag{A.10}$$

The curly bracket denotes $\{A, B\} = AB + BA$.

Calculation of the action in Eq. (A.8) in an exact form is not doable; therefore, several approximations thorough perturbation expansion needs to be performed. For this, the effective action is expanded to second-order in gauge-invariant quantities Φ and $\mathbf{v_s}$. The higher order terms which give rise to non-linear electrodynamics are negligible for superconducting nanowires . The Green function in Eq. (A.9) can be broken into free and interaction parts:

$$\mathcal{G}_0^{-1} = \begin{pmatrix} \hbar\partial_\tau + \xi(\nabla) & \Delta \\ \Delta & \hbar\partial_\tau - \xi(\nabla) \end{pmatrix}, \tag{A.11}$$

and

$$\mathcal{G}_1^{-1} = \begin{pmatrix} -ie\Phi + \frac{m\mathbf{v}_s^2}{2} - \frac{i\hbar}{2}\{\nabla, \mathbf{v}_s\} & 0 \\ 0 & ie\Phi - \frac{m\mathbf{v}_s^2}{2} - \frac{i\hbar}{2}\{\nabla, \mathbf{v}_s\} \end{pmatrix}. \tag{A.12}$$

The logarithm in Eq. (A.8) can be expanded as

$$\operatorname{Tr}\ln\mathcal{G}^{-1} = \operatorname{Tr}\ln\mathcal{G}_0^{-1} + \operatorname{Tr}(\mathcal{G}_0\mathcal{G}_1^{-1}) - \frac{1}{2}\operatorname{Tr}(\mathcal{G}_0\mathcal{G}_1^{-1})^2, \tag{A.13}$$

where the Green function $\mathcal{G}_0$ is

$$\mathcal{G}_0 = \begin{pmatrix} G & F \\ F & \bar{G} \end{pmatrix}. \tag{A.14}$$

Because the non-diagonal component Δ in the matrix $\mathcal{G}_0^{-1}$ are real, we have $\bar{F} = F$, $F(x_1, x_2) = F(x_2, x_1)$ and $\bar{G}(x_1, x_2) = -G(x_2, x_1)$.

We can also assume that the magnitude of the order parameter remains close to the equilibrium value Δ_0; this enables us to expand (A.8) in $\delta\Delta(x, \tau) = \Delta(x, \tau) - \Delta_0$. After expanding to second order in $\delta\Delta$, Golubev and Zaikin average over the random potential of the impurities. This renders the effective action translationally invariant both in time and space.

A.2 Effective Action for 1D Nanowire

For specific geometry of nanowires, x is used for the coordinate along the wire, and A will be the component of the vector potential along the wire. For a cylindrical nanowire, $r_0 \sim \sqrt{s}$, and C and L the capacitance and inductance per unit length are given by relations

$$C = \frac{\epsilon}{2 \ln\left(\frac{2R_0}{r_0}\right)}, \qquad L = \frac{2}{c^2} \ln\left(\frac{2R_0}{r_0}\right), \tag{A.15}$$

where R_0 is the distance to the nearby electrodes. The Euclidean effective action of superconducting nanowire in Fourier domain can then be written

$$\begin{aligned} S_E \; &= \; \frac{s}{2} \int \frac{d\omega dk}{(2\pi)^2} \left\{ \frac{|A|^2}{Lsc^2} + \frac{C|V|^2}{s} + \hbar\tilde{\chi}_D \left| kV + \frac{\omega}{c} A \right|^2 + \hbar\tilde{\chi}_J \left| V + \frac{i\omega}{2e}\varphi \right|^2 \right. \\ &\left. + \hbar \frac{\tilde{\chi}_L}{4m^2} \left| ik\varphi + \frac{2e}{c} A \right|^2 + \tilde{\chi}_A |\delta\Delta|^2 \right\}. \end{aligned} \tag{A.16}$$

where the kernels $\tilde{\chi}_D$, $\tilde{\chi}_J$, $\tilde{\chi}_L$ and $\tilde{\chi}_A$, which depend both on the frequencies and the wave vectors, come form Feynman diagram calculations in the perturbative expansion. These kernels are expressed in terms of the averaged products of the Green functions. The real time version of these kernels, without tilde, are listed in Appendix B.

In Eq. (A.16), both A and V appear quadratically; therefore, they can be integrated out exactly. For $L = 0$ (which is negligible in most cases) we obtain

$$\begin{aligned} V &= \frac{\tilde{\chi}_J}{\frac{C}{s} + \tilde{\chi}_J + \tilde{\chi}_D k^2} \left(\frac{-i\hbar\omega}{2e} \varphi \right), && \text{(A.17)} \\ A &= 0. && \text{(A.18)} \end{aligned}$$

From Eq. (A.17), it is seen that the Josephson junction relation $V = \hbar/2e\dot{\varphi}$ is not correct for superconducting nanowires . In the limit $\tilde{\chi}_J \gg C/s + \tilde{\chi}_D k^2$, which in the case of dirty superconductors, holds for $\hbar\omega \ll \hbar\Delta_0$ and $Dk^2 \ll \Delta_0$, the Josephson junction relation is recovered.

Appendix B

Kernels

In this appendix, we list explicit expressions for the kernels of the GZ model [10, 11, 12, 13]. The χ's kernels are the real time versions of the $\tilde{\chi}$'s kernels that we encountered in the Euclidean effective action of the superconducting nanowire in Eq. (A.16). The real time kernels that we will use in our final result of Eq. (2.20) are given by

$$\begin{aligned}\chi_\Delta(\omega,k) = &-\frac{2N_0}{\lambda} + \frac{N_0}{\pi}\int d\xi_1 d\xi_2 \frac{\hbar D k^2}{(\xi_1-\xi_2)^2+\hbar^2 D^2 k^4} \\ &\times \Bigg\{ -\left(1+\frac{\xi_1\xi_2-\Delta_0^2}{E_1E_2}\right)\frac{(E_1+E_2)(1-f_1-f_2)}{(\hbar\omega+i0)^2-(E_1+E_2)^2} \\ &+ \left(1-\frac{\xi_1\xi_2-\Delta_0^2}{E_1E_2}\right)\frac{(E_1-E_2)(f_1-f_2)}{(\hbar\omega+i0)^2-(E_1-E_2)^2}\Bigg\},\end{aligned} \tag{B.1}$$

$$\begin{aligned}\chi_J(\omega,k) = &-\frac{2e^2N_0}{\pi}\int d\xi_1 d\xi_2 \frac{\hbar D k^2}{(\xi_1-\xi_2)^2+\hbar^2 D^2 k^4}\frac{\Delta_0^2}{E_1E_2} \\ &\times \left\{\frac{(E_1+E_2)(1-f_1-f_2)}{(\hbar\omega+i0)^2-(E_1+E_2)^2} + \frac{(E_1-E_2)(f_1-f_2)}{(\hbar\omega+i0)^2-(E_1-E_2)^2}\right\},\end{aligned} \tag{B.2}$$

$$\begin{aligned}\chi_L(\omega,k) = &-\frac{2m^2N_0D}{\pi}\int d\xi_1 d\xi_2 \frac{(\xi_1-\xi_2)^2}{(\xi_1-\xi_2)^2+\hbar^2 D^2 k^4}\frac{\Delta_0^2}{E_1E_2} \\ &\times \Bigg\{\frac{(E_1+E_2)(1-f_1-f_2)}{(\hbar\omega+i0)^2-(E_1+E_2)^2} \\ &+ \frac{(E_1-E_2)(f_1-f_2)}{(\hbar\omega+i0)^2-(E_1-E_2)^2}\Bigg\},\end{aligned} \tag{B.3}$$

$$
\begin{aligned}
\chi_D(\omega, k) = \frac{e^2 N_0 D}{\pi} \int d\xi_1 d\xi_2 \frac{1}{(\xi_1 - \xi_2)^2 + \hbar^2 D^2 k^4} \\
\times \Bigg\{ \left(1 + \frac{\xi_1 \xi_2 + \Delta_0^2}{E_1 E_2}\right) \frac{(E_1 - E_2)(f_1 - f_2)}{(\hbar\omega + i0)^2 - (E_1 - E_2)^2} \\
- \left(1 - \frac{\xi_1 \xi_2 + \Delta_0^2}{E_1 E_2}\right) \frac{(E_1 + E_2)(1 - f_1 - f_2)}{(\hbar\omega + i0)^2 - (E_1 + E_2)^2} \Bigg\}.
\end{aligned} \tag{B.4}
$$

Here, $E_{1,2} = \sqrt{\xi_{1,2}^2 + \Delta_0^2}$, $f_{1,2} = 1/(1 + \exp[E_{1,2}/k_B T])$. The diffusion constant is defined $D = \nu_F l/3$.

Appendix C

Quantum Tunneling in a High-frequency Field

C.1 Semmiclassical Physics and Quantum Tunneling

In this appendix, we review the effect of a high-frequency field on quantum tunnelling in the semi-classical description[40]. The approach will be based on the method developed in [1, 34, 28]. First, a brief introduction is given to the semi-classical approach to quantum mechanics and quantum tunnelling.

The semi-classical description is obtained from the stationary path approximation of the Feynman path integral approach to quantum mechanics. The stationary path of a Feynman path integral which is obtained from the variation of the action yields the Newtonian equation of motion (EOM):

$$\delta S = 0 \longrightarrow \text{EOM} \tag{C.1}$$

This relation is familiar in classical mechanics for energetically allowed region; however, the natural question that arises is that: is this method applicable to energetically forbidden regions like in quantum tunnelling? The answer is “yes”; however, it requires allowing the time to acquire an imaginary part [67]. To see this, let’s consider the action of a point particle with mass m in a potential $V(x)$. The action can be written as:

$$S = \int dt \left\{ \frac{m}{2} \left(\frac{dx}{dt} \right)^2 - V(x) + E \right\}. \tag{C.2}$$

The equation of motion is found to be

$$m\frac{d^2x}{dt^2} + V'(x) = 0, \tag{C.3}$$

and the total energy is given by

$$E = \frac{p^2}{2m} + V(x), \tag{C.4}$$

where the momentum is defined as $p(t) = mdx/dt$. By integrating Eq. (C.4), the required time t for the particle to reach infinity from point x is given by

$$t(x) = \int_x^\infty \frac{dx'\sqrt{m}}{\sqrt{2\left(E - V(x')\right)}}. \tag{C.5}$$

From Eq. (C.5), it is seen that as long as $E > V(x)$ the time remains real, but for $E < V(x)$ it acquires an imaginary part and becomes complex. Therefore, by allowing complex time, classically forbidden regions can be studied in the semi-classical approach. The tunnelling of a point particle with energy E coming from left from the potential $V(x)$ is shown in Fig. C.1. For $x > x_2$ time is real, because $E > V(x)$; however, for $x_1 < x < x_2$, the time goes in the imaginary direction. For $x < x_1$ time becomes complex, $t + i\tau_0$, where the constant imaginary part is

$$\tau_0 = \int_{x_1}^{x_2} \frac{dx\sqrt{m}}{\sqrt{2\left(V(x) - E\right)}}. \tag{C.6}$$

Therefore, for a tunnelling path of a particle moving from left to right, the time evolution is depicted in Fig. C.1 by contour C_+.

According to the semi-classical description, the tunnelling amplitude is found by calculating the action Eq. (C.2) along contour C_+. In order to find the tunnelling probability amplitude the contour C_- needs to be added, where the property $x(t^*) = x^*(t)$ has been used. Therefore, the tunnelling probability with exponential accuracy is given by

$$\begin{aligned} &\Gamma \approx \exp\left(-S_0\right), \\ &S_0 = -i \int_{C_- + C_+} dt \left[\frac{m}{2}\left(\frac{dx}{dt}\right)^2 - V(x) + E\right], \end{aligned} \tag{C.7}$$

where $x(t)$ is the solution to the classical equation of motion, i.e. Eq. (C.3), along the contour.

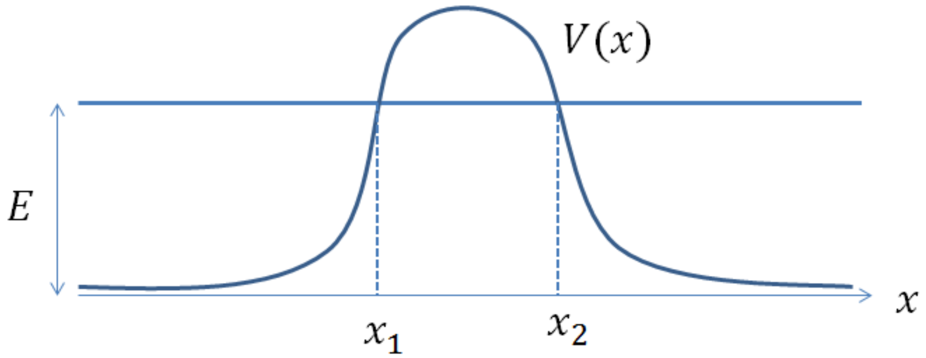

Figure C.1: Potential barrier for a particle moving from left to right with energy E. Classical turning points are indicated by x_1 and x_2. According to Eq. (C.5), for $x_1 < x < x_2$, the time becomes complex.

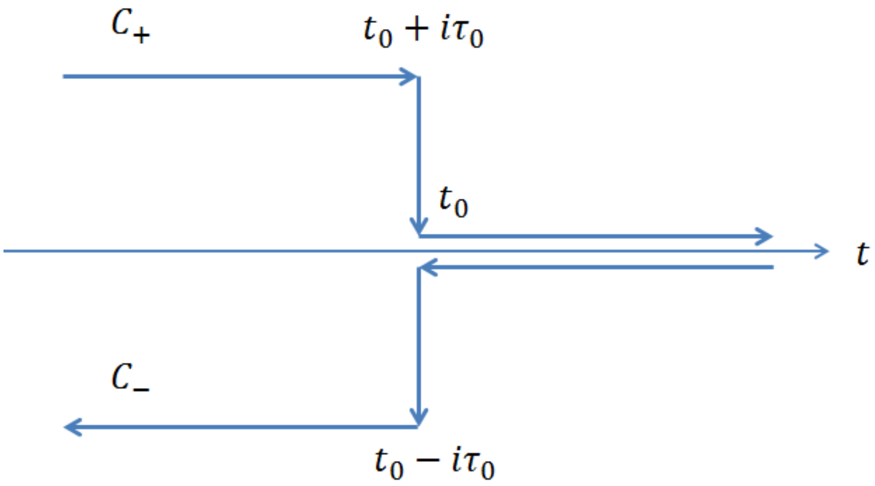

Figure C.2: The integration contour for the quantum tunnelling probability. The vertical sections correspond to the underbarrier motion.

The horizontal segments of C_+ and C_- cancel each other and only vertical segments corresponding to the under barrier motion survive. Using Eq. (C.3) in the exponent of Eq. (C.7) we get

$$\Gamma \approx \exp\left(i\int_{i\tau_0}^{-i\tau_0} dt\, m\dot{x}^2\right) = \exp\left(2im\int_{x_1}^{x_2} dx\dot{x}\right) = \exp\left(-2\int_{x_1}^{x_2} dx\sqrt{2m(V(x)-E)}\right), \tag{C.8}$$

which is the well-known WKB result in quantum mechanics [67].

If the system is in thermodynamic equilibrium before the tunnelling starts, then the tunnelling probability needs to be statistically averaged over E

$$\langle\Gamma\rangle = \int dE \exp\left[-\frac{E}{k_BT} - S(E)\right], \tag{C.9}$$

where E is given by Eq. (C.7). The largest probability of tunnelling occurs for energies that minimizes the exponent in Eq. (C.9) and is given by

$$\frac{\partial S(E)}{\partial E} = -\frac{1}{k_BT}. \tag{C.10}$$

The action for the underbarrier motion is given by

$$S(E) = 2\int_{x_1}^{x_2} dx\sqrt{2m(V(x)-E)}, \tag{C.11}$$

and the energy derivative of the action yields

$$\frac{\partial S(E)}{\partial E} = -2\int_{x_1}^{x_2} dx\frac{\sqrt{m}}{\sqrt{2(V(x)-E)}} = -2\tau_0 \tag{C.12}$$

where τ_0 is the time of the under barrier motion given by Eq. (C.6). Comparing Eqs. (C.10) and (C.12) reveals that

$$\tau_0 = \frac{1}{2k_BT}. \tag{C.13}$$

Eq. (C.12) determines the energy of the tunnelling particle. Therefore, in equilibrium, the probability of tunnelling through the barrier is given by Eq. (C.7) for real trajectories that satisfy Eq. (C.13). The real trajectories condition comes from the analysis that shows that the time-averaged probability for semiclassical processes is entirely determined by real trajectories [28].

C.1.1 Tunneling in a time-dependent potential barrier

The semi-classical method in which time can take on complex values is suitable for generalization to include tunnelling from time dependent potentials. Tunnelling from periodically modulated potential barriers is the most common application of this method and since in this thesis we are interested in sinusoidal alternating field we restrict this section of this review to potentials of the form [28, 34, 1, 15]

$$U(x,t) = V(x) + \mathcal{E}x\cos\Omega t. \tag{C.14}$$

According to the semiclassical description, the linear in the field-strength correction to the tunnelling probability is then given by

$$S_1 = -i\mathcal{E}\int_{C_-+C_+} dt\, x(t)\cos\Omega t, \tag{C.15}$$

where $x(t)$ is the solution of the unperturbed equation of motion Eq.(C.3) along the contour. During the under-barrier motion in the vertical segment of Fig. C.1, time is imaginary $t = i\tau$ and therefore the equation of motion becomes

$$m\frac{d^2x}{d\tau^2} - V'(x) = 0, \tag{C.16}$$

which in comparison to Eq. (C.3) can be interpreted as the classical equation of motion in the inverted potential.

The contour in Eq. (C.15) may be shifted to entails the singularities of the integrand. This enables calculating the integral based on the singularities of the $x(\tau)$. Therefore, the general trend of the A_1 in Eq. (C.15) depends on the specific form of the potential. In some cases S_1 can be exponentially large, which is the case we encountered in this thesis (see Chapter 3). In order to have exponential enhancement, it is necessary for the function defined as

$$h(x) = \sqrt{E - V(x)}, \tag{C.17}$$

to have singularities off the real axis in the x plane [37]. Assuming $V(x)$ has singularities of the form

$$V(x) \approx \begin{cases} \kappa(x-x_s)^{\alpha}, & \alpha < 0, \quad x \to x_s, \\ \kappa x^{\alpha}, & \alpha > 0, \quad x \to \infty, \end{cases} \tag{C.18}$$

then, the solution to Eq. (C.3) near x_s is of the form

$$x(t) = x_s + \left[-\frac{\kappa}{2m}(2-\alpha)^2(t-t_s)^2\right]^{\frac{1}{2-\alpha}}, \tag{C.19}$$

where t_s is the complex time that takes going from x_2 in Fig. C.1 to x_s given by

$$t_s = \int_{x_2}^{x_s} \frac{dx'\sqrt{m}}{\sqrt{2\left(E - V(x')\right)}}. \tag{C.20}$$

By comparing to Eq. (C.6), the time of the underbarrier motion τ_0 has the same order of the magnitude as

$$\tau_s = \operatorname{Im} t_s. \tag{C.21}$$

but for analytical potentials always $\tau_S < \tau_0$. For $\Omega\tau_s \gg 1$, the main contribution to the integral in Eq. (C.15) comes from branch-cut section in the vicinity of the singular points τ_s and τ_s^*. Therefore, the transition probability is given by

$$\Gamma(\mathcal{E}, t) = \Gamma_0 \exp\left(a_1 \cos(\Omega t)\right), \tag{C.22}$$

where

$$a_1 = \frac{2\pi\mathcal{E}}{\Omega} \left|\Gamma_E\left(\frac{2}{\alpha - 2}\right)\right|^{-1} \left[\frac{|\kappa|(2-\alpha)^2}{2m\Omega^2}\right]^{\frac{1}{2-\alpha}} \exp(\Omega\tau_s), \tag{C.23}$$

where Γ_E is the Euler Gamma function and Γ_0 is the tunnelling rate in the absence of the alternating field. The time averaging of Eq. (C.22) gives

$$\overline{\Gamma(\mathcal{E})} = \Gamma_0 \frac{1}{\sqrt{2\pi a_1}} \exp(a_1). \tag{C.24}$$

Eq. (C.24) shows that the semiclassical description is relevant only when

$$S_0 \gg a_1 \gg 1. \tag{C.25}$$

If the condition $S_0 \gg a_1$ is not satisfied, in addition to linear expansion in $\mathcal{E}$, higher order corrections need to be considered.

Appendix D

Duality Between QPS and Josephson Junction

In a seminal work published in 2006, Mooij and Nazarov proposed that the charge and flux duality can link the physics of QPS to the physics of Josephson junction phenomenon [18]. The duality between charge and flux is deemed to originate from the duality between electric and magnetic field in Maxwell equations [68]. This duality of classical Maxwell equation in superconductors manifest itself by making charge and phase as dual quantum numbers.

In a Josephson junction, Cooper pairs tunnel between two superconductors separated by an insulating layer; whereas, during a QPS the phase difference between two points along the superconducting nanowire jumps by 2π. Jumps in the phase happens due to quantum tunnelling or thermal activation.

Another hint toward a fundamental duality between QPS and Josephson junction, comes from the similarity of the QPS as a singularity in 1D systems to vortex in 2D superconductors. QPS in 1D superconductors can be seen as 2D vortices in the x and imaginary time (τ) coordinates in analogy to the x and y coordinates in vortices in 2D superconductors.

The theory of Mooij-Nazarov is based on the argument by Büchler *et al* [69] that successive QPS events can be coherent. Büchler *et al* investigated the effect of boundaries on short wires which is neglected in Golubev-Zaikin theory. They found that when the QPS fugacity ($\lambda_{QPS} \approx (\xi/\Delta_0 L)\Gamma_{QPS}$) is large enough compared to the dissipation scale R_Q/R_{shunt}, the QPSs increase rapidly in number and succesive QPS events become coherent. The QPS dynamics then needs to be treated quantum mechanically. The quantum

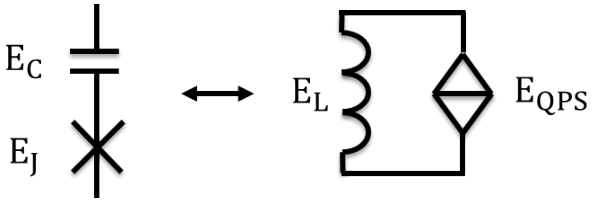

Figure D.1: The ratio of E_{QPS}/E_L as a function of the normal resistance per length for four different materials is shown. For the charge number to be the good quantum number, it is required that $E_{QPS} > 4E_L$. The unwanted region of parameters is highlighted with red.

dynamics of QPS resembles that of cooper pairs in Josephson junctions.

Based on this finding, Mooij and Nazarov introduced a QPS junction as a dual to a Josephson junction Cooper pair box [18]. The QPS junction is made of a loop that consists wide sections and a narrow superconducting nanowire to close the loop. It is worth mentioning that prior to the Mooij-Nazarov duality theorem, the idea of using QPS junction as a qubit was previously introduced by Mooij and Harmans[19]. The proposed dual QPS junction is then constructed in analogy to the Josephson Copper pair box as shown in Fig. D.1. In this dual picture,

$$\begin{aligned} E_{QPS} &\leftrightarrow E_J, \\ E_L &\leftrightarrow E_C. \end{aligned} \tag{D.1}$$

For this dual transformation to be complete, current bias and voltage bias; and impedances in series and parallel need to be transformed accordingly as shown in Fig. D.2.

In Cooper pair boxes, when the charging energy is much larger than the Josephson energy ($E_C \gg E_J$) the charge becomes a good quantum number. This leads to states with approximately fixed number of Cooper pairs. Similarly, in QPS junctions in the ring geometry, when the inductive energy is larger than the QPS energy ($E_L \gg E_{QPS}$), the phase becomes a good quantum number and because of the flux quantization, the number of fluxes trapped is enforced to be approximately fixed. Therefore, similar energy states for the Cooper pair box and QPS junction is expected [18].

In order to maintain the classical charge-phase duality in the quantum regime, the commutation relations between dual operators need to be conserved [18]. The canonical transformation between two system is given by

$$\left(\hat{q}, \hat{\phi}\right) \leftrightarrow \left(-\frac{1}{2\pi}\hat{\phi}, 2\pi\hat{q}\right), \tag{D.2}$$

which preserve the commutation relation between charge and phase according to

$$\left[\hat{q}, \hat{\phi}\right] = -i. \tag{D.3}$$

The Hamiltonian of a Cooper box shown in Fig. D.1 can be written

$$\hat{H} = E_c \hat{q}^2 - E_J \cos \hat{\phi} + \frac{\Phi_0}{2\pi} \left(I - \hat{I}_r\right) \hat{\phi} + \hat{H}_{env}, \tag{D.4}$$

where the operator $\hat{I}_r$ represent the current fluctuations in the effective resistor which is a combination of environment bosonic degrees of freedom and $\hat{H}_{env}$ represent bosoninc environment. The dual Hmiltonian for the QPS junction is given by:

$$\hat{H} = \frac{E_L}{(2\pi)^2} \hat{\phi}^2 - E_{QPS} \cos(2\pi \hat{q}) - 2e \left(V - \hat{V}_r\right) \hat{q} + \hat{H}_{env} \tag{D.5}$$

where $\hat{V}_r$ represent the voltage fluctuations in the effective resistor which is a combination of environment bosonic degrees of freedom.

The energy scale E_{QPS} introduced as the dual to E_J is assumed to be related to the QPS rate [19]:

$$E_{QPS} = \hbar \Gamma_{QPS}. \tag{D.6}$$

The QPS-Josepshon junction duality is expected to hold in the opposite limit of $E_C \ll E_J$ and $E_L \ll E_{QPS}$ as well. In this limit phase and charge become well defined variables for Josephson junction and QPS junction respectively and they manifest classical behaviour. A schematic circuit of this dual system is shown in Fig. D.2 The classical dynamics of a resistively shunted Josephson junction can be written as

$$I(t) = I_c \sin(\phi) + \frac{\Phi_0}{2\pi} \left(C \frac{d^2\phi}{dt^2} + \frac{1}{R} \frac{d\phi}{dt}\right), \tag{D.7}$$

which is the equation of motion of point particle (ϕ) in a tilted washboard potential subjected to dissipation. For $I < I_c$, in equilibrium, the phase is trapped in one of the minima of the potential. This is called the zero-voltage state of the Josephson junction. Similarly, the classical dynamics of a QPS junction can be described by

$$V(t) = V_c \sin(2\pi q) + 2e \left(L \frac{d^2 q}{dt^2} + R \frac{dq}{dt}\right). \tag{D.8}$$

For $V < V_c$, time independent solutions correspond to charge being localized in one of the potential minima. This state is called the zero-current state of a QPS junction. For application in standard of current, QPS junctions work in the charging regime and are subjected to high-frequency fields to exhibit steps.

The dual quantities in the QPS-Josephson junction duality are listed in Table D.

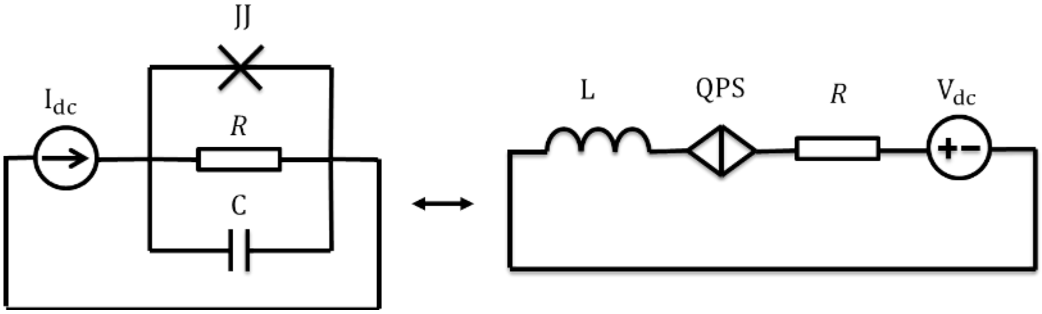

Figure D.2: Dual circuits of a Josephson junction and a QPS junction. The Josephson (QPS) junction is current (voltage) biased. Dynamics of the the two circuits are equivalent for dual parameters.

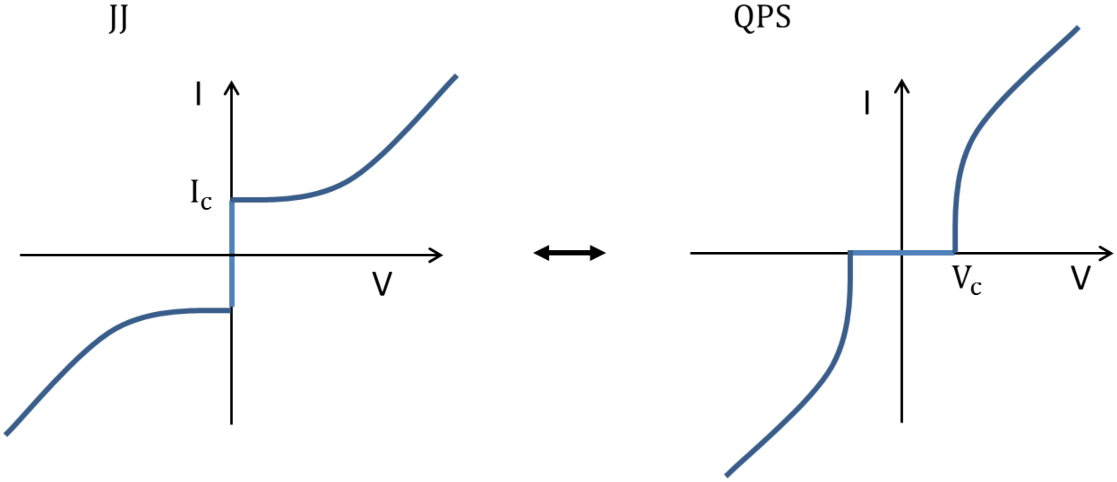

Figure D.3: Current-voltage characteristics of a Josephson junction (left) and a QPS junction(right). For $I < I_c$, the Josephson junction is in the zero-voltage stated. For $V < V_c$ the QPS is in the zero-current state.

Table D.1: Table of duality transformations between QPS and Josepshon junction

Josephson junction	QPS junction
$\hat{q}$	$-\frac{1}{2\pi}\hat{\phi}$
$\hat{\phi}$	$2\pi\hat{q}$
$H_{coup} = \frac{\Phi_0}{2\pi} I_{bias}\hat{\Phi}$	$H_{coup} = -2eV_{bias}\hat{q}$
$E_C = \frac{(2e)^2}{2C}$	$E_L = \frac{\Phi_0^2}{2L}$
$V = \frac{\Phi_0}{2\pi}\frac{d\phi}{dt}$	$I = 2e\frac{dq}{dt}$
$I = I_c \sin(\phi)$	$V = V_c \sin(2\pi q)$
$I_c = \frac{2\pi}{\Phi_0} E_J$	$V_c = \frac{2\pi}{2e} E_{QPS}$
$\hbar\omega_p = \sqrt{2E_J E_C}$	$\hbar\omega_p = \sqrt{2E_{QPS} E_L}$
$L_{kin} = \frac{\Phi_0}{2\pi I_c \cos\phi}$	$C_{kin} = \frac{2e}{2\pi V_c \cos(2\pi q)}$
$Q_J^2 = \beta_C = \frac{2\pi}{\Phi_0} I_c R^2 C$	$Q_{QPS}^2 = \beta_L = \frac{2\pi}{2e} V_c \frac{L}{R^2}$

Appendix E

Vortex Structure in 2D Films

In this appendix the vortex structure in an isolated 2D film is reviewed [54]. This lays the foundation for the vortex structure in a multi-layer system in Chapter 5. Throughout this appendix, the London approximation is used which indicates that the $|\psi(r)|$ is constant. The SI unit is employed in this appendix and the Chapter 5. The current equation from the GL theory in this limit is given by

$$\mathbf{j} = -\frac{1}{\mu_0 \lambda^2}\left(\mathbf{A} + \frac{\phi_0}{2\pi}\nabla\varphi\right), \tag{E.1}$$

where

$$\lambda^2 = \frac{m^*}{\mu_0 e^{*2}|\psi(r)|^2}. \tag{E.2}$$

For a thin film of thickness d, the sheet current density is defined as $\mathbf{K} = d\mathbf{j}$ and when replaced in (E.1) we get

$$\mathbf{K} = -\frac{2}{\mu_0 \Lambda}\left(\mathbf{A} + \frac{\phi_0}{2\pi}\nabla\varphi\right), \tag{E.3}$$

where the Pearl [54] 2D screening Length is defind as

$$\Lambda = \frac{2\lambda^2}{d}. \tag{E.4}$$

For a single pancake vortex with the fluxoid vector $\phi_0\hat{\mathbf{z}}$ at the origin the Maxwell equation is

$$\nabla \times \mathbf{B} = 0, \quad z \neq 0. \tag{E.5}$$

Using the vector potential $\mathbf{B} = \nabla \times \mathbf{A}$, in cylindrical coordinate with unit vectors defined $\hat{\rho} = \hat{\mathbf{x}} \cos(\phi) + \hat{\mathbf{y}} \sin(\phi)$, and $\hat{\phi} = -\hat{\mathbf{x}} \sin(\phi) + \hat{\mathbf{y}} \cos(\phi)$, only $\hat{\phi} A_\phi(\rho, z)$ survives and Eq. (E.5) becomes

$$\left(\frac{\partial^2}{\partial \rho^2} + \frac{1}{\rho} \frac{\partial}{\rho} + \frac{\partial^2}{\partial z^2} - \frac{1}{\rho^2} \right) A_\phi(\rho, z) = 0, \quad z \neq 0. \tag{E.6}$$

Eq. (E.6) can be solved by the method of separation of variables. The z dependent part becomes $\exp(\pm qz)$ where $+(-)$ are for $z < 0 (z > 0)$. The solution to the ρ dependent part is the Bessel function of order one, $J_1(q\rho)$. The solution to Eq. (E.6) is then given by

$$A_\phi(\rho, z) = \int_0^\infty a(q) J_1(q\rho) \exp\left(-q|z|\right) dq. \tag{E.7}$$

The boundary condition for the magnetic field across the film can be written using Eq. (E.3 as

$$K_\phi(\rho, z = 0) = \frac{1}{\mu_0} \left(B_\rho(\rho, 0_+) - B_\rho(\rho, 0_+) \right). \tag{E.8}$$

The phase ϕ is well defined everywhere except at the center of the vortex. By choosing $\varphi = -\phi$, in the cylindrical coordinate we have $\nabla \varphi = 1/\rho \hat{\phi}$, therefore, Eq. (E.3) yields:

$$K_\phi(\rho, z = 0) = -\frac{1}{\mu_0 \Lambda} \left(A_\phi(\rho, z = 0) - \frac{\phi_0}{2\pi\rho} \right) \tag{E.9}$$

using $B_\rho = \partial A_\phi / \partial z$ in Eq. (E.8), equating it to Eq. (E.9) and using

$$\frac{1}{\rho} = \int_0^\infty J_1(q\rho) dq, \tag{E.10}$$

we obtain

$$a(q) = \frac{\phi_0}{2\pi \left(q\Lambda + 1 \right)}. \tag{E.11}$$

Substituting this back into Eqs.(E.7) and (E.3) yields

$$K_\phi(\rho, z = 0) = \frac{\phi_0}{2\mu_0 \Lambda^2} \left(H_1(\rho/\Lambda) - Y_1(\rho/\Lambda) - \frac{2}{\pi} \right), \tag{E.12}$$

where H_n is the Struve function and Y_n is the Bessel function of the second kind.

$$K_\phi(\rho) \approx \begin{cases} \frac{\phi_0}{\mu_0 \pi \Lambda \rho} & \rho \ll \Lambda, \\ \frac{\phi_0}{\mu_0 \pi \rho^2} & \rho \gg \Lambda. \end{cases} \tag{E.13}$$

Likewise, the magnetic flux passing through a circle of radius ρ becomes:

$$\phi_z(\rho) \approx \left\{ \begin{array}{ll} \phi_0 \frac{\rho}{\Lambda} & \rho \ll \Lambda, \\ \phi_0 \left(1 - \frac{\rho}{\Lambda}\right) & \rho \gg \Lambda. \end{array} \right. \tag{E.14}$$

The magnetic field is then

$$\mathbf{B} = \hat{\boldsymbol{\rho}} B_\rho(\rho, z) + \hat{\mathbf{z}} B_z(\rho, z). \tag{E.15}$$

For small ρ, the current from Eq. (E.13) is identical to 3D Abrikosov bulk vortices [3]; however, for large ρ, the decay of the current is $1/\rho^2$ which is slower compared to the exponential decay in bulk [3].

Appendix F

Transfer-matrix Method for Multi-layer Thin Films

In this appendix, the transfer-matrix method in studying optical properties of multi-layer thin films which is used in Chapter 5 is reviewed [59].

At the interface between two source-free mediums (no space charge and current) the tangential (to the boundary) components of the electric field (E_t) and magnetic (H_t) fields obey

$$\begin{aligned} E_t &= E_t^+ + E_t^-, \\ H_t &= H_t^+ - H_t^-. \end{aligned} \tag{F.1}$$

where the signs (+) and (−) indicate the positive and negative-going fields respectively. Fields in Eqs. (F.1) are related

$$\begin{aligned} H &= \eta E_{\perp H}, \\ \eta &= \sqrt{\frac{\varepsilon_0}{\mu_0}} \frac{n}{\cos\theta}, \quad \text{for TM}, \\ \eta &= \sqrt{\frac{\varepsilon_0}{\mu_0}}\, n\cos\theta, \quad \text{for TE}. \end{aligned} \tag{F.2}$$

TM and TE indicate transverse magnetic and electric mode respectively. The angle θ is determined form the Snell's law and, in general, is a complex number. Here, we assume that the fist medium is non-absorptive (n_0 is real), but other layers can be absorptive with a complex refractive index, i.e., $n = n' - in''$. The Snell's law is written as

$$n_0 \sin\theta_0 = n_1 \sin\theta_1 = (n' - in'') \sin\theta_1. \tag{F.3}$$

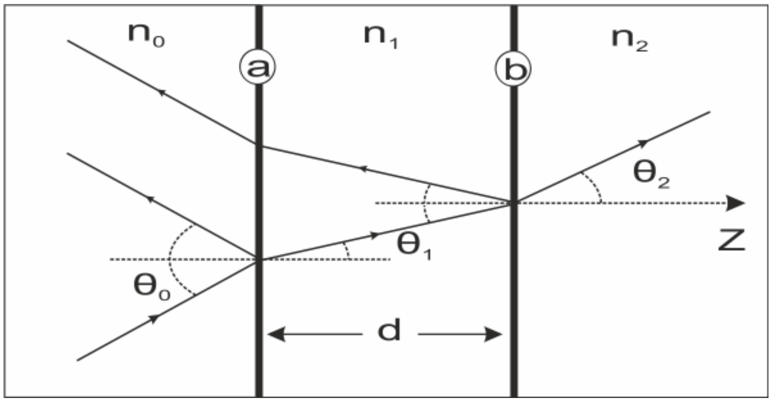

Figure F.1: Optical wave incident on a thin film of thickness d.

Combining Eqs. (F.1) and (F.2) gives

$$\begin{aligned} E_t &= E_t^+ + E_t^-, \\ H_t &= \eta E_t^+ - \eta E_t^-. \end{aligned} \tag{F.4}$$

Now, we assume that the optical beam is incident on a thin film of thickness d according to Fig. (F.1). The positive-going wave acquires the phase $\exp(-i\tilde{\varphi})$ in going from point a to point b where the phase $\tilde{\varphi}$ is defined:

$$\tilde{\varphi} = \frac{2\pi n_1 d \cos\theta_1}{\lambda_0} \tag{F.5}$$

where λ_0 is the wavelength. Similarly, a negative-going wave acquires $\exp(i\tilde{\varphi})$ in going from point a to point b. Writing Eq. (F.4) at two interfaces a and b in Fig. (F.1) and using the phase relations gives:

$$\begin{aligned} E_{1at}^+ &= E_{1bt}^+ \exp(i\tilde{\varphi}) = \frac{1}{2}\left(\frac{H_{bt}}{\eta_1} + E_{bt}\right)\exp(i\tilde{\varphi}), \\ E_{1at}^- &= E_{1bt}^- \exp(-i\tilde{\varphi}) = \frac{1}{2}\left(-\frac{H_{bt}}{\eta_1} + E_{bt}\right)\exp(-i\tilde{\varphi}), \\ H_{1at}^+ &= H_{1bt}^+ \exp(i\tilde{\varphi}) = \frac{1}{2}(H_{bt} + \eta_1 E_{bt})\exp(i\tilde{\varphi}), \\ H_{1at}^- &= H_{1bt}^- \exp(-i\tilde{\varphi}) = \frac{1}{2}(H_{bt} - \eta_1 E_{bt})\exp(-i\tilde{\varphi}). \end{aligned} \tag{F.6}$$

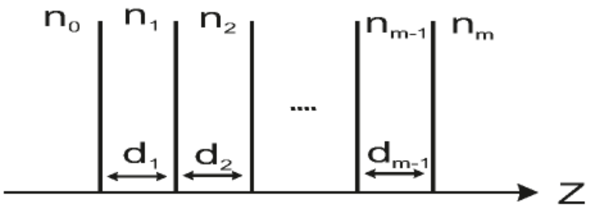

Figure F.2: An assembly of thin films with different thicknesses and refractives indices.

Then, the total tangential electric and magnetic are given by:

$$\begin{aligned} E_{at} &= E_{1at}^{+} + E_{1at}^{-} = \cos(\tilde{\varphi})E_{bt} + \frac{i\sin(\tilde{\varphi})}{\eta_1}H_{bt}, \\ H_{at} &= H_{1at}^{+} + H_{1at}^{-} = i\eta_1\sin(\tilde{\varphi})E_{bt} + \sin(\tilde{\varphi})H_{bt}. \end{aligned} \tag{F.7}$$

Eqs. (F.7) can be cast in the matrix form as:

$$\begin{bmatrix} E_{at} \\ H_{at} \end{bmatrix} = \begin{bmatrix} \cos(\tilde{\varphi}) & i\sin(\tilde{\varphi})/\eta_1 \\ i\eta_1\sin(\tilde{\varphi}) & \cos(\tilde{\varphi}) \end{bmatrix} \times \begin{bmatrix} E_{bt} \\ H_{bt} \end{bmatrix}. \tag{F.8}$$

It is convenient to normalize the fields in Eq. (F.8) by E_{bt} to get

$$\begin{bmatrix} B \\ C \end{bmatrix} = \begin{bmatrix} E_{at}/E_{bt} \\ H_{at}/E_{bt} \end{bmatrix} = \begin{bmatrix} \cos(\tilde{\varphi}) & i\sin(\tilde{\varphi})/\eta_1 \\ i\eta_1\sin(\tilde{\varphi}) & \cos(\tilde{\varphi}) \end{bmatrix} \times \begin{bmatrix} 1 \\ \eta_2 \end{bmatrix}. \tag{F.9}$$

For multiple thin films, as shown in Fig. F.2, the generalization of Eq. (F.9) is straightforward and is given by

$$\begin{bmatrix} B \\ C \end{bmatrix} = \left(\prod_{i=1}^{m-1} \begin{bmatrix} \cos(\tilde{\varphi}_i) & i\sin(\tilde{\varphi}_i)/\eta_1 \\ i\eta_i\sin(\tilde{\varphi}_i) & \cos(\tilde{\varphi}_i) \end{bmatrix}\right) \times \begin{bmatrix} 1 \\ \eta_m \end{bmatrix}, \tag{F.10}$$

where for each layer η_i and $\tilde{\varphi}_i$ are determined from Eq. (F.2) and Eq. (F.5) respectively. Having the matrix $[B \quad C]'$ in Eq. (F.10), the reflection (R), trasmittance (T) and absorption (A) coefficients are given by

$$\begin{aligned} R &= \frac{|\eta_0 B - C|^2}{|\eta_0 B + C|^2}, \\ T &= \frac{4\eta_0\,\mathrm{Re}\{\eta_m\}}{|\eta_0 B + C|^2}, \\ A &= \frac{4\eta_0\,\mathrm{Re}\{BC^* - \eta_m\}}{|\eta_0 B + C|^2}, \end{aligned} \tag{F.11}$$

where η_m is given by Eq. (F.2) for $n = n_m$, where n_m is the refractive index of the substrate. It is easy to see forn Eq. (F.11) that

$$R + T + A = 1. \tag{F.12}$$

References

[1] B. I. Ivlev and V. I. Mel'nikov. Alternating-current-induced decay of decay of the zero-voltage of josephson junctions. *Sov. Phys. JETP*, 62:1298–1302, Dec 1985.

[2] Kristine M. Rosfjord, Joel K. W. Yang, Eric A. Dauler, Andrew J. Kerman, Vikas Anant, Boris M. Voronov, Gregory N. Gol'tsman, and Karl K. Berggren. Nanowire single-photon detector with an integrated optical cavity and anti-reflection coating. *Opt. Express*, 14(2):527–534, Jan 2006.

[3] M. Tinkham. *Introduction to Superconductivity: Second Edition*. Dover books on physics and chemistry. Dover Publications, 2004.

[4] M. H. Devoret, A. Wallraff, and J. M. Martinis. Superconducting Qubits: A Short Review. *eprint arXiv:cond-mat/0411174*, November 2004.

[5] Chandra M Natarajan, Michael G Tanner, and Robert H Hadfield. Superconducting nanowire single-photon detectors: physics and applications. *Superconductor Science and Technology*, 25(6):063001, 2012.

[6] J. S. Langer and Vinay Ambegaokar. Intrinsic resistive transition in narrow superconducting channels. *Phys. Rev.*, 164:498–510, Dec 1967.

[7] D. E. McCumber and B. I. Halperin. Time scale of intrinsic resistive fluctuations in thin superconducting wires. *Phys. Rev. B*, 1:1054–1070, Feb 1970.

[8] N. Giordano. Evidence for macroscopic quantum tunneling in one-dimensional superconductors. *Phys. Rev. Lett.*, 61:2137–2140, Oct 1988.

[9] N. Giodano. Superconducting fluctuations in one dimension. *Physica B: Condensed Matter*, 203(34):460 – 466, 1994.

[10] A D Zaikin, D S Golubev, A van Otterlo, and G T Zimanyi. Quantum fluctuations and dissipation in thin superconducting wires. *Physics-Uspekhi*, 41(2):226, 1998.

[11] Dmitri S. Golubev and Andrei D. Zaikin. Quantum tunneling of the order parameter in superconducting nanowires. *Phys. Rev. B*, 64:014504, Jun 2001.

[12] Andrei D. Zaikin, Dmitrii S. Golubev, Anne van Otterlo, and Gergely T. Zimányi. Quantum phase slips and transport in ultrathin superconducting wires. *Phys. Rev. Lett.*, 78:1552–1555, Feb 1997.

[13] K.Yu. Arutyunov, D.S. Golubev, and A.D. Zaikin. Superconductivity in one dimension. *Physics Reports*, 464(12):1 – 70, 2008.

[14] William A. Little. Decay of persistent currents in small superconductors. *Phys. Rev.*, 156:396–403, Apr 1967.

[15] A.O Caldeira and A.J Leggett. Quantum tunnelling in a dissipative system. *Annals of Physics*, 149(2):374 – 456, 1983.

[16] A. O. Caldeira and A. J. Leggett. Influence of dissipation on quantum tunneling in macroscopic systems. *Phys. Rev. Lett.*, 46:211–214, Jan 1981.

[17] J. E. Mooij and Gerd Schön. Propagating plasma mode in thin superconducting filaments. *Phys. Rev. Lett.*, 55:114–117, Jul 1985.

[18] J. E. Mooij and Yu. V. Nazarov. Superconducting nanowires as quantum phase-slip junctions. *Nature Physics*, 2(3):169–172, 2006.

[19] J E Mooij and C J P M Harmans. Phase-slip flux qubits. *New Journal of Physics*, 7(1):219, 2005.

[20] O. V. Astafiev, L. B. Ioffe, S. Kafanov, Yu Pashkin, Arutyunov, D. Shahar, O. Cohen, and J. S. Tsai. Coherent quantum phase slip. *Nature*, 484(7394):355–358, April 2012.

[21] C.H. Webster, S.P. Giblin, D. Cox, T.J.B.M. Janssen, and A.B. Zorin. A quantum current standard based on phase slip. In *Precision Electromagnetic Measurements Digest, 2008. CPEM 2008. Conference on*, pages 628 –629, june 2008.

[22] A. M. Hriscu and Yu. V. Nazarov. Coulomb blockade due to quantum phase slips illustrated with devices. *Phys. Rev. B*, 83:174511, May 2011.

[23] T. T. Hongisto and A. B. Zorin. Single-charge transistor based on the charge-phase duality of a superconducting nanowire circuit. *Phys. Rev. Lett.*, 108:097001, Feb 2012.

[24] Jeff Flowers. The route to atomic and quantum standards. *Science*, 306(5700):1324–1330, 2004.

[25] B. Jeanneret and S. P. Benz. Application of the josephson effect in electrical metrology. *The European Physical Journal Special Topics*, 172(1):181–206, 2009.

[26] L. N. Bulaevskii, M. J. Graf, C. D. Batista, and V. G. Kogan. Vortex-induced dissipation in narrow current-biased thin-film superconducting strips. *Phys. Rev. B*, 83:144526, Apr 2011.

[27] H. Bartolf, A. Engel, A. Schilling, K. Il'in, M. Siegel, H.-W. Hübers, and A. Semenov. Current-assisted thermally activated flux liberation in ultrathin nanopatterned nbn superconducting meander structures. *Phys. Rev. B*, 81:024502, Jan 2010.

[28] B. I. Ivlev and V. I. Mel'nikov. Semiclassical processes in a high-frequency field. *Sov. Phys. JETP*, 63:1295–1305, 1986.

[29] Ryogo Kubo. Statistical-mechanical theory of irreversible processes. i. general theory and simple applications to magnetic and conduction problems. *Journal of the Physical Society of Japan*, 12(6):570–586, 1957.

[30] D. C. Mattis and J. Bardeen. Theory of the anomalous skin effect in normal and superconducting metals. *Phys. Rev.*, 111:412–417, Jul 1958.

[31] Alexey Bezryadin. Quantum suppression of superconductivity in nanowires. *Journal of Physics: Condensed Matter*, 20(4):043202, 2008.

[32] Michel H. Devoret, John M. Martinis, Daniel Esteve, and John Clarke. Resonant activation from the zero-voltage state of a current-biased josephson junction. *Phys. Rev. Lett.*, 53:1260–1263, Sep 1984.

[33] Myung-Ho Bae, R C Dinsmore III, M Sahu, and A Bezryadin. Stochastic and deterministic phase slippage in quasi-one-dimensional superconducting nanowires exposed to microwaves. *New Journal of Physics*, 14(4):043014, 2012.

[34] B. I. Ivlev and V. I. Mel'nikov. Stimulation of tunneling by a high-frequency field: Decay of the zero-voltage state in josephson junctions. *Phys. Rev. Lett.*, 55:1614–1617, Oct 1985.

[35] D. E. McCumber. Effect of ac impedance on dc voltagecurrent characteristics of superconductor weaklink junctions. *Journal of Applied Physics*, 39(7), 1968.

[36] W. C. Stewart. Currentvoltage characteristics of josephson junctions. *Applied Physics Letters*, 12(8), 1968.

[37] B. I. Ivlev and V. I. Mel'nikov. Quantum tunnelling in condensed media. Modern Problems in Condensed Matter Sciences, Eds. Elsevier Science, 1992.

[38] Sidney Shapiro. Josephson currents in superconducting tunneling: The effect of microwaves and other observations. *Phys. Rev. Lett.*, 11:80–82, Jul 1963.

[39] A. I. Larkin and Yu. N. Ovchinnikov. Decay of the supercurrent in tunnel junctions. *Phys. Rev. B*, 28:6281–6285, Dec 1983.

[40] A. Kamenev. *Field Theory of Non-Equilibrium Systems.* Cambridge University Press, 2011.

[41] Jonas Zmuidzinas and P.L. Richards. Superconducting detectors and mixers for millimeter and submillimeter astrophysics. *Proceedings of the IEEE*, 92(10):1597–1616, 2004.

[42] C.A. Balanis. *Antenna Theory: Analysis and Design.* Wiley, 2012.

[43] C. N. Lau, N. Markovic, M. Bockrath, A. Bezryadin, and M. Tinkham. Quantum phase slips in superconducting nanowires. *Phys. Rev. Lett.*, 87:217003, Nov 2001.

[44] C. H. Webster, J. C. Fenton, T. T. Hongisto, S. P. Giblin, A. B. Zorin, and P. A. Warburton. Nbsi nanowire quantum phase-slip circuits: dc supercurrent blockade, microwave measurements, and thermal analysis. *Phys. Rev. B*, 87:144510, Apr 2013.

[45] J. T. Peltonen, O. V. Astafiev, Y. P. Korneeva, B. M. Voronov, A. A. Korneev, I. M. Charaev, A. V. Semenov, G. N. Golt'sman, L. B. Ioffe, T. M. Klapwijk, and J. S. Tsai. Coherent Flux Tunneling Through NbN Nanowires. *ArXiv e-prints*, May 2013.

[46] J. S. Lehtinen, K. Zakharov, and K. Yu. Arutyunov. Coulomb blockade and bloch oscillations in superconducting ti nanowires. *Phys. Rev. Lett.*, 109:187001, Oct 2012.

[47] Amin Eftekharian, Haig Atikian, and A. Hamed Majedi. Plasmonic superconducting nanowire single photon detector. *Opt. Express*, 21(3):3043–3054, Feb 2013.

[48] F. Marsili, V. B. Verma, A. J. Stern, S. Harrington, E. A. Lita, T. Gerrits, Vayshenker I., B. Baek, D. M. Shaw, P. R. Mirin, and W. S. Nam. Detecting single infrared photons with 93% system efficiency. *Nat Photon*, 7(3):210–214, March 2013.

[49] A. Engel, K. Inderbitzin, A. Schilling, R. Lusche, A. Semenov, H. Hubers, D. Henrich, M. Hofherr, K. Il'in, and M. Siegel. Temperature-dependence of detection efficiency in nbn and tan snspd. *Applied Superconductivity, IEEE Transactions on*, 23(3):2300505–2300505, 2013.

[50] A.M. Goldman and S.A. Wolf. *Percolation, localization, and superconductivity.* NATO ASI series: Physics. Plenum Press, published in cooperation with NATO Scientific Affairs Division, 1984.

[51] JohnR. Clem. Pancake vortices. *Journal of Superconductivity*, 17(5):613–629, 2004.

[52] G. Blatter, M. V. Feigel'man, V. B. Geshkenbein, A. I. Larkin, and V. M. Vinokur. Vortices in high-temperature superconductors. *Rev. Mod. Phys.*, 66:1125–1388, Oct 1994.

[53] John R. Clem. Phenomenological theory of magnetic structure in the high-temperature superconductors. *Physica C: Superconductivity*, 162164, Part 2(0):1137 – 1142, 1989.

[54] J. Pearl. Current distribution in superconducting films carrying quantized fluxoids. *Applied Physics Letters*, 5(4):65–66, 1964.

[55] A. De Col, V. B. Geshkenbein, and G. Blatter. Dissociation of vortex stacks into fractional-flux vortices. *Phys. Rev. Lett.*, 94:097001, Mar 2005.

[56] John R. Clem and Karl K. Berggren. Geometry-dependent critical currents in superconducting nanocircuits. *Phys. Rev. B*, 84:174510, Nov 2011.

[57] L. N. Bulaevskii, Matthias J. Graf, and V. G. Kogan. Vortex-assisted photon counts and their magnetic field dependence in single-photon superconducting detectors. *Phys. Rev. B*, 85:014505, Jan 2012.

[58] Vinay Ambegaokar and Alexis Baratoff. Tunneling between superconductors. *Phys. Rev. Lett.*, 10:486–489, Jun 1963.

[59] H.A. Macleod. *Thin-Film Optical Filters, Fourth Edition.* Series in Optics and Optoelectronics. Taylor & Francis, 2010.

[60] Xiaolong Hu, C.W. Holzwarth, D. Masciarelli, E.A. Dauler, and K.K. Berggren. Efficiently coupling light to superconducting nanowire single-photon detectors. *Applied Superconductivity, IEEE Transactions on*, 19(3):336–340, 2009.

[61] A. Jafari Salim, A. Eftekharian, and A. Hamed Majedi. High quantum efficiency and low dark count rate in multi-layer superconducting nanowire single-photon detectors. *Journal of Applied Physics*, 115(5):–, 2014.

[62] Amin Eftekharian, Haig Atikian, Mohsen K. Akhlaghi, Amir Jafari Salim, and A. Hamed Majedi. Quantum ground state effect on fluctuation rates in nano-patterned superconducting structures. *Applied Physics Letters*, 103(24):–, 2013.

[63] M Khoshnegar, A Jafari-Salim, M H Ansari, and A H Majedi. Toward tripartite hybrid entanglement in quantum dot molecules. *New Journal of Physics*, 16(2):023019, 2014.

[64] Haig A. Atikian, Amin Eftekharian, A. Jafari Salim, Michael J. Burek, Jennifer T. Choy, A. Hamed Majedi, and Marko Lonar. Superconducting nanowire single photon detector on diamond. *Applied Physics Letters*, 104(12):–, 2014.

[65] Gorkov L.P. Abrikosov, A.A. and Dzyaloshinskii. *Quantum Field Theoretical Methods in Statistical Physics*. Dover Publications, 1965.

[66] A. Altland and B.D. Simons. *Condensed Matter Field Theory*. Cambridge University Press, 2010.

[67] L.D. Landau and E.M. Lifshits. *Quantum Mechanics: Non-relativistic Theory*. Butterworth Heinemann. Butterworth-Heinemann, 1977.

[68] Andrew J Kerman. Fluxcharge duality and topological quantum phase fluctuations in quasi-one-dimensional superconductors. *New Journal of Physics*, 15(10):105017, 2013.

[69] H. P. Büchler, V. B. Geshkenbein, and G. Blatter. Quantum fluctuations in thin superconducting wires of finite length. *Phys. Rev. Lett.*, 92:067007, Feb 2004.

[70] Lau C.N. Tinkham M. Bezryadin, A. Quantum suppression of superconductivity in ultrathin nanowires. *Nature*, 404(6781):971–974, 2000. cited By (since 1996) 340.

[71] M. V. Feigel'man, L. B. Ioffe, and M. Mézard. Superconductor-insulator transition and energy localization. *Phys. Rev. B*, 82:184534, Nov 2010.